ESTIMATING MARINE PHYTOPLANKTON BIOMASS AND PRODUCTIVITY FROM AUTONOMOUS PROFILING FLOATS

by

Adam Christopher Stoer

Submitted in partial fulfilment of the requirements
for the degree of Master of Science

at

Dalhousie University
Halifax, Nova Scotia
November 2023

Table of Contents

List of Tables

Main

Appendix A

Appendix B

Appendix C

List of Figures

Main

Appendix A

Appendix B

Appendix C

Abstract

Knowledge on the biomass and productivity of ocean phytoplankton is fundamental to our understanding of life on Earth. Phytoplankton are autotrophic microbes at the base of the marine food web, that, through photosynthesis, produce organic matter that sustains higher trophic levels – a rate termed net primary productivity. Conventional approaches to measuring the biomass and productivity of phytoplankton often involve the use of satellite remote sensing. Satellites provides daily, global images at kilometer-scale resolution, offering an unprecedented view of the ocean. However, satellites only observe a small portion of the sunlit surface ocean, missing out on biomass and productivity below the surface. In this thesis, I investigate the uncertainties relating to subsurface biomass and productivity by using the fleet of Biogeochemical-Argo floats. These robotic profiling platforms are distributed across the globe and provide proxy bio-optical observations of chlorophyll-a (from fluorescence) and carbon biomass (from particle backscatter) throughout the water-column. In Chapter 2, I assess the quality and quantity of the biogeochemical data collected by the Biogeochemical-Argo program. I provide a census of this data for each the primary variables that the program measures, including chlorophyll-a fluorescence and particle backscatter. I identify interannual trends in data quality, and areas where more data could be collected in the future. In Chapter 3, I design a method for estimating net primary productivity from daily cycles of particulate carbon. In this approach, I construct the daily cycle of particulate carbon from quality-controlled particle backscattering taken at ~5 or 10 days intervals. I demonstrate that the primary productivity inferred from daily cycles varies seasonally and regionally, producing estimates that are comparable to satellite models. With this chapter, I argue that this approach could 1) constrain uncertainties in satellite-based models with regard to the vertical structure of productivity, and 2) identify climate-related, basin-scale trends in ocean productivity. In Chapter 4, I use the global BGC-Argo array to estimate Earth's stock of phytoplankton. I also describe the phenology and biogeography of phytoplankton carbon and chlorophyll-a. I highlight how in the vast majority of the ocean the spatiotemporal distribution of carbon substantially differs from the metric of chlorophyll-a, which is commonly used as a proxy for phytoplankton biomass. With these results, I make the point – like others have before – that to properly describe the basic naturalistic tendencies of Earth's phytoplankton stocks, the proper metric of carbon must be used and must include information from throughout the water-column. The combination of these chapters underscores how profiling robots can provide a more accurate, holistic view of ocean phytoplankton.

List of Abbreviations and Symbols Used

Abbreviation	Units	Description
b_{bp}	m^{-1}	Particle backscattering
$b_{bp,phyto}$	m^{-1}	Particle backscattering from phytoplankton
$b_{bp,NAP}$	m^{-1}	Particle backscattering from non-algal particles
BGC	-	Biogeochemical
BGC-Argo	-	Biogeochemical-Argo
CAFE	-	Carbon, absorption, and fluorescence euphotic-resolving [productivity model]
CbPM	-	Carbon-based productivity model
Chla	mg Chla m^{-3}	Chlorophyll-a concentration
Chla:C_{org}	mg Chla mg C_{org}^{-1}	The ratio of chlorophyll-a to organic carbon biomass
CI	-	Confidence interval
C_{org}	mg C_{org} m^{-3}	Organic carbon biomass of phytoplankton
CR	mmol [C or O_2] m^{-3}	Community respiration
CTD	-	Conductivity-temperature-depth
DAC	-	Data assembly center
DMQC	-	Delayed-mode quality control
ETOPO5	-	Earth topography 5-min grid [dataset]
E_d	W m^{-2} nm^{-1}	Downwelling irradiance
GCP	mmol C m^{-3}	Gross carbon production
GO-BGC	-	Global-Ocean Biogeochemistry Array
GOP	mmol O_2 m^{-3}	Gross oxygen production
HPLC		High pressure liquid chromatography
MLD	m	Mixed-layer depth
MODIS	-	Moderate Resolution Imaging Spectroradiometer
NAAMES	-	North Atlantic Aerosol and Marine Ecosystem Study
NO_3^-	μmol kg^{-1}	Nitrate concentration
NODC	-	National Oceanographic Data Center
$NPP_{b_{bp}}$	mmol C m^{-3}	Net primary productivity inferred from daily cycles of particle backscatter
$NPP_{\Delta O_2}$	mmol C m^{-3}	Net primary productivity inferred from daily cycles of dissolved oxygen anomaly
NPQ	-	Non-photochemical quenching
N	%	Percentage of high-quality data points in a profile
n_1	data points	Number of data points in a profile with a quality-control flag of "1"
n_2	data points	Number of data points in a profile with a quality-control flag of "2"
n_3	data points	Number of data points in a profile with a quality-control flag of "3"
n_4	data points	Number of data points in a profile with a quality-control flag of "4"
n_5	data points	Number of data points in a profile with a quality-control flag of "5"
n_8	data points	Number of data points in a profile with a quality-control flag of "8"
O_2	μmol kg^{-1}	Dissolved oxygen concentration
ΔO_2	μmol kg^{-1}	Anomaly in dissolved oxygen concentration
PAR	μmol m^{-2} s^{-1}	Photosynthetically available radiation

PAR/E_d	-	Measurements of co-located photosynthetically available radiation and irradiance at 380, 412, and 490 nm. Units for each can be found in this table.
PER	%	Percent extracellular release
POC	mmol POC m^{-3}	Particulate organic carbon concentration
pH	dimensionless	Potential of hydrogen/acidity/basicity
P_{HQ}	%	Percentage of high-quality profiles
P_{LQ}	%	Percentage of low-quality profiles
P_{NR}	%	Percentage of unresponsive profiles
PQ	mol O_2 mol C^{-1}	Photosynthetic quotient; the ratio of gross oxygen production to gross carbon production
R_{Float}	% remaining at 36.5 cycles	Survival rate of float profile
R_{FUNC}	% remaining at 36.5 cycles	Survival rate of profiles with functioning sensors
R_{HQ}	% remaining at 36.5 cycles	Survival rate of profiles with high-quality data
RTQC	-	Real-time quality control
R^2	-	R-squared; the coefficient of determination
SeaWiFS	-	Sea-viewing Wide Field-of-View Sensor
S_{HQ}	profiles	Number of high-quality profiles
S_{LQ}	profiles	Number of low-quality profiles
S_{NR}	profiles	Number of unresponsive profiles
S_{NOQC}	profiles	Number of profiles with no quality control
SOCCOM	-	Southern Ocean Carbon and Climate Observations and Modelling
QC	-	Quality control
VGPM	-	Vertically generalized productivity model
z_{eu}	m	Euphotic depth defined by the 1% light level
^{14}C-NPP	mmol C m^{-3}	Net primary productivity estimated from incubations with radiocarbon.
ΣChla	mg Chla m^{-2}	Depth-integrated chlorophyll-a
ΣC_{org}	mg C_{org} m^{-2}	Depth-integrated organic carbon biomass
ΣNPP	mol C m^{-2} yr^{-1}	Depth-integrated net primary productivity
$\Sigma NPP_{b_{bp}}$	mol C m^{-2} yr^{-1}	Depth-integrated net primary productivity inferred from daily cycles of particle backscatter
$\Sigma NPP_{\Delta O_2}$	mol C m^{-2} yr^{-1}	Depth-integrated net primary productivity inferred from daily cycles of dissolved oxygen anomaly

Acknowledgements

I'd like to give special thanks to my supervisor, Dr. Katja Fennel, who has been an invaluable role model and guide throughout my graduate studies. I thank my advisory committee: Dr. Andrew Irwin, Dr. Blair Greenan, and Dr. Marlon Lewis for their helpful conversations while developing this research. I thank Dr. Robert Izett for helpful clarifying discussions on productivity early-on in my studies and for his comments on the manuscript associated with Chapter 3. I thank Jessica Oberlander for helpful discussions and feedback on various writing and presentations, especially on Chapter 4. For the research completed in Chapter 2, I thank Dr. Yui Takeshita, Dr. Tanya Maurer, Charlotte Begouen Demeaux, Dr. Henry Bittig, Dr. Emmanuel Boss, Dr. Hervé Claustre, Dr. Giorgio Dall'Olmo, Dr. Blair Greenan, Dr. Kenneth Johnson, Dr. Emanuele Organelli, Dr. Raphaëlle Sauzède, and Dr. Catherine Schmechtig for their contributions to the manuscript associated with that chapter. Finally, I thank Dr. John Cullen for his insightful feedback on the manuscripts associated with Chapter 3 and Chapter 4.

Chapter 1

INTRODUCTION

Despite their small size, phytoplankton play a crucial role in Earth's ecosystems. During the day, phytoplankton produce organic matter and oxygen through photosynthesis – a metric referred to as primary productivity. The biomass that is produced via photosynthesis sustains higher trophic organisms (Lindeman, 1942) and contributes to the long-term sequestration of atmospheric carbon dioxide as the remaining organic matter sinks into the deep ocean (Falkowski et al., 2000).

Monitoring these vital organisms has never been more important given ongoing anthropogenic changes making the ocean warmer (Cheng et al., 2022), more acidic (Doney et al., 2009), and less oxygenated (Schmidtko et al., 2017). Phytoplankton biomass is commonly inferred from satellite images of chlorophyll-a (Chla), a pigment unique to all photosynthetic organisms and can be estimated from ocean colour. More recently, there has been renewed focus to describe phytoplankton bloom dynamics based on carbon biomass (e.g., Behrenfeld et al., 2005; Behrenfeld and Boss, 2018). On the other hand, primary productivity is modelled from various environmental inputs, and applied to satellite observations to obtain a large-scale view of biological production (Eppley et al., 1985; Behrenfeld and Falkowski, 1997). While satellites have helped address fundamental questions about phytoplankton biogeography and seasonality

(Behrenfeld et al., 2005; Platt and Sathyendranath, 2008; Racault et al., 2012; Silsbe et al., 2016), and climate-driven trends (Behrenfeld et al., 2006, 2016), satellite ocean colour technology has limitations.

To illustrate this limitation, imagine sitting on a dock staring into a lake during a bright, sunny afternoon. The human eye can likely only see a foot or two into the water, especially if the water is brown in colour or full of small particles. This is because the sunlight penetrating the lake's surface is absorbed and scattered by phytoplankton and decaying material in the water, and by the water itself. Only a tiny amount of light from the sun returns back out of the water column and into the eye. In this thought experiment, an eye is like the satellite's radiometer. Both can only "see" so deep before there is too little light to sense. In practice, this limitation means that 90% of the reflected light comes what is called the first optical depth (Gordon and McCluney, 1975), and in satellite observation means that only phytoplankton close to the surface are directly observed, missing out on the phytoplankton present far deeper in the ocean. As a rule of thumb, phytoplankton generally grow at depths approximately five-times greater than the sensing capability of the satellite (Morel, 1988). This limitation is not always considered, and when it is, broad assumptions must be made concerning the vertical structure of phytoplankton biomass and productivity (Behrenfeld and Falkowski, 1997; Westberry et al., 2008; Silsbe et al., 2016).

The maturation of underwater robotic technology in the past two decades has helped solve this observational limitation (Chai et al., 2020). Underwater robots can be deployed for long periods to collect detailed measurements hundreds of meters deep. The biogeochemical- (BGC-) Argo program, an extension of the Argo program, has deployed

robotic profiling "floats" for the past decade, amassing an unprecedented database of ~250,000 water-column profiles (Roemmich et al., 2019; Claustre et al., 2020; Stoer et al., 2023). Alongside temperature, salinity, and depth, BGC-Argo floats aim to measure six key metrics in ocean biogeochemistry: dissolved oxygen (O_2), pH, nitrate (NO_3^-), fluorescence from Chla, particle backscatter (b_{bp}), and downwelling light. The program aims to sustain an array of 1,000 actively-monitoring floats within a few years. The size of such an array would provide more profiles in a couple years than ship-based efforts have in the past fifty (Chai et al., 2020). The BGC-Argo monitoring program offers a consistent source of information about the ocean's subsurface biogeochemistry – and phytoplankton – that would otherwise not be possible with satellite observation.

1.1 Objectives

In this thesis, I utilize three key metrics obtained through the BGC-Argo program, specifically O_2, Chla fluorescence, and b_{bp}, to enhance our comprehension of subsurface phytoplankton within the ocean. Each of these metrics exhibits variation that is tied to photosynthetic processes, and through comprehensive analysis, can yield valuable insights into standing stocks and productivity of these abundant photosynthetic microbes.

This thesis is a compendium of research I've prepared while studying at Dalhousie University. I have kept the introduction intentionally short because most of the necessary background information is available in appropriate chapters. With slight modifications, each chapter is based on research that is published, accepted, or in preparation for submission to a journal. These modifications generally include making symbols and

abbreviations consistent between chapters, renumbering figures and tables, removing some introductory text, and switching “we” to “I”*.

I answer three main questions in this thesis, which are:

1. What is the overall quality and quantity of BGC-Argo Float measurements?
2. Can net primary productivity be inferred from daily cycles of carbon?
3. What is the distribution and stock of Earth’s phytoplankton carbon and Chla biomass?

In Chapter 2, I aim to describe the quality and quantity of each biogeochemical measurement using the entire BGC-Argo database. A census of the data will help identify where BGC data is lacking, where improvements could be made, and contextualize its use in later chapters. In Chapter 3, my aim is to estimate daily cycles of particulate carbon from b_{bp} to infer depth-resolved primary productivity. This research follows what was done by Johnson and Bif (2021) who showed that the daily cycle in dissolved oxygen can be extracted the BGC-Argo array and subsequently be used to infer primary productivity. In Chapter 4, I focus on constraining global phytoplankton stocks and describe the phenology and biogeography of phytoplankton carbon biomass in contrast to Chla concentrations at the surface, which is commonly used as a proxy for the stock of phytoplankton carbon biomass.

*This latter modification should in no way imply that trivial contributions were made by my co-authors.

Chapter 2

A CENSUS OF BIOGEOCHEMICAL DATA QUALITY FROM PROFILING ARGO FLOATS[†]

2.1 Introduction

Assessing the quality and quantity of BGC-Argo observations offers valuable information for its use in standard oceanographic research. With the goal of sustaining a global network of 1,000 floats, BGC-Argo aims to deploy 250 floats each year equipped to measure six key properties: O_2, NO_3^-, pH, Chla (from fluorescence), b_{bp}, and downwelling light as photosynthetically available radiation (PAR) and irradiance (E_d). The BGC-Argo is designed to deliver this BGC data in real-time and within ~24 hours of

[†]This chapter and Appendix A are a modified version of the article titled "A Census of Quality-Controlled Biogeochemical Argo Float Measurements" by Adam Stoer, Yui Takeshita, Tanya Maurer, Charlotte Begouen Demeaux, Henry Bittig, Emmanuel Boss, Hervé Claustre, Giorgio Dall'Olmo, Blair Greenan, Kenneth Johnson, Emanuele Organelli, Raphaëlle Sauzède, Catherine Schmechtig, and Katja Fennel published in Frontiers in Marine Science published by Frontiers Media SA on October 27, 2023 under the terms of CC BY 4.0, which permits the use, distribution, and reproduction in any medium, provided the original work is properly cited. This citation for this work can be found under Stoer et al. (2023).

collection. This real-time oceanographic monitoring system thus requires parameter-specific, quality-control (QC) procedures.

The data structure and QC procedures, among other aspects, are provided in the guide by Bittig et al. (2019). Briefly, profile data received from each BGC-Argo float cycle is formatted into two types of files: a core file that includes temperature and salinity measurements from the conductivity-temperature-depth (CTD) sensor, and a b-file that includes measurements from all BGC sensors available. These two files are combined into a synthetic-profile file, which aligns or interpolates each measurement along a synthetic pressure axis. This process accounts for any misalignment of the CTD and BGC measurements during onboard processing, and thus greatly enhances the usability of the data while maintaining the character of the original sample design (Bittig et al., 2022). All synthetic-profile files from each float are merged into a single "Sprof" file, which contains the CTD and BGC data and associated quality control information.

The BGC-Argo QC procedures are structured under two main levels (Argo Data Management Team, 2022). The first level is real-time QC (RTQC) involving a set of automatic tests on each profile, with the goal of screening grossly bad data from the system (i.e., global range and spike tests). The second level is referred to as delayed-mode QC (DMQC), which aims at delivering high-quality data for research purposes, such as long-term studies testing for climate-driven changes in ocean biogeochemistry. DMQC involves a more detailed set of procedures that are performed by an expert to account for shifts in sensor calibration that can occur during storage and post-deployment. For O_2, NO_3^-, and pH, these adjustments are an essential part of the QC process, as they provide significant improvements to the accuracy of the raw data. Users

are always advised to use '<PARAM>_ADJUSTED' data fields, such as 'DOXY_ADJUSTED' for adjusted O_2 measurements, as described in Johnson et al. (2018), Johnson et al. (2021), Bittig et al. (2019), and Thierry et al. (2021). The DMQC procedures generally involve re-calibrating the sensor to high-quality reference fields or climatologies (Takeshita et al., 2013; Bittig and Körtzinger, 2015; Johnson et al., 2015; Maurer et al., 2021). These new calibrations are then propagated forward to provide higher-quality real-time data (called real-time adjusted data).

The DMQC procedures for the bio-optical parameters are currently still under development, although various methods have been explored (Organelli et al., 2016, 2017; Cornec et al., 2021; Jutard et al., 2021; Begouen Demeaux and Boss, 2022; O'Brien and Boss, 2022). However, all bio-optical parameters receive some level of real-time QC at this stage (Schmechtig et al., 2015, 2018, 2019; Poteau et al., 2019). The Chla parameter also receives an adjustment in real time, which includes a correction for non-photochemical quenching (NPQ), dark values, and an improved calibration factor (Roesler et al., 2017).

In this study, I report a census of select BGC measurements, and their associated data quality based on the Argo QC flagging system. While other variables are available, the main analysis focuses on the six key variables, the program aims to measure (NO_3^-, pH, Chla, b_{bp}, PAR, and E_d). When describing both adjusted and unadjusted measurements, I refer to the variable name (e.g., "Chla"); otherwise, I specify when adjusted or unadjusted data is specifically described (e.g., "adjusted O_2"). For O_2, NO_3^-, pH, and Chla, I refer to the adjusted data when reporting quality metrics, as the unadjusted data is intentionally treated as bad for scientific analysis (e.g., due to storage drift for the O_2, NO_3^-, and pH

sensors, or NPQ for Chla). Comparatively, for b_{bp}, PAR, and E_d, data are generally usable for scientific analysis without requiring further adjustments. For this analysis, I also only consider floats that simultaneously collect E_d at 380, 412, and 490 nm and PAR, which is the most common configuration in the BGC-Argo array. For brevity, I refer to these simultaneous measurements of PAR and E_d as PAR/E_d.

This paper describes the current breakdown of BGC profile quality in terms of data quality flags, what's been collected so far, annual trends in data quality, and how close BGC-Argo is to reaching its targets. I compare data quality before 2017 with that in the last six years to identify improvements in data quality. The density of quality BGC profiles is also assessed regionally and in relation to the target density of a 1,000-float network. Finally, I also discuss potential strategies for increasing the number of high-quality profiles in the future.

2.2 Methodology

For each profile and BGC parameter used in this study, I recorded the WMO number of the float, date and location, cycle number, profile- and depth-level quality flags, and the presence of sensor data using Sprof files downloaded from March 16–17, 2023 (Argo, 2000). I also recorded information about each sensor's manufacturer and model from the metadata file associated with each float (Argo Data Management Team, 2022). Data from 2023 was not included in this analysis. With the QC flags BGC-Argo provides, I applied two simplified flagging systems I created. I only used ascending profiles (~96% of the database) because QC flags and BGC data were not consistently available from descending profiles. For the rare occasion where a single float had multiple sensors measuring the same BGC property (e.g., 24 floats had more than one O_2 sensor), I used

the sensor designated as the primary parameter (see pg. 84 in Argo Data Management Team, 2022).

2.2.1 Description of BGC-Argo quality flag system

First, I provide a description of BGC-Argo's QC flag system which is based on the pre-existing flagging scheme used operationally within the Argo data management system. The QC flag system sets depth-level and profile-level quality flags for each BGC property (Table 1; Argo Data Management Team, 2022). The depth-level flag system in Argo denotes the QC flags as "<PARAM>_QC" or "<PARAM_ADJUSTED>_QC" for unadjusted or adjusted measurements, respectively. These QC flags will flag "good" data as "1", "probably good" data as "2", "probably bad" data as "3", and "bad" data as "4" (Table 1). Data are labeled with a flag of "5" when they are changed (e.g., the correction for NPQ of chlorophyll-a fluorescence). If values are interpolated or extrapolated, a label of "8" is used. If no QC is performed, a flag of "0" is used, while missing data are flagged as "9". Generally, data with flags "1", "2", "5", and "8" are treated as high-quality data, while data with flags "3" or "4" are treated as low-quality data.

Profile-level quality flags, denoted as "PROFILE_<PARAM>_QC" in Argo, describe the percentage of high-quality data points out of all the available data points in a profile (N). For the calculation of N, the QC flags associated with the adjusted data (from either adjusted RTQC or DMQC) are used. If there are no adjusted data available, the QC flags associated with the unadjusted data are used in the calculation instead (from unadjusted RTQC processing). Depth-level data points with flags "0" or "9" are not used in the determination of the profile-level flag. In Equation 1, the calculation for profile-level quality flags is as follows:

$$N = \frac{n_1 + n_2 + n_5 + n_8}{n_1 + n_2 + n_3 + n_4 + n_5 + n_8} \times 100\%, \quad (1)$$

where *n* is the number of QC flags in the profile with the subscript indicating the value of the depth-level QC flag. Then, *N* is categorized as one of seven different flags: flag "A" means when 100% of the profile has high-quality data, flag "B" when 75 to 100% of the profile has high-quality data, and so on in 25% increments to flag "F" which means that 0% of the profile data are high quality (Table 1). If no QC is performed or the only depth-level quality flags are "0" and "9", then no profile-level flag is given, and an empty value is assigned.

Table 1. Quality control system used by BGC-Argo (Argo Data Management Team, 2022). Note that depth-level QC flags of "6" and "7" are not used.

QC Level	Flag Label	Quality Control Meaning
Depth-level	0	No quality control is performed
	1	Good data. All real-time or delayed-mode tests have been passed
	2	Probably good data; this data can be used with caution
	3	Probably bad data; data may require adjustment, or the adjusted data are still bad
	4	Bad data that are unusable or likely cannot be adjusted
	5	Value changed
	8	Data estimated from extrapolation, interpolation, or another approach
	9	Missing value
Profile-level	A	100% of the profile's data has depth-level flags of 1, 2, 5, or 8
	B	75 to 100% of the profile's data has depth-level flags of 1, 2, 5, or 8
	C	50 to 75% of the profile's data has depth-level flags of 1, 2, 5, or 8
	D	25 to 50% of the profile's data has depth-level flags of 1, 2, 5, or 8
	E	0 to 25% of the profile's data has depth-level flags of 1, 2, 5, or 8
	F	0% of the profile's data has depth-level flags of 1, 2, 5, or 8
	" "	No quality control is performed, or usable depth-level flags are present

2.2.2 Measurement-quality metrics

For this analysis, I created two simplified systems of flags based on BGC-Argo's quality flag scales described in the previous section. Our first flag classification system is important for those interested in scientific analysis as it focuses on the availability of high-quality data profiles.

The second flag system I created describes the prevalence of functioning sensors, as opposed to those that have malfunctioned (e.g., the sensor stops reporting data or reports oceanographically inconsistent values entirely). Data profiles from malfunctioning sensors cannot be recovered for biogeochemical analysis and may be meaningless. The purpose of the second flag classification system is to identify causes of poor-quality data that result from an unfixable sensor malfunction, and not from intermittent error or other operational limitations. This flag scale is likely of interest to those who are currently deploying floats and those who plan to. Both flag scales provide a foundation for tracking BGC-Argo data quality and sensor performance through repeated future analyses.

2.2.2.1 Profile quality flag system

The first system of flags defines high-quality profiles as profiles where N is greater than or equal to 75% (so profile flags "A" and "B" as defined in Table 1). Low-quality profiles were defined as profiles where N is less than 75% (or having profile-level flags of "C", "D", "E", or "F").

I needed to identify the cause of missing QC flags in a profile, which can result from either the QC algorithm simply not being applied, or from the sensor no longer reporting data due to malfunction. To distinguish between the two possible causes, I checked for the presence of BGC data in the profile. If BGC data were missing, the profile was categorized as having an unresponsive sensor. If BGC data was present, the profile was labelled as having missing QC flags.

Based on these definitions, I calculated the percentage of high-quality profiles (P_{HQ}) by parameter, year, region, or for each float in Equation 2 as:

$$P_{HQ} = \frac{S_{HQ}}{S_{HQ} + S_{LQ} + S_{NR}} \times 100\%, \quad 2$$

where S_{HQ} is the number of high-quality profiles, S_{LQ} is the number of low-quality profiles, and S_{NR} is the number of profiles where the sensor was no longer reporting data. I repeat a similar calculation but for the percentage of low-quality profiles (P_{LQ}) and profiles with unresponsive sensors (P_{NR}). Note that the number of profiles without QC (S_{NOQC}) is not included in the calculation.

2.2.2.2 Functioning-sensor flag system

The second QC flag scheme created for this analysis classifies sensors as either functioning or malfunctioning. I use this scheme to describe the prevalence of functioning/malfunctioning sensors for each BGC parameter and sensor manufacturer/model.

I defined "malfunctioning sensors" as sensors that produced profiles where all data points in the profile had a depth-level flag of "4" or when the sensor reported no data in the profile. When data are labeled with a depth-level flag of "4", BGC data are outside the expected range, contain spikes, have unexpected gradients, or the measurements remain 'stuck' at the same value. Otherwise, if the sensor profile did not follow these conditions, the sensor was labeled as functional.

For this calculation, QC flags were produced from the combination of unadjusted or adjusted data for all BGC parameters. Profiles without QC flags and deemed as S_{NOQC} (as previously described) were ignored. In Equation 3, I calculated the percentage of functioning profiles as P_{FUNC} as:

$$P_{FUNC} = \frac{S_{FUNC}}{S_{FAIL} + S_{FUNC}} \times 100\%, \quad 3$$

where S_{FUNC} is the number of profiles with functioning sensors and S_{FAIL} is the number of profiles with malfunctioning sensors.

2.2.2.3 Float survival rate

The survival rate of floats and their sensors are an important aspect of maintaining the BGC-Argo network. Depending on various factors (e.g., power consumption, environmental conditions, manufacturing quality), some floats will collect only a few profiles before failing, while others will last several years. For similar reasons, sensors may stop functioning before the float does. The survival rates of floats (R_{Float}) can be quantified as the number of floats operating at a pre-defined cycle number divided by the number of floats originally deployed. As cycle numbers increase, the portion of floats remaining declines until no floats are active. Similarly, the portion of remaining floats that produce high-quality profiles at a pre-defined cycle number represents a combination of float and sensor performance and is termed the high-quality survival rate or R_{HQ}. The difference between R_{Float} and R_{HQ} is therefore representative of sensor performance alone. The same concept can be applied to the float profiles I label as 'functioning' (termed the functioning survival rate or R_{FUNC}).

I'm interested in estimating R_{Float}, R_{HQ}, and R_{FUNC} at 36.5 cycles (equivalent to one year of profiling at a 10-d profiling frequency). To determine R_{Float}, I first calculated the fraction of floats remaining at cycle numbers between one and thirty and then applied a linear regression to extrapolate the survival rate to 36.5 cycles. A similar calculation was performed for R_{HQ} and R_{FUNC} but only floats with high-quality profiles and with functioning sensors were counted, respectively. At a 10-d sampling interval, floats deployed after March 7, 2022, would not have been deployed for long enough to make 30

cycles, and are therefore not used in this calculation. Note that for these survival rate estimates, I relied on cycle numbers instead of profile numbers because 1) up- and down-cast profiles (if both were taken) are given the same cycle number, and 2) I only consider ascending profiles in this analysis.

2.2.3 Regional data density and coverage

The density and spatial coverage of BGC data are important for determining where regional biogeochemistry may need to be better constrained. I assessed these metrics in different marine regions (Flanders Marine Institute, 2021) which include the North Atlantic, South Atlantic, North Pacific, South Pacific, Indian Ocean, Southern Ocean, Arctic Ocean, Baltic Sea, Black Sea, and Mediterranean Sea. Floats in the Black, Mediterranean, and Baltic seas were also reviewed both individually and as a single region I call 'seas around Europe'.

I determined the density of high-quality profiles (equal to S_{HQ} divided by surface area) from both the total number of profiles available and on a yearly basis. The surface area of ocean was calculated for each marine region and from a global ocean grid resolved to 5º longitude by 5º latitude. For all regions, except for the seas around Europe, areas where the seabed was shallower than 200 m was excluded. I report the average number of high-quality profiles from PAR/E_d profiles since this BGC data comes from the same sensor and have similar numbers of high-quality profiles.

For the annual assessments, I compared the density of high-quality profiles with a target profile density of a BGC-Argo network of 1,000 active floats (assuming they are evenly-spaced). This comparison was made by calculating 1) the region-wide density as a percentage of target density, and 2) the percent area of grid cells where high-quality

profile density met the target density in each region. A similar calculation was also made for the latter but by including areas where profile densities are above 0. The target density is equal to ~1.1 profile per 10,000 km^2 per year (i.e., ~1 profile per 100 km x 100 km square of ocean per year) and is based on a network of 1,000 floats (presumably profiling every 10 days) over ~335 million km^2 of ocean each year.

2.3 Results

2.3.1 Overall BGC-Argo profile quantity

As of December 2022, the database of Sprof files has accumulated a total of 263,715 unique BGC profiles from 1,811 BGC-Argo floats (Table A1). The most frequently measured property is O_2 (251,855 raw profiles from 1,754 floats) while the least frequently measured property is pH (39,483 raw profiles from 447 floats) after PAR/E_d (46,028 raw profiles from 273 floats). Since 2002, the total number of floats deployed has steadily increased, alongside the total number of floats sustained in the array (Figure 1).

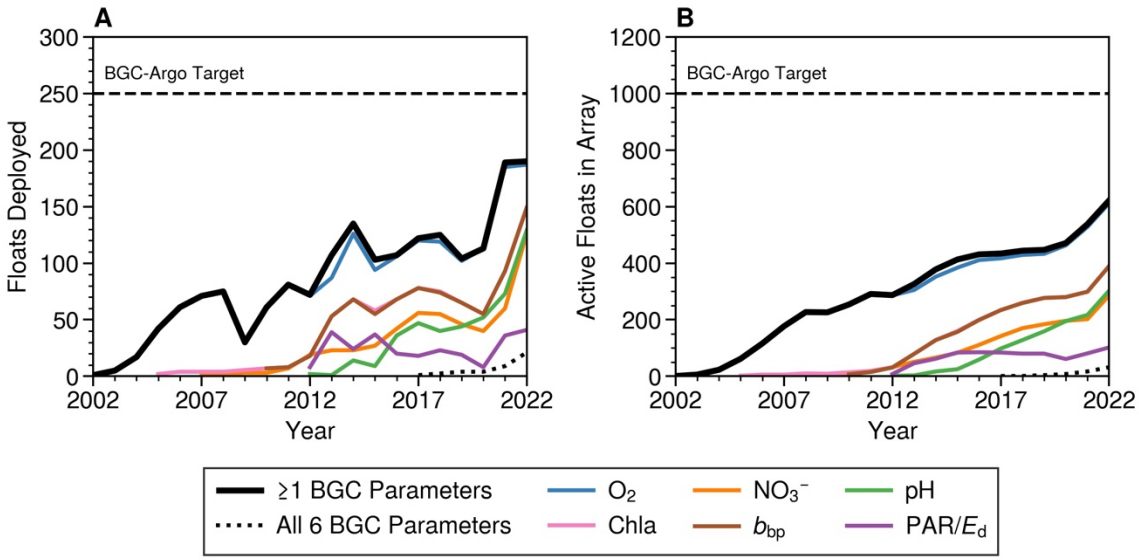

Figure 1. The number of floats deployed (**A**) and the size of the float array (**B**) each year since 2002. The solid black line represents floats with at least one BGC parameter, the dotted black line represents floats with all six BGC parameters (O_2, NO_3^-, pH, Chla, b_{bp}, and PAR/E_d), and the remaining colored lines represent floats with a specific BGC parameter. The BGC-Argo targets for annually deployed floats and the size of float array are shown in panels (**A**, **B**), respectively, as the horizontal dashed lines.

How close the float array is to the annual float or profile targets is highly dependent on the BGC parameter because most floats do not measure the full suite of BGC parameters. For example, the number of radiometer-equipped floats deployed each year has not surpassed 50, while the other five BGC parameters see a minimum of 100 floats deployed per year as of 2022. These discrepancies result from pilot programs that prioritized certain parameters. Radiometry has largely been driven by European and Australian projects, which focused on regions around Europe, the North Atlantic, and the Indian sector of the Southern Ocean.

Currently, only 39 floats measure all 6 BGC parameters of interest (Figure 1). As of 2022, PROVOR, one of the three main models of floats used in the BGC-Argo fleet, is the only float type that can measure all six variables, restricting the full set of parameters from being collected. However, many operational float programs are currently putting

effort toward expanding sensor suite capabilities on various platforms. For example, the Global Ocean Biogeochemistry (GO-BGC) array plans to begin deploying six-parameter APEX floats in the summer of 2023. A 6-parameter Navis float is currently in the later stages of development as well.

2.3.2 Overall BGC-Argo profile quality

The majority of profiles for each BGC parameter have received QC flags. Almost all O_2 profiles have undergone QC (P_{NOQC} = <1%). The parameters missing the most QC flags are Chla (P_{NOQC} = 12%) and b_{bp} (P_{NOQC} = 15%). This lack of QC on some parameters will decline as the program matures. The mode of QC received by each property also varies greatly (Figure 2). At least three-quarters of O_2, NO_3^-, pH, and Chla profiles have received adjusted or delayed-mode processing. In comparison, >40% of b_{bp} and PAR/E_d data contain unadjusted real-time processing (also see Figure A1). Note that the RTQC for PAR/E_d only involves a range test and that there is no procedure for real-time adjustments; if adjustments are made to the radiometry data, then only DMQC has been applied.

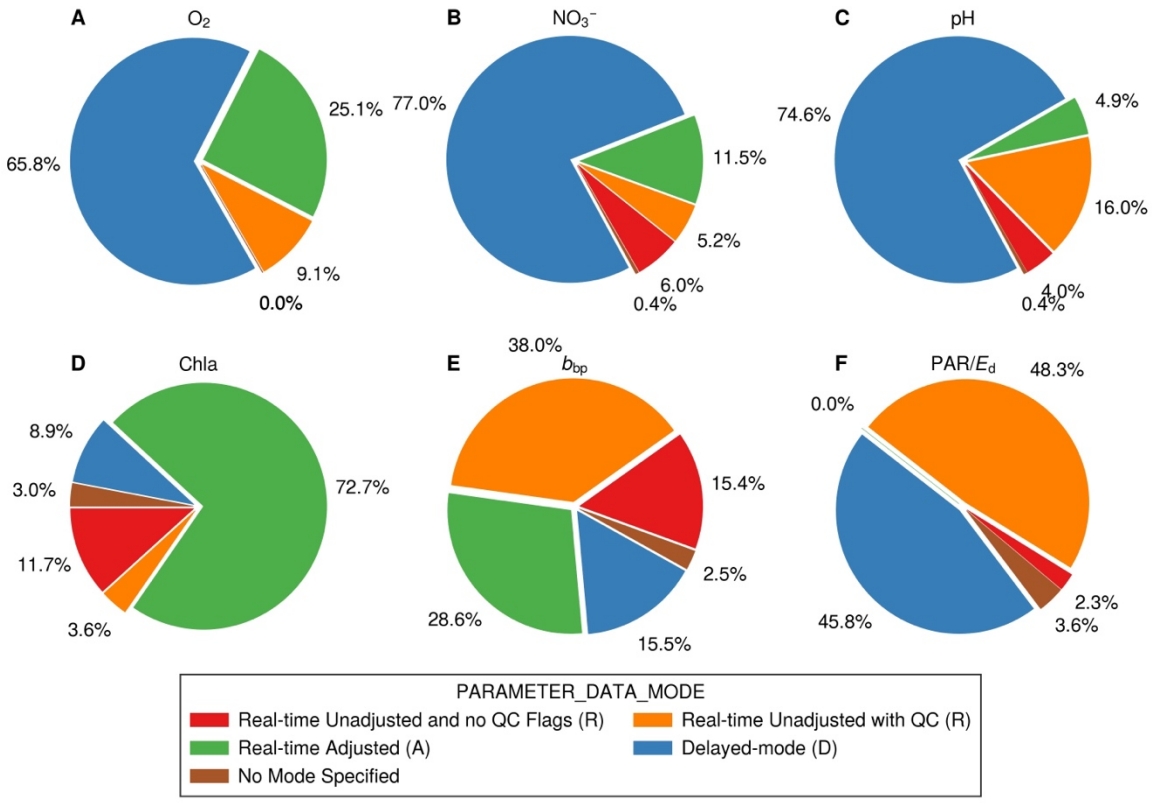

Figure 2. Percentage of profiles based on the type of quality-control mode, denoted in the PARAMETER_DATA_MODE field, for each BGC property: (**A**) O_2, (**B**) $\mathbf{NO_3^-}$, (**C**) pH, (**D**) Chla, (**E**) b_{bp}, and (**F**) PAR/E_d. The associated label from Argo notation for each data mode is shown in brackets in the legend. Note that some data with real-time unadjusted processing do not always have QC flags (also see Supplementary Note). Representations for specific downwelling light channels are the same as (**F**) and are reported in Figure A1.

Due to their specialized QC procedures, which limit the quality flag of "1" to data that has been adjusted, I report only the QC metrics derived from adjusted data of O_2, NO_3^-, pH, and Chla for the rest of this document, specifically referring to these variables as 'adjusted'. Otherwise, the QC metrics for the other parameters (b_{bp} and PAR/E_d) include both adjusted and unadjusted data, unless specifically stated.

Based on our first classification system, the number of high-quality profiles has generally increased each year, except for profiles of PAR/E_d (Figure 3). This lack of PAR/E_d profiles is due to no sustained rise in the deployments of floats equipped with

these sensors (Figure 1). I find that the database-wide P_{HQ} was the highest for PAR/E_d (92%, on average) and the lowest for adjusted pH (48%) (Table A2). Adjusted O_2 and NO_3^- profiles have a P_{HQ} equal to ~90% and 87%, respectively, while profiles of b_{bp} and adjusted Chla have P_{HQ} equal to 87% and 85%, respectively. For the ~21,000 adjusted PAR/E_d profiles that have received DMQC, P_{HQ} increases to ~97% (or 96.7% for PAR; 97.3% for E_d[380], E_d[412], and E_d[490]).

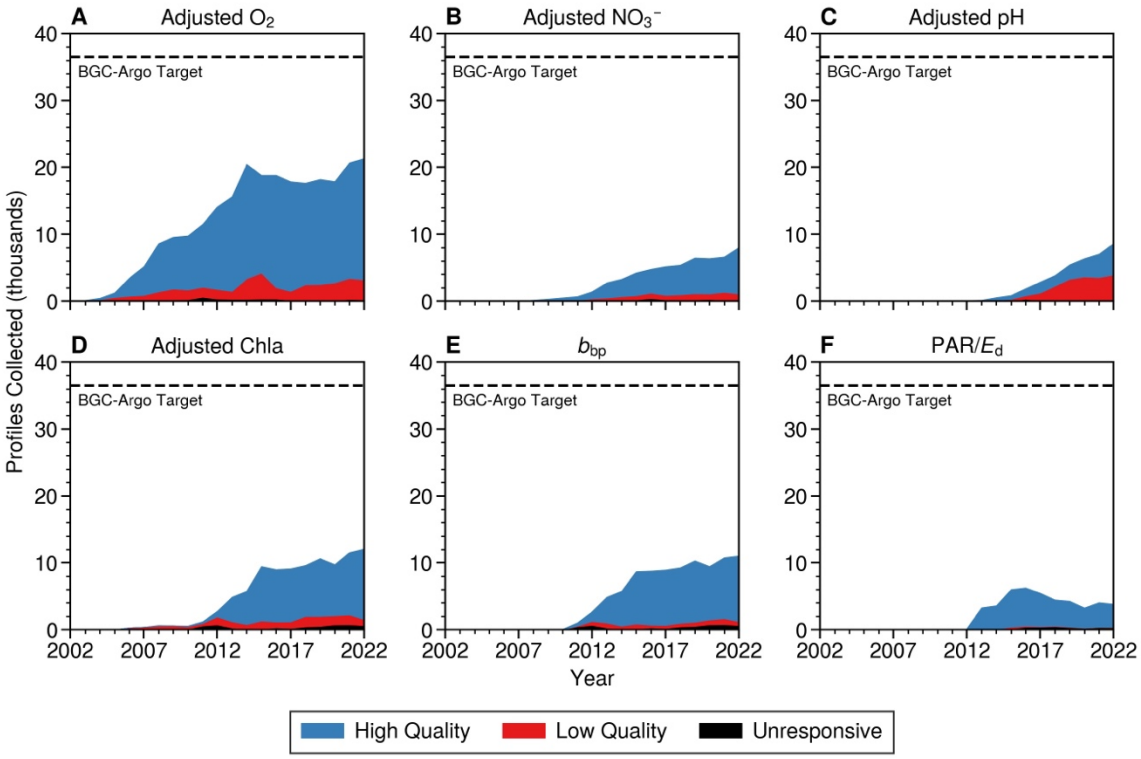

Figure 3. Profiles with QC collected each year for each BGC property: (**A**) adjusted O2, (**B**) adjusted NO_3^-, (**C**) adjusted pH, (**D**) adjusted Chla, (**E**) b_{bp}, and (**F**) PAR/E_d. Both unadjusted and adjusted data profiles are shown in (**E**, **F**). Profiles are colored by their quality-control flags. The BGC-Argo target for the number of profiles collected each year is shown in each panel as a horizontal dashed line. PAR and E_d are collected by the same sensor and undergo similar quality control, so, for simplicity, the average number of profiles per quality type are shown in (**F**) instead; the exact number of high/low-quality profiles between PAR and E_d profiles vary slightly (Table A2).

Low-quality data profiles were the least common with PAR/E_d (P_{LQ} = 2.5% for PAR; 1.8% for E_d[380]; 1.8% for E_d[412]; and 1.9% for E_d[490]). Low-quality adjusted pH

profiles are currently the most common (P_{LQ} = ~52%) among the BGC parameters. Other BGC sensors tend to report low-quality profiles 7–15% of the time. Profiles with no data (i.e., unresponsive sensors) are the most common among PAR/E_d and b_{bp} (P_{NR} = ~6% for each), while they are the least common among the adjusted O_2, NO_3^-, pH, and Chla profiles (P_{NR} < 1.5%; Table A2).

Using our secondary classification system, profiles with functioning sensors were the least common among pH profiles (P_{FUNC} = 60%; Table A2). This suggests that sensor malfunction is the cause of most low-quality pH profiles, rather than correctable calibration drift errors. Functioning sensors were present in a higher portion of profiles for O_2 (91%), NO_3^- (91%), Chla (94%), b_{bp} (88%), and PAR/E_d (P_{FUNC}= 93% for PAR, E_d[380], E_d[412], and E_d[490]).

2.3.3 Annual trends in profile quantity and quality

I first analyzed annual P_{HQ} by the year a profile was collected to summarize temporal trends in the BGC data quality available to users (Figure 4). Secondly, I estimated the survival rates after one year (R_{Float}, R_{HQ}, and R_{FUNC}) by year the float was deployed (Figure 5; Figure A2). The trends in R_{Float}, R_{HQ}, and R_{FUNC} by deployment year are useful for characterizing similar batches of floats/sensors (Figure 5; Table A3). With both data quality and survival rates, I compared pre-2017 values with the period of 2017 to 2022 to determine changes in the past six years with respect to the early stages of the program.

I find that annual P_{HQ} in the past six years was >80% for most BGC parameters, except for adjusted pH, which was between 40 and 60% and below pre-2017 levels (Figure 4). PAR/E_d profiles have an annual P_{HQ} that is always >85%, even though P_{HQ} in

the past six years is below pre-2017 levels. For the remaining parameters, the P_{HQ} values between 2017 and 2022 are generally close to or above pre-2017 levels.

Regarding survival rates, the annual R_{Float} and R_{HQ} can appreciably vary from year-to-year (Figure 5). Generally, R_{Float} is ~90% at 36.5 cycles, meaning that about 9-in-10 floats survive their first year. R_{HQ} tends to vary more and is more parameter dependent. R_{HQ} should always be equal to or less than R_{Float} because it is not possible for the sensor to record data if the float fails (the reverse is possible). The results show that R_{HQ} is typically <10% below R_{Float}. In some cases, R_{Float} is more than R_{HQ}, which I suspect results from sensors that temporarily become unresponsive or report bad data, before reporting good data in a successive profile, and the non-linear nature of float/sensor survival over time. Furthermore, R_{FUNC} follows the same patterns as R_{HQ} (Figure A2). This suggests that the cause of most low-quality profiles is not intermittent error or other operational limitations but rather sensor/cable damage, degradation, and/or bio-fouling.

R_{Float} for floats with pH sensors is similar to the R_{Float} of floats measuring other parameters. However, R_{HQ} derived from adjusted pH profiles had a distinct drop in 2017 and 2018 that was not associated with a decline in R_{Float}. This gap between R_{Float} and R_{HQ} for floats with pH sensors led to the accumulation of low-quality, adjusted pH profiles seen one-to-two years later in 2018 and 2019. Since then, the R_{HQ} has improved, resulting in an increase in P_{HQ} of adjusted pH profiles in the following years (Figure 4). This recovery in P_{HQ} and R_{HQ}, especially in 2022, puts pH on track to have similar data quality as the other five BGC properties.

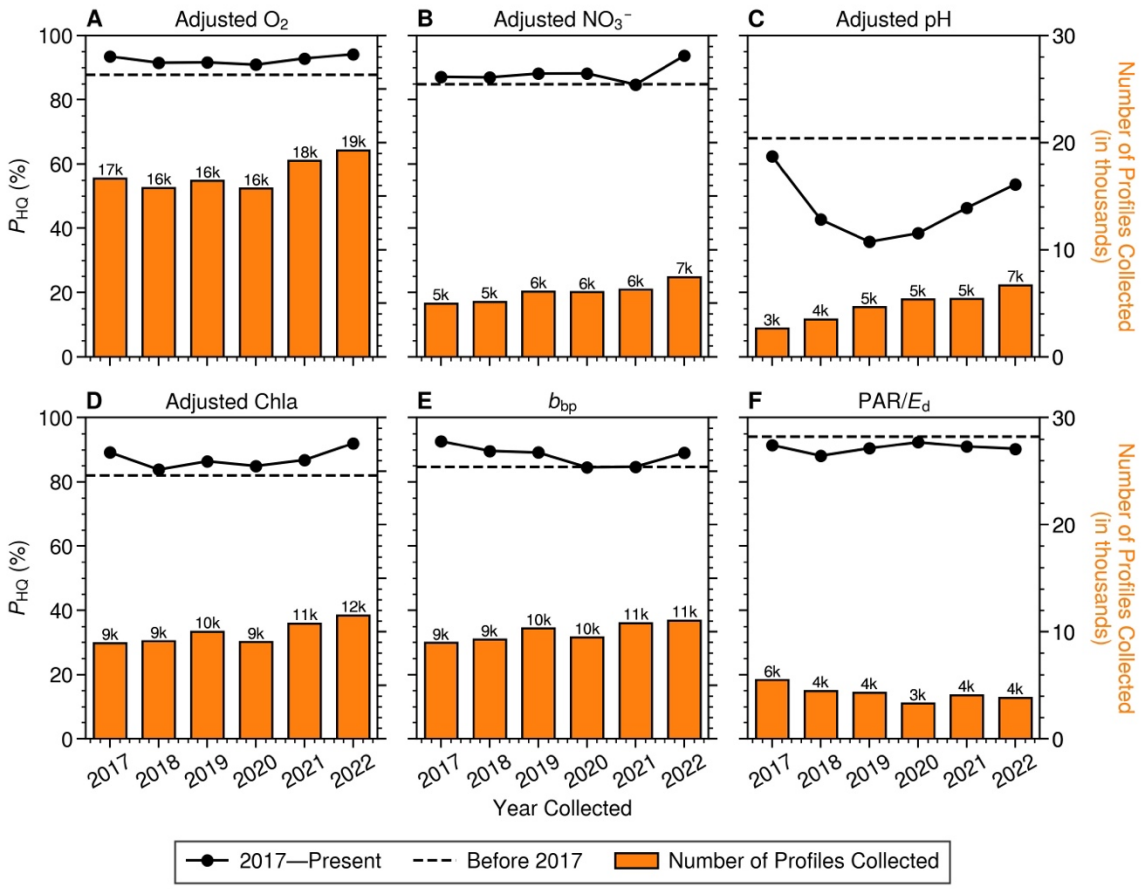

Figure 4. Percentage of high-quality profiles (P_{HQ}) for each year: (**A**) adjusted O_2, (**B**) adjusted NO_3^-, (**C**) adjusted pH, (**D**) adjusted Chla, (**E**) b_{bp}, and (**F**) PAR/E_d. The solid lines represent the annual P_{HQ} from 2017 to 2022. The number of profiles available each year is reported as the orange bar plot in each subplot, where the total number of profiles is indicated on the top of each bar. The dashed lines in each subplot represent P_{HQ} before 2017. The number of unique profiles collected before 2017 for ~127k for adjusted O_2; ~17k for NO_3^-; ~3.3k for pH; ~32k for Chla; ~32k for b_{bp}; and ~19k for PAR/E_d. DMQC for b_{bp} and PAR/E_d has been developed but is not yet fully implemented; a mix of adjusted and unadjusted data are shown for b_{bp} and PAR/E_d here.

A similar case may have occurred with b_{bp} from floats deployed in 2019. The R_{HQ} of b_{bp} was ~10% lower than the R_{Float} in 2019 and 2020 (Figure 5) and was followed by a decline in the P_{HQ} of b_{bp} profiles in 2020 and 2021 (Figure 4). This difference suggests that b_{bp} sensors failed before the floats did, which led to a disproportionate collection of low-quality profiles. However, a similar pattern in R_{HQ} was observed in adjusted Chla,

without a similar decline in P_{HQ} in 2020 or 2021. The decline in annual P_{HQ} of b_{bp} appears to have been corrected since 2022.

R_{Float} is generally close to the R_{HQ} for most parameters in most years. The similarity between the two rates explains why there is little variability in the P_{HQ} of adjusted O_2 profiles in the last six years. For the same reason, P_{HQ} for PAR/E_d profiles remains generally consistent from 2017 to 2022, despite both R_{Float} and R_{HQ} declining to ~70% in 2019/2020.

2.3.4 Regional profile quality

The density of accumulated BGC profiles is important to construct global climatologies (e.g., Cossarini et al., 2021; Sauzède et al., 2016). The number of float profiles, including those of high quality, are available in most marine regions (Figure 6) but at greatly varying densities (Table A4). The density of high-quality profiles varies among parameters as pilot programs prioritized certain types of sensors early on (e.g., radiometry in the North Atlantic and the Mediterranean Sea).

Generally, the marine regions that have accumulated the highest density of high-quality profiles are the seas around Europe (Mediterranean Sea, Black Sea, and Baltic Sea), the Arctic Ocean, and the Southern Ocean (Figure 6; Table A4), although these densities are highly parameter dependent. In the Arctic Ocean, sampling also has not occurred evenly throughout the region. There is a lack of floats between the Chukchi Sea and Fram Strait, leaving a large portion of the Arctic Ocean under-sampled.

The Southern Ocean has accumulated high profile densities for each BGC property due in large part to the success of the Southern Ocean Carbon and Climate Observations and Modelling (SOCCOM) project (Maurer et al., 2021; Sarmiento et al., 2023).

However, floats deployed as part of SOCCOM do not include radiometers, explaining the low level of PAR/E_d data in this region. Additionally, pH data coverage is also lower than the other parameters in this region, due to sensor quality issues highlighted in the previous section.

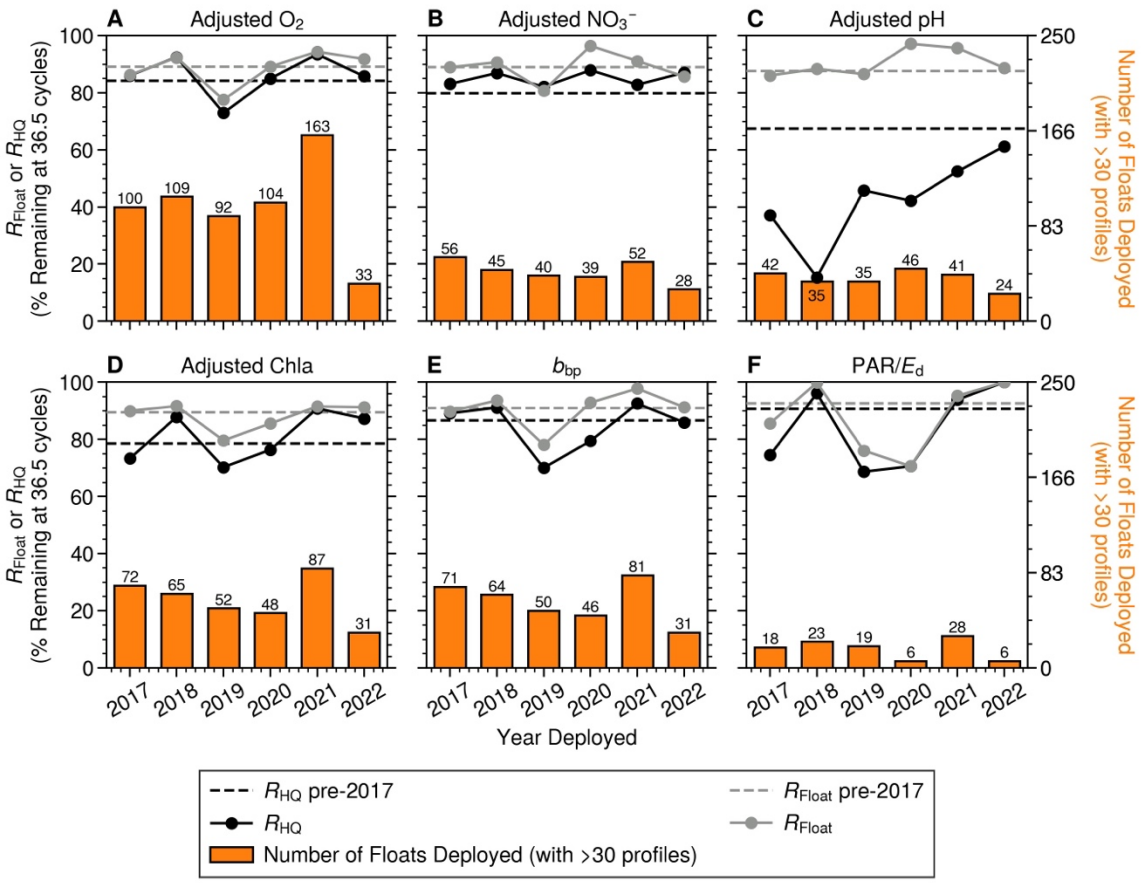

Figure 5. Survival rates of floats (R_{Float}) and high-quality profiles (R_{HQ}) by deployment year. Each of the six key BGC variables: (**A**) adjusted O_2, (**B**) adjusted NO_3^-, (**C**) adjusted pH, (**D**) adjusted Chla, (**E**) b_{bp}, and (**F**) PAR/E_d. The solid line represents R_{Float} (grey) and R_{HQ} (black) by year from 2017 to 2022. The horizontal dashed line in each subplot represents R_{Float} (grey) and R_{HQ} (black) before 2017. The number of floats with quality-controlled data (and adjusted data when relevant) deployed each year are reported as the bar plot at bottom of each subplot and on the top of each bar. The number of floats deployed before 2017 are 817 for O_2; 144 for NO_3^-; 60 for pH; 249 for Chla; 238 for b_{bp}; and 128 for PAR/E_d. Note that only floats deployed for more than 300 days before January 1, 2023, were used to standardize float lifetimes for the survival rate calculation (see Section 2.2.2.3).

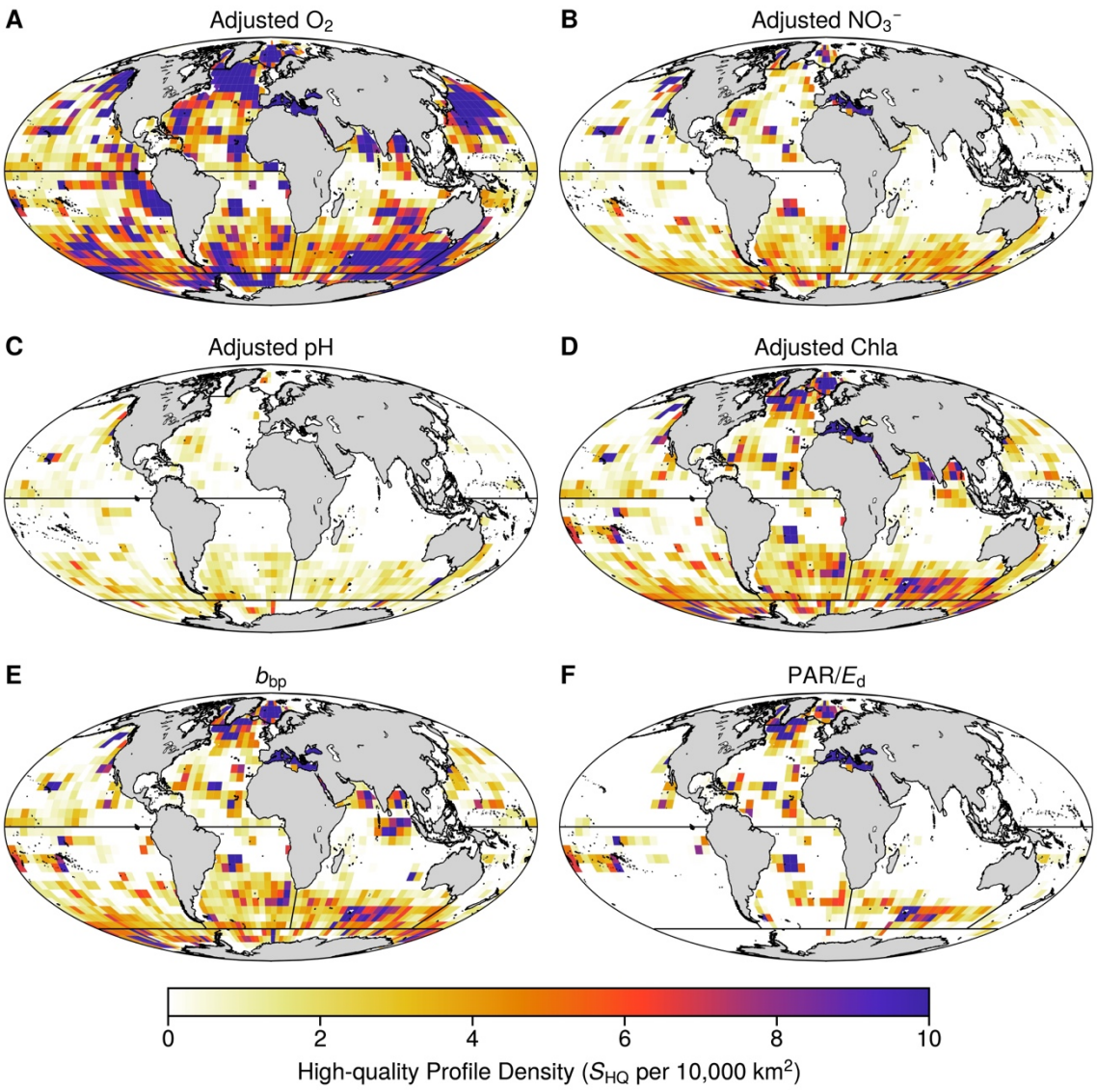

Figure 6. Density of high-quality profiles collected from 2002 to 2022 per 5°-by-5° grid cell for (**A**) adjusted O_2, (**B**) adjusted NO_3^-, (**C**) adjusted pH, (**D**) adjusted Chla, (**E**) b_{bp}, and (**F**) PAR/E_d. The black lines delineate the marine regions defined by Flanders Marine Institute (2021). Areas shallower than 200 m were removed, except for the Mediterranean, Black, and Baltic seas. Note that the target density for a full BGC-Argo network is ~1.1 profiles per 10,000 km² each year. The accumulated density of high-quality profiles in each marine region is described in Table A4.

For the major basins (Pacific, Atlantic, and Indian Oceans), the densities of high-quality profiles are generally lower than polar regions and the seas around Europe (Table

A4). Additionally, the high-quality, adjusted O_2 profiles are generally high compared to other BGC parameters collected in the same major basins.

With an annual global target density of ~1.1 profiles per 10,000 km^2 per year, the density of high-quality profiles is assessed on an annual basis to help evaluate the success of BGC-Argo (Figure 7; Figure A3; Figure A4). The annual, regional density of high-quality profiles, expressed as a percentage of the target density, highly varies between parameters and regions, although there is a general interannual trend of increasing profile densities. The percent area of each region with sufficient sampling also highly varies between parameters and regions. While there are significant year-to-year fluctuations, the general long-term trend is that profile densities and percent area coverage have been increasing since 2012.

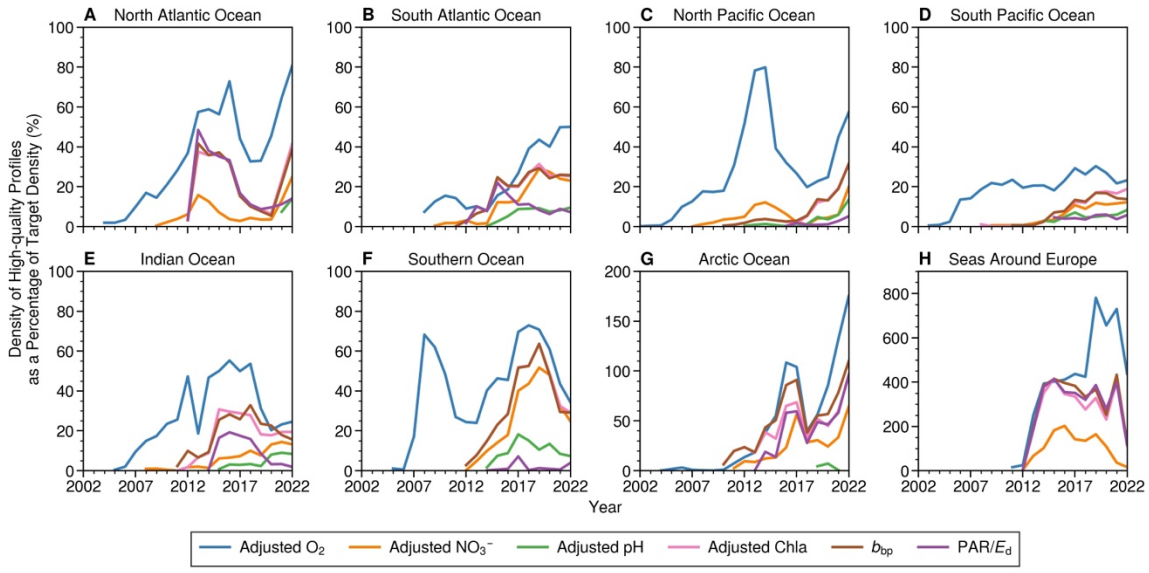

Figure 7. Density of high-quality profiles as a percentage of the targeted high-quality profiles per year with each BGC parameter in the (**A**) North Atlantic, (**B**) South Atlantic, (C**)** North Pacific, (**D**) South Pacific, (E**)** Indian Ocean, (**F**) Southern Ocean, (**G**) Arctic Ocean, and (**H**) seas around Europe. For regions in (**A**–**G**), areas shallower than 200 m were removed. The average number of high-quality profiles for co-located PAR and Ed profiles was used. In each region, sampling efforts are not evenly distributed (see Figure 8) nor may floats sample at 10-d intervals. Note the change in y-axis limits in (**G**, **H**).

BGC profiles in the seas around Europe far surpassed annual region-wide target densities at >100% in recent years (Figure 7) and meet target profile densities in ~70% of the area (Figure 8; Figure A4), except for profiles of adjusted pH and adjusted NO_3^-. For the parameters present, profile densities surpassed annual targets in the Mediterranean, Black, and Baltic seas individually (Figure A4). Considering that the marginal seas around Europe are more variable than much of the open ocean, a higher sampling effort may be needed to better constrain uncertainties. The Arctic Ocean has met target densities for most parameters in the last two years as well, however, this sampling is largely concentrated in an area that consists of 30% or less of the region. The high, region-wide densities (in both the Arctic Ocean and the seas around Europe) are partly driven by floats profiling more frequently than every 10 days, which leads to more

observations than what is expected from an annual target based on 10-d sampling intervals.

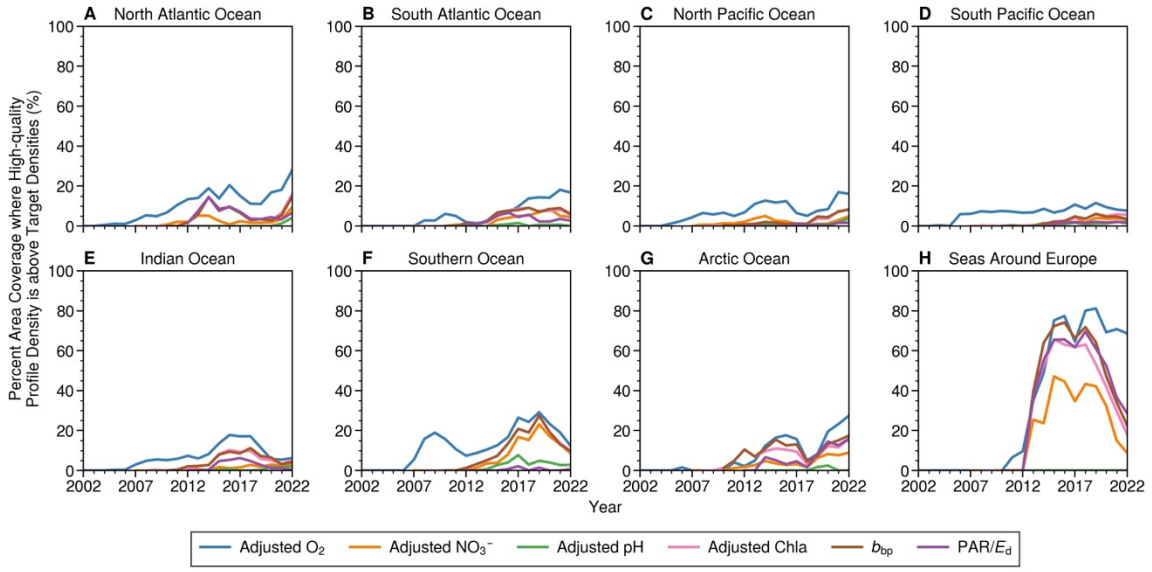

Figure 8. Percent area coverage where high-quality profile density is above target density for each BGC parameter in the (**A**) North Atlantic, (**B**) South Atlantic, (**C**) North Pacific, (**D**) South Pacific, (**E**) Indian Ocean, (**F**) Southern Ocean, (**G**) Arctic Ocean, and (**H**) seas around Europe. For regions in (**A**–**G**), areas shallower than 200 m were removed. The average density of high-quality profiles for co-located PAR and Ed profiles was used in density calculations.

The Atlantic, Indian, and Pacific oceans generally have reached 10 to 30% of target densities, region-wide, for most parameters. In the same regions, about 5 to 30% of the area has hit target densities. The ocean surface area in these regions with any amount of BGC data is much higher, generally reaching 30 to 60% of a region's area (Figure A4). For O_2, profile density and percent area coverage tend to be higher than other parameters. O_2 profile densities are between 50 to 70% of the target in the North Atlantic, North Pacific, and South Atlantic oceans in recent years, while the percent area coverage is <30%.

As is the case for all regions, region-wide profile densities are closer to the target density than when evaluating target density in terms of surface area covered. This

discrepancy means that the sampling effort is concentrated over a small portion of a region's area. Future float deployments could target these under-sampled regions, although, depending on scientific interest, concentrating sampling effort in certain areas may be needed for constraining highly variable regions (e.g., the Labrador Sea).

2.4 Discussion

The success of BGC-Argo is dependent on collecting and providing high-quality BGC observations of the ocean. The data quality summary provided herein was based on the pre-existing flagging scheme that is used operationally within the Argo data management system. It offers a quick synopsis of the current extent of high-quality BGC-Argo data directly available to users for scientific applications.

It is important to note that the various methods used in the QC of different BGC parameters, as well as the capability to adopt and implement new methods uniformly across Argo Data Assembly Centers (DACs), are still maturing. For example, there remain floats within the data system for which QC flags are missing (Figure 2). This lack of QC is due, in part, to limited resources in addressing management requirements for legacy floats, as one example. Additionally, for a portion of floats, the <PARAM>_ADJUSTED field is not filled. While it is advised to use the adjusted data when available, a lack of adjusted data does not necessarily mean the sensor is bad, and the data may receive an adjustment in the future. For b_{bp} and PAR/E_d, analysis can be performed without further adjustments, unlike O_2, NO_3^-, and pH data profiles, which require adjustments for proper scientific analysis. Similarly, the adjusted Chla data includes improved estimates of Chla. The unadjusted Chla profiles should not be used for the analysis of Chla. However, the unadjusted data can still yield other valuable scientific

information about the strength of NPQ and the photo-physiology of phytoplankton (e.g., Schallenberg et al., 2022; Ryan-Keogh et al., 2023).

The most efficient way to bolster the number of high-quality profiles available is to process existing profiles that have not received QC flags, so such floats should not be overlooked. As I reported in the results, QC flags are missing for 4–15% of BGC profiles, excluding O_2, which has QC flags assigned to almost all profiles. Processing these remaining profiles should increase the number of profiles labeled as high-quality, yet not significantly alter P_{HQ}.

Furthermore, efforts should be made to ensure all floats get processed (and reprocessed) with the most up-to-date QC procedures across DACs as protocols continue to be refined. This will result in improved consistency across the dataset into the future and strengthen its overall value for use in global analyses.

2.4.1 Parameter-specific improvements

In addition to refining quality flags through time and initiating data adjustments, there are further parameter-specific procedures that should be adopted by the data management team to further improve the absolute accuracy of BGC parameters. While high-quality profiles already represent more than 90% of adjusted O_2 profiles collected thus far, O_2 optode sensors suffer from slow response times, which are not routinely corrected within the data system. Slow sensor response times lead to a lag in true O_2 concentrations and can create errors on the order of ~10 μmol kg^{-1} (Bittig et al., 2014; Gordon et al., 2020). Fortunately, various methods exist for calculating the *in situ* response time of O_2 optodes, given the existence of certain ancillary data and/or sampling conditions (Bittig et al., 2014; Gordon et al., 2020). Such response time corrections will

help reduce uncertainties around the oxycline, although, it would not likely affect the assigned QC flags.

In situations where salinity sensor data are labeled with a flag of "4" (unrecoverable), O_2 data are given a label of "3" because salinity compensation to the O_2 measurements cannot be performed. In these cases, utilizing salinity profiles from a high-quality derived product may help recover more O_2 profiles. This procedure has been explored by the Argo community and will likely be implemented in the near future.

The pH sensors tended to fail far more than the other BGC sensors (Figure 4; Figure 5; Table A2). Since a significant portion of the processed pH data was given a QC flag of "4" or characterized as "malfunctioned", improvements to the P_{HQ} appear more limited by the technology. Accordingly, the community has continued to refine and improve the design of the pH sensor, leading to a steady increase in reliability over the past five years. Future, repeated analysis of the pH QC time series presented here should be performed to ensure that the upward trending pattern in P_{HQ} continues. It is important to note that even with relatively high failure rates, BGC-floats now collect substantially more pH profiles than shipboard measurements, playing a critical role in understanding the ocean carbon cycle.

Float fluorometers currently rely on a lab-based calibration of fluorescence-to-Chla. The conversion of fluorescence to in situ Chla concentration depends on both the composition of the phytoplankton community and their physiological status (Cullen, 1982). Ideally, the relationship between fluorescence and Chla is determined using water samples collected at the deployment site. However, this approach is not the most cost-effective, and any relationships determined at the time of deployment will likely not be

the same once seasons change or the float drifts into an ecologically distinct region. Currently, each fluorometer is calibrated in a laboratory setting, using a reference fluorometer that was initially calibrated to a single culture of *Thalassiosira weisflogii*. This calibration has introduced a bias in the determination of Chla *in situ*. Roesler et al. (2017) quantified this bias with WET Labs ECO sensors and Chla concentrations determined by high pressure liquid chromatography (HPLC). Using their analysis, BGC-Argo adjusts Chla data by dividing unadjusted Chla by two, to reduce this global bias. While this adjustment does not account for regional or seasonal changes in the fluorescence-Chla relationship, nor greatly affects how QC flags are applied, it is a step forward for gaining more accurate estimates.

An important effort is made by the Argo Data Management Team to calibrate and qualify fluorescence data measured from BGC-Argo floats in order to deliver Chla with the best possible accuracy. It has been shown that using radiometric data associated with fluorescence measurements is an effective way to improve the fluorescence calibration (Xing et al., 2011; Xing et al., 2018). However, not all BGC-Argo floats are equipped with radiometers, making it impossible to calibrate the entire fleet homogeneously. Recently, new methods based on machine learning have made it possible to derive radiometric profiles, from merged satellite ocean color observations and hydrological data, for any BGC-Argo float, whether equipped with a radiometer or not. These synthetic radiometric profiles can thus be assigned to the fluorescence profiles to consistently calibrate the whole BGC-Argo fleet. This method is a promising alternative to other possible approaches that obtain seasonal/regional adjustments tuned to space-

based estimates at the surface (Boss et al., 2008; Lavigne et al., 2015), or to HPLC Chla data.

Since the global adjustment factor is also only applicable for WET Labs (now Seabird) ECO sensors, other sensors may have to be calibrated to Chla following a different procedure and may behave differently when compared to WET Labs sensors. Subsequently, new sensors will most likely require different adjustment factors. One way to assess sensor/model-dependent adjustment factors could be to deploy some floats with multiple models of fluorometers to cross-calibrate between sensors. To catch the possibly wide range of variability in these adjustments, float deployment should be undertaken in various open ocean areas covering a wide range of biogeochemical and trophic conditions (e.g., from oligotrophic subtropical gyres to high latitude environments with strong seasonal changes in biomass). This cross-calibration could then be used to convert all Chla measurements to a common unit, assuming that differences between the same models of fluorometers are negligible. Similarly, a standard calibration procedure could be developed for BGC-Argo floats to ensure all Chla derived from fluorescence measurements from various models are intercomparable (e.g., with diffuse attenuation coefficient estimates from irradiance profiles). Regardless of which technique is applied, great care will need to be taken to ensure the interoperability of the resulting Chla concentration data so that the researchers can leverage the full database at once.

Measurements of b_{bp} from floats currently have a limited QC procedure that includes processing for range filters, data spikes, and bad offsets. Additional real-time QC procedures proposed by Dall'Olmo et al. (2023) will be integrated into BGC-Argo data processing soon and will likely change the proportion of QC flags in the system. Briefly,

this new procedure identifies issues such as noisy b_{bp} data, profiles with a large fraction of missing data, and profiles with negative b_{bp}. Potential sensor malfunction or biofouling is also identified by setting a threshold for high deep values of b_{bp}, where b_{bp} is expected to be very low (but not equal to zero). Dall'Olmo et al. (2023) also describe a procedure that identifies biased measurements of b_{bp} resulting from particles that have accumulated on the float while the float is parked at depth between casts. For those interested in data spikes (e.g., Briggs et al., 2011) or high b_{bp} at depth, both of which could result from real oceanographic phenomena, users will likely want to apply custom QC procedures. Once implemented, these added real-time QC procedures will reduce the number of falsely identified high-quality profiles available, but also erroneously identify good data as bad. Efforts should be made in developing a DMQC procedure to improve data quality flagging.

I found that high-quality PAR/E_d profiles represent ~90% of the entire database (Table A2). The data from radiometers are generally good without much QC. (Radiometry RTQC currently involves a global range test, and all radiometry data are given a QC flag of "2" unless the test is failed.) Previously tested improvements to the float radiometry processing include a dark offset correction, temperature correction, spike removal, and sensor drift detection (Organelli et al., 2016, 2017; Jutard et al., 2021; O'Brien and Boss, 2022). About half of the database has DMQC processing correcting for temperature and dark values (Jutard et al. 2021) but has not yet been implemented on all floats. Future float deployments should prioritize collecting nighttime profiles of PAR/E_d, at least once a year by each float, for these temperature and dark offset corrections (Jutard et al., 2021). In a similar sense, collecting these nighttime profiles

could also prove beneficial for assessing NPQ corrections. To reduce space-time biases in such an assessment without changing the standard profiling interval, average daily cycles could be extracted (Johnson and Bif, 2021; Stoer and Fennel, 2023).

Unstable sea states, clouds, and wave focusing can also momentarily alter light conditions which can lead to large fluctuations in the downwelling light profile. While there is nothing inherently wrong with the sensor during such events (as it represents natural light variability), stable light conditions are needed to better characterize the optical properties of the water column (e.g., estimation of the light diffuse attenuation coefficient). Procedures to identify these effects have been successfully applied to floats before (Organelli et al., 2016, 2017) and could be further developed to create a reference dataset for use in the ocean optics community.

2.4.2 Pre-deployment strategies

A few pre-deployment strategies can also be taken to help improve BGC data quality in the future. For one, testing the float from a dock could help identify issues with sensors, communications, and mechanics before deployment in the open ocean. Ideally, dock testing would prevent the deployment of floats that would otherwise quickly fail in the field. This strategy has proven to be very effective for the SOCCOM and GO-BGC projects. Secondly, while not always logistically feasible, reducing the time between when the float is manufactured and deployed may improve float survival and functionality by limiting exposure to possible damage. Finally, larger batteries can also be purchased for some float models to increase the float's lifetime, allowing the float to collect more high-quality profiles (assuming all sensors continue to function).

2.5 Conclusion

BGC-Argo is a rapidly expanding global ocean observation network that offers an independent, cost-effective approach to studying ocean biogeochemistry. The success of BGC-Argo depends on ensuring that scientific-quality data can be retrieved and delivered to the user in near-real time. Delivering scientific-quality data requires rigorous QC. Alongside increasing profile numbers and spatial coverage, I report that for most of the key BGC parameters, high-quality profiles make up at least 80% of all profiles collected thus far, with the exception of pH. I find that pH profiles collected over the past five years have drastically improved in quality and are on track to have a similar data quality as the other BGC parameters. I suggest several ways in which the BGC-Argo data system is improving, which should lead to both an increase in the number of high-quality profiles available to users, as well as improvements to the absolute accuracy of key parameters in the future. These strategies involve ensuring that data from all new and old floats contain flags with the most up-to-date QC procedures, advancing parameter-specific corrections, and testing the float before deployment. This census provides the foundation necessary to monitor measurement quality and quantity in the future as BGC-Argo advances.

Chapter 3

ESTIMATES OF NET PRIMARY PRODUCTIVITY USING DAILY CYCLES OF CARBON BIOMASS FROM PROFILING FLOATS[†]

3.1 Introduction

Marine net primary productivity (NPP), the rate of photosynthetically produced organic carbon available to heterotrophs (Lindeman, 1942), sustains marine life and contributes to the sequestration of atmospheric carbon in the deep ocean. Global warming may decrease NPP in the ocean because of increased stratification, lower nutrient availability, and changes to the phytoplankton community (Henson et al., 2021), altering the ocean's carbon sink and food webs (Riebesell et al., 2009). The traditional approach

[†]This chapter and Appendix B are a modified version of the article titled "Estimating ocean net primary productivity from daily cycles of carbon biomass measured by profiling floats" by Adam Stoer and Katja Fennel in Limnology and Oceanography Letters published by Wiley Periodicals LLC on behalf of the Association for Sciences of Limnology and Oceanography on December 1, 2022 under the terms of CC BY 4.0, which permits the use, distribution, and reproduction in any medium, provided the original work is properly cited.

to determining marine NPP is to incubate water samples in bottles with added inorganic, radioactively labelled carbon and measure its conversion to biomass (Steemann Nielsen, 1951). However, this technique is costly, time consuming, and requires the presence of a ship thus limiting where and how often the ocean can be measured. In contrast, satellite-based approaches can provide daily, global images at kilometer-scale resolution but can only measure a small portion of the sunlit surface ocean (Gordon and McCluney, 1975) and do not observe NPP directly, instead relying on strong assumptions and abundant direct measurements for ground truthing (Behrenfeld and Falkowski, 1997). Monitoring global changes in NPP requires well-resolved, basin-scale observations spanning decades, which neither of the above approaches can provide.

Phytoplankton photosynthesis depends on sunlight. During the day, photosynthesis (measured as gross primary productivity or GPP) typically dominates over autotrophic and heterotrophic respiration (termed community respiration or CR), leading to a net conversion of CO_2 and water to carbon biomass and O_2. At night, photosynthesis is absent resulting in the net production of CO_2 and water from C and O_2 via CR. The resulting daily pattern in these products is sinusoidal in shape and phase locked to the solar light cycle. One can infer GPP and CR by integrating the changes in these metabolites over a 24-hr cycle (Siegel et al., 1989; Barone et al., 2019), assuming biological processes dominate, and respiration is constant throughout the day (see discussion in Barone et al., 2019). While these assumptions are convenient for simplifying processes, constant community respiration could be violated (e.g., grazing is likely not constant throughout the day due to diel vertical migration).

The concentrations of both particulate organic carbon (POC) and O_2 are measured autonomously by the BGC-Argo array: a global array of floats profiling the top 2,000 m of the water column about every 5 or 10 days (Claustre et al., 2020). When profiles are collected at intervals that are not a multiple of 24 hours, every hour of the day is measured over a float's lifetime. With sufficient floats deployed, daily cycles of key oceanographic variables can be extracted from the ensemble (Gille, 2012; Johnson and Bif, 2021).

Here, I demonstrate that daily cycles of particle backscatter or b_{bp}, a bio-optical proxy for POC, can be used to estimate NPP ($NPP_{b_{bp}}$) using BGC floats. I build on the recent work of Johnson and Bif (2021), who estimated gross oxygen productivity (GOP) and NPP ($NPP_{\Delta O_2}$) using daily cycles in oxygen anomaly (ΔO_2) from the BGC-Argo array. Bio-optical proxies for particulate organic carbon (POC), such as beam attenuation and b_{bp}, are known to exhibit a daily periodicity too (Siegel et al., 1989; Kheireddine and Antoine, 2014; Barbieux et al., 2022). These daily particulate cycles have previously been used to estimate gross carbon productivity (GCP), but not NPP. Here I apply the technique to both float-based POC and ΔO_2 collected for the past decade, providing two independent but complementary estimates of NPP for the regions south of 30°S and south of 50°S (or the Southern Ocean).

3.2 Methodology

3.2.1 Float data

The BGC-Argo float profiles used for this analysis (Figure 9) came from the December 2021 snapshot (Argo, 2021). Only floats equipped to measure either b_{bp} or O_2

and with a mean latitude (over the float's lifetime) south of 20°S were processed. I used adjusted O_2 because it included corrections for sensor drift and calibration error by either in-air O_2 measurements from the floats (Johnson et al., 2015) or climatological O_2 data between 1,500 and 2,000 m depth (Takeshita et al., 2013). No attempt was made to correct for the response time of the sensor (Bittig et al., 2014; Gordon et al., 2020). Only data with quality flags of 1 or 2 (representing 'good' and 'probably good') for time, CTD (conductivity, temperature, and depth), and b_{bp} were used. Adjusted O_2 data used here had flags 1, 2, or 5. To reduce the influence of spikes, I discarded b_{bp} data greater than 0.03 m^{-1} as these would result in highly unlikely POC values. I then applied a 5-point running minimum filter followed by a 5-point running maximum filter to each b_{bp} - profile. Float data were then binned at a 10-m resolution from the surface to 200 m depth. Profiles were constructed from the median of each depth bin and then linearly interpolated to fill up to 2 missing data points (spanning 20 m); excluding the interpolation of surface data when the float did not reach the surface. These steps resulted in 56,885 profiles of O_2 from 436 floats and 34,318 profiles of b_{bp} from 256 floats between 2010 and 2020.

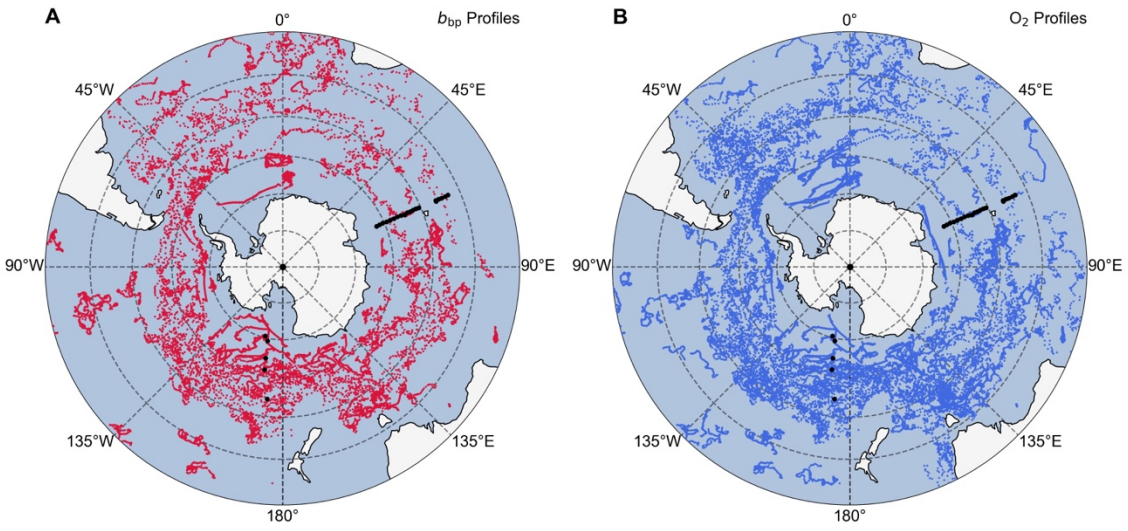

Figure 9. The locations of (**A**) b_{bp} and (**B**) O_2 profiles collected from 2010 to 2020 by biogeochemical Argo floats below 30°S. These profiles are used to construct daily cycles of POC and ΔO_2. Shipborne radiocarbon NPP measurements from Marra et al. (2021) and Mattei and Scardi (2021a) are represented by black circles. Circular grid lines represent 10° increments in latitude.

3.2.2 Construction of daily cycles

For $NPP_{\Delta O_2}$, I followed Johnson and Bif (2021) in using the ΔO_2 instead of O_2, and calculated ΔO_2 as the difference between observed O_2 and O_2 saturation ($O_{2,sat}$; Garcia and Gordon, 1992):

$$\Delta O_2 = O_2 - O_{2,sat}. \quad (4)$$

For estimates of $NPP_{b_{bp}}$, b_{bp} data were converted into POC equivalents. I converted b_{bp} from 700 nm to 470 nm using a power law relationship with a spectral slope of 0.78 (Boss et al., 2013; Boss and Haëntjens, 2016):

$$b_{bp}[470] = b_{bp}[700]\left(\frac{470}{700}\right)^{-0.78}. \quad (5)$$

Then, POC was estimated from b_{bp} at 470 nm using an empirical relationship (Graff et al., 2015):

$$\mathrm{POC} = 48811 \times b_{bp} - 24. \quad (6)$$

Floats with oceanographically inconsistent b_{bp} or O_2 were discarded from the analysis. I discarded O_2 data from float #5905030 and those listed in Johnson and Bif (2021), as well as b_{bp} data from eight floats (#1901329, #5903649, #5903630, #5904882, #5904218, #5905023, #5905396, #5905165, and #5903629). These floats exhibited sudden large changes in b_{bp} or had indications of sensor drift. I then discarded any profiles taken in areas with a water depth less than 2,000 m as defined by the ETOPO5 topography (NOAA, 1988) because O_2 profile calibrations require reference measurements at this depth (Takeshita et al., 2013).

To construct the daily cycles, I only used floats that sampled each hour of the day nearly equally throughout their lifetime (Figure 9). To identify these floats, I first calculated the number of unique hours that each float observed throughout its lifetime. Then, if the float contained observations from at least 21 different hours, the total number of profiles collected by the float was calculated and divided by 24. This quotient is the number of profiles that are expected for each hour of the day if the float was profiling with no bias for any hour of the day. Floats that sampled any hour of the day more than three times this expected number were discarded. Note that with more unique hours, hourly data is more equally spread throughout the day, but fewer floats are used so spatial or seasonal biases within each hour of sampling may be more prominent. A total of 29,874 profiles from 202 floats carrying O_2 sensors and 15,972 profiles from 111 floats carrying b_{bp} sensors met these criteria. Note that float profiles of b_{bp} have mostly come from the last five years (Figure B1).

Daily cycles of ΔO_2 and POC were constructed for latitudinal, seasonal, and depth bins (Figure 10). Floats were grouped into 10° bands from 30 to 70°S and by season in the 30–50°S region. Additionally, I compared the daily cycles of all profiles that contained both O_2 and b_{bp} measurements from 30 to 70°S (n = 13,037). The median and standard error of ΔO_2 and POC were calculated for each local hour of the day and each latitudinal, seasonal or depth subset, as described above. For every 'day', the 24-hourly data points were concatenated three times before applying a 3-point running mean. The center 24 data points of the smoothed time series are used for productivity calculations.

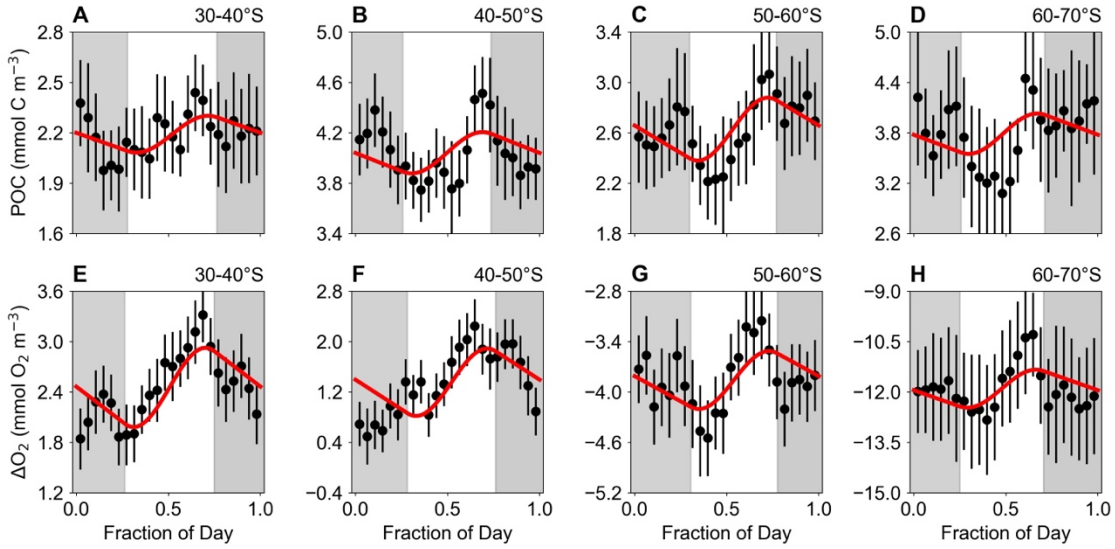

Figure 10. The annual daily cycle of median (**A**–**D**) POC and (**E**–**H**) ΔO_2 at hourly intervals (black points) in the upper 10 m of the water column. All sinusoidal fits (red curves) are significant below the 0.1 significance level, except for **D**. The gray shaded regions represent nighttime. Error bars (black vertical lines) represent one standard error. For panels **A**–**D**, R^2 = 0.34, 0.23, 0.47, and 0.17, respectively. For panels **E**–**H**, R^2 = 0.60, 0.46, 0.38, and 0.33, respectively.

3.2.3 Primary productivity calculations

I calculated GOP and GCP from the median daily cycles of ΔO_2 and POC, respectively. Johnson and Bif (2021) simplified their calculations by assuming that all

variation in ΔO_2 was due to metabolism. In a similar sense, I assumed that all variation in b_{bp} was driven by POC, and that all variation in POC was from C_{org}. These assumptions do not consider how daily variations in particle size or refractive index can affect the POC:b_{bp} ratio (Poulin et al., 2018), or the variable contribution of C_{org} to the POC pool (Graff et al., 2015).

Using the algorithm from Johnson and Bif (2021), a modified version of a previously published algorithm (Barone et al., 2019), NPP was then calculated. The model assumes that CR is equal to GPP:

$$P(t) = P_0 + GPP \times (f(t, E) - t). \quad 7$$

where $P(t)$ is the model fit to either POC or ΔO_2 at local hour t, P_0 is the POC or ΔO_2 at the start of the day, GPP is either GOP or GCP, and, using the sinusoidal option, $f(t, E)$ describes the variability in GPP throughout the day as a function of t and light intensity (or E). The standard error of the fit was estimated by bootstrapping the residuals (Barone et al., 2019). The difference between GPP and CR in a single day is thought to be at most 10 to 20% of GPP or CR (Barone et al., 2019). This difference contributes to the error in the productivity estimates when assuming GPP is equal to CR.

The latitude, longitude, and date are needed for determining the daily light cycle and GPP. For all subsets, the median longitude and latitude were used. For seasonal subsets, the midpoint date of the season was used, and for annual climatologies, I used day of year 90 from 2016 (which represents the average annual light cycle). I fit the model to the hourly medians to better approximate the center of each hourly bin, avoiding outliers. I converted GOP to NPP using an empirical GOP:NPP ratio of 2.7 mol O_2 (mol C)$^{-1}$

(Marra, 2002; Johnson and Bif, 2021). From ΔO_2 measurements, $NPP_{\Delta O_2}$ was calculated as:

$$NPP_{\Delta O_2} = \frac{GOP}{2.7}. \quad 8$$

Phytoplankton produce both POC and DOC during photosynthesis, however, the b_{bp} -sensor only measures the particulate portion. Using the data reported by Moran et al. (2022), I calculated an average percent extracellular release (PER; equal to the contribution of dissolved primary production to total primary production) of ~31% (see Supplementary Table 1 in Moran et al., 2022). Therefore, I assumed that ~30% of NPP was from dissolved primary production. I converted GCP to GOP using a PQ of 1.4 (Laws, 1991), assuming that growth was primarily new. Then, $NPP_{b_{bp}}$ was calculated as:

$$NPP_{b_{bp}} = \frac{GCP \times PQ}{2.7 \times (1 - (PER))}. \quad \mathbf{9}$$

where PER is equal to 0.3.

I used the seasonal climatological means of euphotic depth (z_{eu}) from the entire MODIS satellite mission at a 9-km spatial resolution (Lee et al., 2007; NASA, 2022). The euphotic depth data from MODIS is defined as the depth where light is 1% of its value at the surface. More realistically, an absolute light level should be used for future work. Euphotic-depth-integrated NPP (ΣNPP) was calculated as the sum of NPP from the surface to z_{eu}, but excluding the bin that contained z_{eu}, and multiplied by the width of the depth bins (10 m). For each subset, I calculated the average z_{eu} from the satellite data, discarding measurements where the seabed is shallower than 2,000 m. Negative NPP or estimates made with insignificant fits were included in the vertical integration to avoid biasing of ΣNPP (Barone et al., 2019). The standard error of the depth-integrated values was calculated as the square root of the sum of squared standard errors. Total annual NPP

comes from multiplying ΣNPP in each zone by the surface area where the seabed is below 2,000 m (NOAA, 1988).

Annual mean NPP from multiple satellite-based models were calculated using data available on the Oregon State University Productivity site (http://sites.science.oregonstate.edu/ocean.productivity/index.php). I downloaded the monthly means from 2010 to the end of 2020 derived by the VGPM (Behrenfeld and Falkowski, 1997), CbPM (Westberry et al., 2008), and CAFE (Silsbe et al., 2016) models. Since higher latitudes contain missing data points, I calculated the average ΣNPP pixels for each 10° latitude after removing values where the seabed was less than 2,000 m.

3.2.4 Sensitivity analysis

A sensitivity analysis was performed to test the effect of different parameter choices on the NPP calculations (see Table B1). I tested the median or the mean, the minimum number of unique local hours, how the outliers are defined, the type of model used, b_{bp}-to-POC conversion algorithms, alternative spectral slopes, the depth of the euphotic zone, and how the analysis changes with an additional year of data (from 2021). I recorded the total NPP in the 30–70°S and 50–70°S regions, whether negative ΣNPP was obtained at any latitude, the mean R^2 from each curve fit made within the euphotic zone, and the slope, R^2, and significance of the relationship (using a least-squares linear regression) between $NPP_{b_{bp}}$ and $NPP_{\Delta O_2}$ shallower than z_{eu}.

3.2.5 Bootstrapping analysis

A bootstrapping analysis was performed by randomly selecting different numbers of profiles from all O_2 and b_{bp}-profiles within 30–70°S. The number of randomly selected

profiles ranged from 500 to 12,000 profiles. I then calculated $\Sigma NPP_{b_{bp}}$ and $\Sigma NPP_{\Delta O_2}$ for each random selection. For each interval, I repeated the analysis 1,000 times. The mean and standard deviation of $\Sigma NPP_{b_{bp}}$ and $\Sigma NPP_{\Delta O_2}$ at each interval was calculated, which was used to describe a noise-to-signal ratio (equal to one standard deviation divided by the mean).

3.3 Results and Discussion

Profiles of $NPP_{b_{bp}}$ and $NPP_{\Delta O_2}$ measured between 30–70°S (Figure 11) yielded similar ranges of $\Sigma NPP_{b_{bp}}$ and $\Sigma NPP_{\Delta O_2}$ from 7.1–12.5 and 6.6–12.0 mol C m^{-2} y^{-1}, respectively. The NPP estimates are reasonably close to those made by ^{14}C incubations (see Supplementary Information; Figure B**2**). The total $NPP_{b_{bp}}$ and $NPP_{\Delta O_2}$ in the 30–70°S region was quantified as 11.4 ± 1.1 and 11.7 ± 5.6 Pg C y^{-1}, and in the region 50–70°S, as 4.6 ± 0.8 and 3.5 ± 5.6 Pg C y^{-1}, respectively (Table 2). The parameters used to define which floats are sampling at roughly equal hours of the day shows that these NPP estimates vary with different parameters but average to ~11.5 Pg C y^{-1} and ~4 Pg C y^{-1}, respectively (Table B1). I analyzed NPP derived from co-located b_{bp} and O_2 to determine if real differences exist between $NPP_{b_{bp}}$ and $NPP_{\Delta O_2}$. Although volumetric NPP still had differences at each latitude (Figure B3), I obtained similar zonally-resolved NPP using this subset (Table B2). When pooled into a single diel cycle, the two NPP estimates appeared to follow an almost 1:1 relationship (slope = 1.07; $R^2 = 0.78$; $p < 0.05$; Figure B**4**).

Table 2. Total NPP south of 30°S. The area is calculated from ETOPO5 using all grid cells deeper than 2,000 m. The climatological mean euphotic depth was obtained from NASA Ocean Color and was rounded to the nearest depth bin's center. Both Argo float and satellite data are from 2010 to 2020 (inclusive) and do not include data points in waters less than 2,000 m deep. Total NPP below 30°S and 50°S is calculated as the sum of all latitudinal bands shown in the table. Errors represents one standard error.

Latitudinal Band	b_{bp} - Profiles	O_2- Profiles	Area (10^{13} m^2)	z_{eu} (m)	$NPP_{b_{bp}}$ (Pg C y^{-1})	$NPP_{\Delta O_2}$ (Pg C y^{-1})	NPP_{VGPM} (Pg C y^{-1})	NPP_{CbPM} (Pg C y^{-1})	NPP_{CAFE} (Pg C y^{-1})
30–40°S	2,386	3,617	2.94	95	4.4 ± 0.4	4.1 ± 0.4	4.5	4.5	4.7
40–50°S	4,264	8,476	2.80	65	2.4 ± 0.7	4.0 ± 0.6	4.1	3.5	4.5
50–60°S	4,383	8,234	2.37	65	2.8 ± 0.6	1.9 ± 0.3	1.7	1.4	3.0
60–70°S	4,019	6,284	1.53	65	1.9 ± 0.5	1.7 ± 5.6	0.9	1.1	2.0
Total (below 30°S)	15,052	26,611	9.64	-	11.4 ± 1.1	11.7 ± 5.6	11.1	10.5	14.2
Total (below 50°S)	8,402	14,518	3.90	-	4.6 ± 0.8	3.5 ± 5.6	2.6	2.5	5.0

Satellite studies of the Southern Ocean (below 50°S) from the past two decades reported relatively low NPP at 1.9 (Arrigo et al., 2008), 2.9 (Moore and Abbott, 2000), and 1.8–3.4 Pg C y^{-1} (Arteaga et al., 2018). Our results suggest that recent estimates of Southern Ocean NPP may be underestimates and that NPP in this region is more likely above 3 Pg C y^{-1} for the 2010–2020 period. The two studies that estimated NPP for the region south of 30°S are higher than our estimates by 2–5 Pg C y^{-1} (Moore and Abbott, 2000; Arteaga et al., 2018). For south of 30°S, satellite NPP range from 10.5–14.2 Pg C y^{-1}, while south of 50°S, they range from 2.5 to 5.0 Pg y^{-1} (Table 2). In both cases, float-based NPP values are within range of the satellite estimates. The VGPM model compares best to $NPP_{\Delta O_2}$ and $NPP_{b_{bp}}$ for south of 30°S. For south of 50°S, the VGPM model is closest to $NPP_{\Delta O_2}$ while the CAFE model is closest to $NPP_{b_{bp}}$.

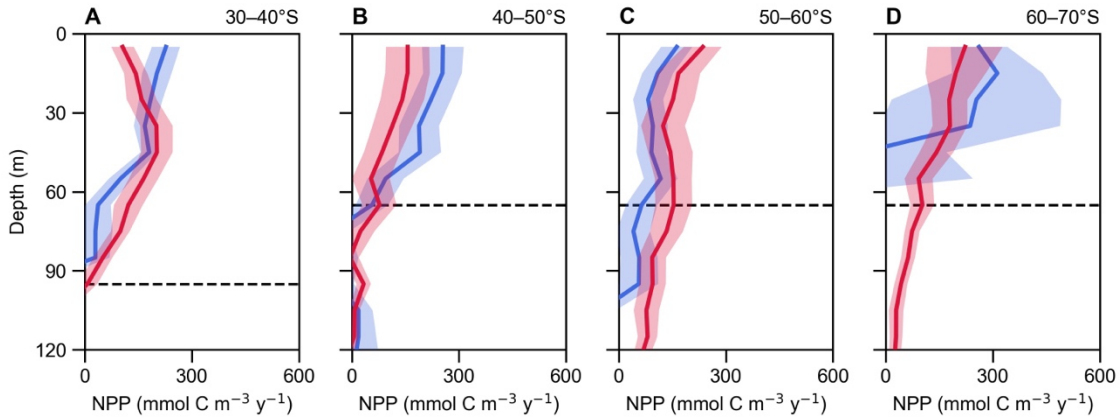

Figure 11. (**A**–**D**) Annual float-based $NPP_{b_{bp}}$ and $NPP_{\Delta O_2}$ estimates at 10-m resolution are shown for each latitude band as red and blue lines, respectively. The shaded regions represent one standard error. The 1% euphotic depth is shown as a dashed horizontal line in each panel.

$NPP_{b_{bp}}$ and $NPP_{\Delta O_2}$ display a strong seasonality (Figure 12). In spring, $\Sigma NPP_{b_{bp}}$ and $\Sigma NPP_{\Delta O_2}$ was 17.6 ± 7.7 and 16.0 ± 1.5 mol C m^{-2} y^{-1}; in summer, $\Sigma NPP_{b_{bp}}$ and $\Sigma NPP_{\Delta O_2}$ was 12.9 ± 14.9 and 21.4 ± 10.7 mol C m^{-2} y^{-1}; in the fall, ΣNPP declined to 2.2 ± 1.0 and 2.1 ± 1.1 mol C m^{-2} y^{-1}; and in the winter to 2.9 ± 0.5 and 1.8 ± 2.1 mol C m^{-2} y^{-1}, respectively. I did not obtain reliable seasonal NPP estimates from 50–70°S potentially because too few profiles were available.

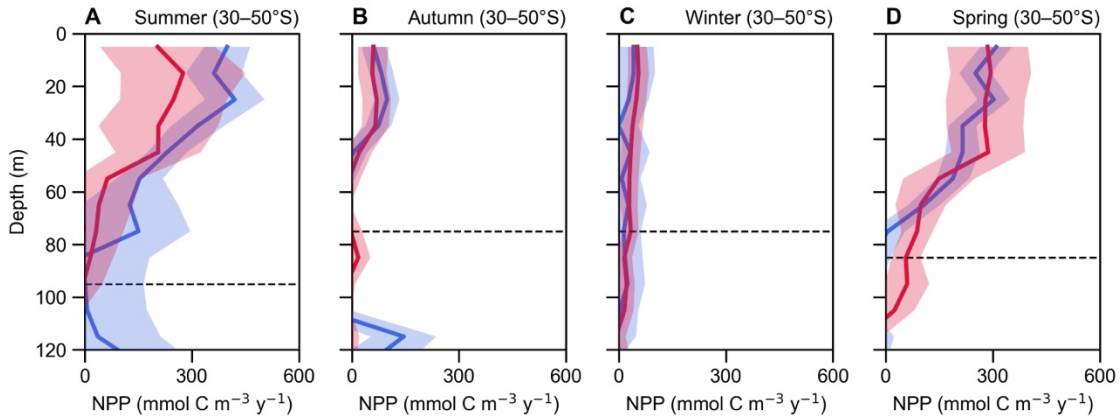

Figure 12. (**A**–**D**) Seasonal float-based $NPP_{b_{bp}}$ (red lines) and $NPP_{\Delta O_2}$ (blue lines) at a 10-m resolution between 30°S and 50°S. The colored shaded regions represent one standard error for float-based NPP. The 1% euphotic depth is shown as a dashed horizontal line in each panel.

Using the co-located dataset, I estimated how many profiles are needed to obtain reliable NPP estimates from diel cycles in this region. The bootstrapping analysis suggests that at least ~2,000 b_{bp}-profiles and ~5,000 O_2-profiles are needed to achieve a noise-to-signal ratio equal to one (Figure B5). This threshold would therefore be achieved annually with ~55 or ~137 active floats measuring b_{bp} or O_2, respectively, at ~10-day intervals.

Our b_{bp}-based approach for estimating NPP has advantages over the O_2-based approach. Namely, $NPP_{b_{bp}}$ is not affected by the same errors that physical processes introduce for $NPP_{\Delta O_2}$ (e.g., air-sea gas exchange; Barone et al., 2019). Bio-optical sensors are also less prone to drift. The use of b_{bp} to estimate NPP is promising because the diel cycle in b_{bp} is retrievable from geostationary satellites. Disadvantages to using b_{bp} include the uncertainty in PER and converting b_{bp} to POC (e.g., spectral slope and b_{bp} -to-POC conversion factors, especially on sub-daily time scales; Poulin et al., 2018). Different conversion algorithms tested in the sensitivity analysis highlight this

uncertainty in $NPP_{b_{bp}}$: estimates range from 5.3 to 20.4 Pg y^{-1} for south of 30°S and 2.2 to 8.2 Pg y^{-1} for south of 50°S (Table B1). Although, an evaluation of these conversion algorithms to determine which is the best performing remains to be done. Biases in the productivity estimates can also arise from day-night shifts in biomass losses (e.g., grazing, particle export, lysis), the uncertainty in the z_{eu} (Table B1), the assumption that GPP is equal to CR, and spatial/seasonal biases in each hourly median. These spatial/seasonal biases are partly controlled by the unique hours parameter, which in our dataset appears to increase $NPP_{\Delta O_2}$ with an increase in the number of unique hours (but leaves $NPP_{b_{bp}}$ unaffected; see Table B1).

Unlike satellites, floats can detect subsurface productivity, including beneath sea ice and community metabolism during the polar night. Although it cannot provide the daily, kilometer-scale resolution of satellite imagery, float-based NPP offers the depth-resolved information needed to ground-truth and calibrate satellite models. In the coming decades, the combination of a sustained float array and space-based remote sensing will provide powerful monitoring capabilities for detecting climate-induced changes in NPP not possible with other current approaches.

Chapter 4

GLOBAL STOCK, PHENOLOGY, AND BIOGEOGRAPHY OF PHYTOPLANKTON CARBON AND CHLOROPHYLL-A‡

4.1 Introduction

Assessing global phytoplankton stocks is an important effort in biology. Modeling suggests that phytoplankton are responsible for about half of the net primary productivity on Earth, rivaling that of the terrestrial biosphere (Field et al., 1998; Johnson and Bif, 2021). And, through the sinking of their organic matter into the deep ocean, phytoplankton keep atmospheric CO_2 concentrations ~200 ppm below an otherwise phytoplankton-free ocean (Falkowski et al., 2000; Parekh et al., 2006).

The most ecologically relevant metric for determining phytoplankton stocks is organic carbon biomass, or C_{org} (Cullen, 1982; Falkowski, 1994), which makes up ~50% of a cell's biomass (Ho et al., 2003). Currently, the global stock of phytoplankton C_{org} is poorly constrained, ranging from approximately 250 to 2,400 Tg C_{org} (Falkowski and

‡This chapter and Appendix C are based on a manuscript in preparation for journal submission.

Raven, 1997; Buitenhuis et al., 2013). This uncertainty limits our ability to establish a confident baseline in global phytoplankton biomass.

Directly measuring phytoplankton C_{org} is notoriously difficult due to the presence of various other particles (e.g., detritus, heterotrophic bacteria, and zooplankton) in seawater among phytoplankton (Banse, 1977; Graff et al., 2012). Typically, phytoplankton C_{org} is estimated indirectly by counting the abundance of phytoplankton cells through flow cytometry and then applying conversion factors regarding their carbon content. In addition to this uncertainty, the high cost and time requirements of this approach often make it impractical for collecting consistent shipboard measurements across the ocean.

It is common in biological oceanography to infer C_{org} biomass from the concentration of Chla. This photosynthetic pigment is specific to phytoplankton and can be measured with ease and high sensitivity (Holm-Hansen et al., 1965; Cullen, 1982; Falkowski, 1994) but makes up only ~1% of the cell's biomass (Cullen, 1982). The Chla pigment has a distinct optical signature, strongly absorbing colors in the blue (~420 nm) and red (~660 nm) parts of the light spectrum. In most of the ocean, phytoplankton Chla correlates with the optical properties of seawater to such an extent that it can estimated from space.

Beginning in the late 1970s with the Coastal Zone Color Scanner (Gordon et al., 1983), satellite observations of the ocean's color revolutionized our view of ocean biology with global maps of Chla (McClain, 2009). More modern satellite instruments like the Sea-viewing Wide Field-of-View Sensor (SeaWiFS) and the Moderate Resolution Imaging Spectroradiometer (MODIS) have provided daily, kilometer-scale images of Chla. Surface Chla estimates based on satellite ocean colour technology has

enabled fundamental studies about the standing stocks of phytoplankton, including their geographic and seasonal variations (Yoder et al., 1993; Siegel et al., 2002; Platt et al., 2003; Platt and Sathyendranath, 2008; Racault et al., 2012) and their response to weather and climate (Yoder and Kennelly, 2003; Babin et al., 2004; Behrenfeld et al., 2006; Martinez et al., 2009; Henson et al., 2018; Thomalla et al., 2023).

However, there are important, well-known limitations to describing large-scale phytoplankton dynamics with satellite-detected Chla. For one, it has long been recognized that the relationship between Chla and C_{org} is highly variable (Riley et al., 1949; Steele, 1964; Eppley et al., 1971; Banse, 1977; Cullen, 1982, 2015). A wide range of C_{org}-to-Chla ratios has been reported, generally from 10 to 300 mg C_{org} mg $Chla^{-1}$, across studies using laboratory cultures (Geider, 1987; Cloern et al., 1995), field samples (Riley et al., 1949; Graff et al., 2015), robotic profilers (Thomalla et al., 2017; Xing et al., 2021; Chiswell et al., 2022), and satellites (Behrenfeld et al., 2005; Sathyendranath et al., 2009; Jackson et al., 2017). The C_{org}-to-Chla ratio of the phytoplankton is influenced by factors like taxonomic composition and growing conditions (e.g., temperature, nutrients, and light) in systematic but complex ways (Cullen, 1982; Geider et al., 1997). The adjustments phytoplankton make to their intracellular Chla content in response to ambient light levels (called photoacclimation) is a major determinant in the distribution of Chla in the ocean (Fennel and Boss, 2003; Alvarez-Fernandez and Riegman, 2014; Behrenfeld et al., 2016; Masuda et al., 2021). Among all other factors, photoacclimation can significantly complicate the interpretation of the temporal trends in C_{org} biomass based on Chla alone (Alvarez-Fernandez and Riegman, 2014; Behrenfeld et al., 2016).

Secondly, ocean color satellites are inherently biased towards a small fraction of the sunlit ocean called the first optical depth (Gordon and McCluney, 1975). Approximately 90% of the reflected light received by satellite ocean colour technology comes from the first optical depth. However, the euphotic depth – the depth at which photosynthesis is no longer appreciable – is conventionally defined at depths about five times greater than what the satellite is sensitive to*. This observational limitation leaves a substantial portion of subsurface phytoplankton unobserved.

Following the advice of Behrenfeld and Boss (2018), evaluating phytoplankton stocks as depth-integrated carbon biomass is needed to properly understand large-scale phytoplankton dynamics. The emerging global network of BGC-Argo floats currently provides carbon stocks estimates of phytoplankton but has not yet been analyzed on a global scale. Floats are a type of profiling robot that freely drift across the ocean, travelling through the entire euphotic zone and up to 2 km depth every 5 or 10 days (Claustre et al., 2020). During their ascent, these floats measure two key bio-optical parameters: Chla fluorescence, a proxy for Chla, and particle backscatter (b_{bp}), a proxy for C_{org} (Martinez-Vicente et al., 2013; Graff et al., 2015). The growing use of this new technology in oceanography has allowed for depth-resolved, carbon-based studies of phytoplankton dynamics (e.g., Boss and Behrenfeld, 2010; Westberry et al., 2016; Arteaga et al., 2020). These studies have highlighted the importance of resolving the

* The euphotic depth is commonly defined as the depth at which photosynthetically available radiation is 1% of its surface value. The 1% euphotic depth is about 4.6 times deeper than the first optical depth, as per Morel (Morel, 1988).

subsurface structure of C_{org} as well as the misleading interpretations that could result from relying solely on Chla concentrations or surface measurements (Chai et al., 2021; He et al., 2023; Vives et al., 2023). There is great value in understanding how a satellite-based Chla view of phytoplankton biomass commonly relied on compares in a global context with the more holistic, carbon-centric view now provided by autonomous profilers.

Here, I aim to address two simple questions: What is the standing stock of phytoplankton Chla (Tg) and C_{org} (Tg) on Earth? And how well does surface Chla characterize the depth-integrated C_{org} (ΣC_{org}) stocks in space and time? I address these questions to better constrain global stocks of phytoplankton C_{org} (and Chla) and to offer a quantitative assessment on the reliability of surface Chla is as a proxy for ΣC_{org}. I used 86,523 high-quality profiles of Chla fluorescence and b_{bp} from 769 floats from the BGC-Argo database (Figure 13). From this dataset, which includes measurements from all ocean basins and seasons, I created weekly, mean climatologies of depth-resolved Chla and C_{org}. These climatologies were then used to calculate the total stocks of annual mean Chla and C_{org} for every 10° latitude band. The weekly resolved climatologies allowed us to compare the seasonal cycle of surface Chla (calculated as the average concentration within the mixed-layer) with the total stock of phytoplankton carbon biomass, ΣC_{org}.

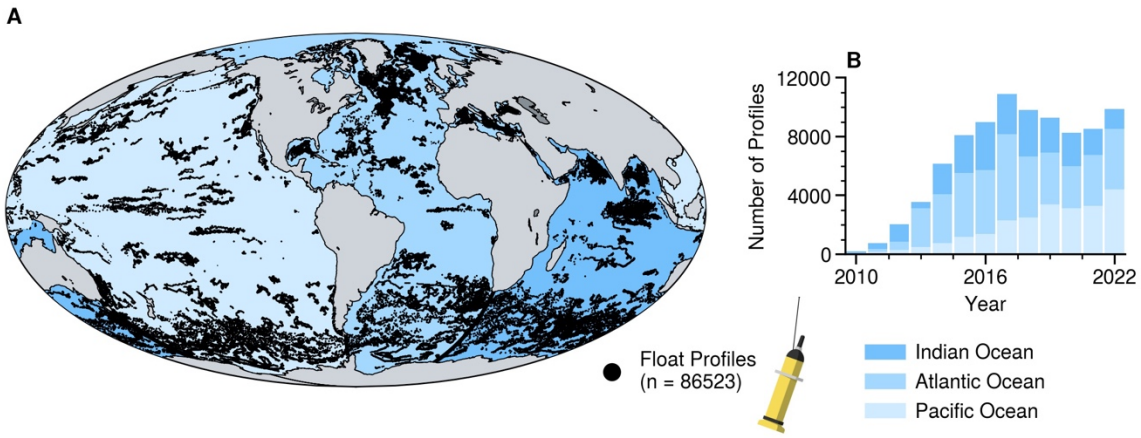

Figure 13. (**A**) Global map of 86,523 quality-controlled, bio-optical profiles from BGC-Argo floats measuring phytoplankton Chla and C_{org} (black points); and (**B**) the number of profiles obtained each year. The geographical boundaries of the Pacific, Atlantic, and Indian ocean basins (colored regions) are used to calculate the climatological means every 10° latitude of surface Chla and ΣC_{org}.

4.2 Methodology

4.2.1 Sources of biogeochemical float data.

Four sources of BGC-Argo float data were used. The first source is the BGC-Argo Program database (Argo, 2023). I downloaded the float data between March 16–17, 2023. At the time, there were 853 floats with bio-optical sensors. Second, I added 10 additional floats deployed in the Gulf of Mexico with funding from the Gulf of Mexico Research Initiative (Shay et al., 2018; Gordon et al., 2020) using the data processing provided by Gordon et al. (Gordon et al., 2020). Third, I included data from 7 floats deployed earlier in the Gulf of Mexico from the National Oceanographic Data Center (NODC) (Hamilton and Leidos, 2017). The fourth source included data from 13 floats deployed in the Northwest Atlantic for the North Atlantic Aerosol and Marine Ecosystem Study (NAAMES) campaign (Behrenfeld et al., 2019;

https://misclab.umeoce.maine.edu/floats/). I cross-referenced these floats with the BGC-Argo program database and found no duplicated float data.

4.2.2 Quality control and processing for biogeochemical data.

Not all data sources include quality-control flags for conductivity-temperature-depth (CTD) and bio-optical data. The BGC-Argo Program and Gordon et al. (2020) provided QC flags for the CTD data. For the BGC-Argo Program database, I only used data with the QC flags of 1,2, 5, and 8 and adjusted and delayed-mode data (Argo Data Management Team, 2022), which are considered science-quality measurements. For Gordon et al. (2020), the same selection criteria for QC flags were applied (i.e., flags 1,2, 5, and 8). The NODC and NAAMES floats did not have QC flags associated with CTD data and therefore underwent a visual inspection only. The bio-optical float sensors underwent a series of tests and corrections to account for potential instances of bio-fouling, malfunction, calibration errors, and other uncommon issues. For this analysis, I developed a standard algorithm that applies a series of tests and corrections to the bio-optical data, which I describe in more detail below.

The quality control of the BGC-Argo float profiles proceeded as follows. After the available QC flags for the CTD data were applied, any BGC data points that did not contain co-located Chla, b_{bp}, temperature, and salinity measurements were discarded. This step was to ensure that all bio-optical measurements had associated CTD measurements. Then each profile underwent a data gap test to ensure that no profile contained any significant gaps in the upper 300 m where phytoplankton are present and variation in oceanographic parameters is relatively high. The gap test discarded any

profiles where there were missing data for more than 100 m within the upper 300 m of the profile.

I then applied a depth range test, which ensured that data were available both between 0 and 15 m depth and deeper than 300 m depth. The only exception to the depth range test was if the float was avoiding ice. The ice-avoidance software stops floats from ascending before reaching the surface and potentially colliding with sea ice. The settings for the ice-avoidance software varies between floats and sampling programs. For example, the ice avoidance algorithm on Southern Ocean Carbon and Climate Observations and Models (SOCCOM) program floats is triggered if the median temperature between 20 and 50 m is less than -1.78°C (Riser et al., 2018). Alternatively, the ProIce floats (see Randelhoff et al. 2020) used an ice-avoidance algorithm with a threshold of -1.3°C in addition to an ice-detecting sensor and a simple date criterion to avoid ascent. Because of the differing sea ice avoidance techniques, I decided to use a more generous temperature threshold of -1°C to compare against the median temperature in the upper 50 m of the water-column. If the median temperature observed by the float was below this threshold, I assumed the float avoided sea ice and accepted float profiles that instead reached a minimum of 25 m depth (rather than 15 m) for the depth range test.

If a float profile passed the gap test and the depth range test, the mixed-layer depth (MLD) was calculated. The MLD is commonly-defined as the depth where the density has increased by a set threshold compared to the density at reference depth near the surface (e.g., de Boyer Montégut et al., 2004). A variety of threshold potential densities (0.005 to 0.125 kg m^{-3}) and reference depths (0 to 20 m) have been used to define the MLD before (de Boyer Montégut et al., 2004; Dong et al., 2008; Holte et al., 2017). For

our MLD calculation, I decided to use a threshold density of 0.03 kg m^{-3} and reference depth of 15 m. If a float had not ascended to at least 15 m and was determined to be avoiding sea ice, the reference depth was set to the minimum depth in the profile (25 m or less). This reference depth is chosen to avoid diurnal mixed layers (de Boyer Montégut et al., 2004) and because there is occasionally a lack of CTD data at shallower depths, as done previously in the literature (Dong et al., 2008). In the rare case where the density threshold was not exceeded (e.g., MLDs of 2000 m can occur in the Nordic Seas; 11), the MLD was set to the maximum depth of the profile.

The bio-optical measurements of b_{bp} and Chla fluorescence were then quality controlled following a similar procedure as Dall'Olmo et al. (2023).

For b_{bp}, a gross filter test was first applied. A profile failed the gross filter test if more than 10% of the b_{bp} data in the profile were less than 0 m^{-1} or greater than 0.03 m^{-1}. I then applied a profile hook test. Profile hooks occur when unusually high b_{bp} is present at the start a float's ascent. This high b_{bp} is believed result from particles that either stick to the sensor face or rest on the top of the float while the float is resting for several days between profiles (Dall'Olmo et al., 2023). If the float is set to rest at the same depth at which it begins recording data, then it is common to observe high b_{bp} values that quickly decrease to a background value as the float ascends (hence the name "profile hook"). I only applied this test to floats from the BGC-Argo program since the parking depth information was available with the associated metadata. If the parking depth was known, then the profile hook test was only applied if the parking depth was within the 20 m of the deepest b_{bp} measurement. If this was the case, any data points greater than a set threshold value within those 20 m were discarded. This threshold value was calculated as

the median b_{bp} of the bottom 100 m of the profile plus 0.0001 m^{-1}. After the parking hook test, I applied a spike/noise test similar to Dall'Olmo et al (2023). This test was only applied to profiles deeper than 300 m, as shallower parts of the profile can have a larger frequency of spikes that arise from real biogeochemical phenomena (e.g., bubbles, aggregates, zooplankton).

For the spike/noise test, the difference in b_{bp} was calculated from b_{bp} in the original profile and the profile of b_{bp} smoothed with 7-point median filter. A data point was labelled a spike when the absolute difference was greater than 0.0005 m^{-1}. If more than 10% of the b_{bp} data in the profile contained spikes, than the whole profile was considered too noisy/spikey and was discarded. If the profile passed the spike/noise test, any spikes greater than 0.0005 m^{-1} or less than -0.0001 m^{-1} were removed from the profile.

Next, I tested for inaccurate offsets in the calibration, sensor malfunction, and/or bio-fouling, using the deep b_{bp} test. This test is only applied to data deeper than 500 m, where b_{bp} is generally expected to be low (but not equal to 0 m^{-1}) in the open ocean. A profile fails the deep b_{bp} test if more than 20% of the values below 500 m depth are negative, or if the minimum b_{bp} below 500 m depth is higher than 0.0006 m^{-1}. This test biases against profiles taken where sediment resuspension is present in the water column, such as near a shelf break or in shallow waters.

After the deep b_{bp} test, the profile is checked for negative b_{bp} near the surface at depths less than 10 m. These negative values could result from bubbles sticking to the surface of the sensor or the float breaching the surface of the ocean. Once these tests have been applied, the b_{bp} profile is smoothed with 5-point median filter followed by a 7-point mean filter.

The profiles of Chla underwent a series of rigorous tests and corrections as well. The first test was a gross filter test. It removed profiles when more than 10% of the data points in the profile contained values outside of the range from -0.5 to 20 mg m^{-3}.

I then applied a sensor response test, which determines whether the Chla sensor simply outputs the same value or an unrealistically small range of values throughout the water column, likely resulting from sensor malfunction. The sensor response test calculates the ratio of the difference between the 90^{th} and 10^{th} percentiles of Chla in the upper 200 m to the difference between 90^{th} and 10^{th} percentile of Chla below 300 m. This ratio is meant to compare the variability near the surface (where gradients in Chla are present) with the general lack of variability at depth (where Chla should be close to 0 mg m^{-3}). The sensor response test is failed when two conditions are met. The first condition is that the surface-to-deep ratio in Chla is less than 1.1. A ratio of less than 1.1 suggests that the range in Chla at depth is similar to that at the surface, meaning the sensor is insensitive to changes in Chla or is stuck on the same value. The second condition is met when the median concentration of Chla in the upper 100 m is below 0.05 mg m^{-3}.

After the sensor response test, I applied a spike/noise test similar to the one applied to profiles of b_{bp}. This test is applied only to profiles deeper than 300 m and calculates the absolute difference between the original Chla values and the seven-point median filtered version of the Chla profile. If more than 10% of the profile contained spikes greater than 0.1 mg m^{-3}, the profile failed the spike/noise test and was discarded. If the profile passed this test, the spikes that exceeded the threshold were removed from the profile.

Next, a standard dark offset correction was applied to the Chla profile. The dark offset corrects for errors in the Chla calibration associated with varying photo-chemical

conditions among each profile. The dark offset is determined in situ as the minimum Chla value found in the deep portion of the water column where Chla is expected to approach 0 mg m^{-3}. A dynamic depth range was used to search for an accurate minimum value. The lower limit of the depth range was either the mixed-layer depth and the depth of the deep chlorophyll maximum, whichever was deeper. The upper limit of the depth range was the deepest value of the profile. The deep chlorophyll maximum is calculated as the depth of maximum Chla concentration from a Chla profile smoothed with a 5-point median filter followed by a 7-point mean filter. The dark offset was set as minimum Chla concentration within the specified depth range from a 7-point median filtered version of the Chla profile. The dark value was then subtracted from the Chla profile, such that the depth of the dark offset equaled 0 mg m^{-3}. Occasionally, a small increase in Chla fluorescence is observed with increasing depth below the euphotic zone as a result of fluorescent dissolved organic matter. Since I expect Chla to be equal or near 0 mg m^{-3} at high depths, all values below the dark offset value were set to 0 mg m^{-3} to eliminate this fluorescence bias at depth. In cases where the mixed layer depth was set to the bottom of the profile (e.g., during deep mixing events), the profile was only offset with the last known dark offset values determined from a previous profile, which typically does not vary greatly from profile to profile.

Using the dark offset, I employed a biofouling/malfunction test which eliminated profiles when the absolute value of the dark offset was greater than 0.1 mg m^{-3}. Following these tests, negative values of Chla were removed between 0 and 10 m depth, if present.

The Chla profile was then smoothed with a 5-point median filter followed by a 7-point mean filter. With the smoothed profile, I corrected for the effects of non-photochemical quenching (NPQ) on Chla fluorescence following a similar protocol to Xing et al. (2012), which is also used for quality control within the BGC-Argo program (Schmechtig et al., 2018). To correct for NPQ, the maximum Chla value within the mixed layer was found. Then, all values above the depth of mixed-layer maximum Chla were set to the maximum of Chla in the mixed-layer. The NPQ correction was only applied to profiles that were made between sunrise and sunset, or during polar day (when the sun is continuously present throughout the day).

A final correction was made based on the biases identified by Roesler et al. (2017). Using their Table 2, I calculated the median slope factor for the estimates north of 30°S (equal to 1.80) and south of 30°S (equal to 4.13). These correction factors were applied to the individual quality-controlled Chla profiles in each region. This correction was made to reduce global biases in Chla resulting from the manufacturer's calibration of Chla sensor. Since this correction is only applicable to Wetlabs ECO sensors, I checked to ensure all floats in our database were equipped with this type of sensor.

Following the quality control of the Chla and b_{bp} data, the profile was binned to a 5-m resolution and the average value in each bin was recorded. If either Chla or b_{bp} had failed any of their tests, the entire profile was discarded. This was done for two reasons. The first reason was that Chla and b_{bp} are measured from the same device within a few centimeters of each other. So, if there were any issues present in either measurement (e.g., bio-fouling on the sensor head was identified in b_{bp} but not Chla), I assumed that none of the data from the device was accurate. Secondly, I wanted to ensure all

comparisons with float data made in this study used co-located measurements of Chla and b_{bp}, to avoid any potential bias due to differences in temporal or spatial coverage.

The profile then underwent the same 100-m gap test employed before to ensure the previous filters did not remove a substantial portion of profile. If there were no significant gaps, data in the profile was interpolated. Additionally, data from the shallowest depth of the profile was extrapolated to the surface if needed, under the assumption that the mixed layer is well-mixed.

As a final precautionary step, I employed a test called the long-term failure test. For the long-term failure test, I recorded the profile number of all b_{bp} or Chla profiles that failed the gross filter test, spike/noise test, deep b_{bp} test, sensor response test, or biofouled/malfunction test. If the Chla or b_{bp} profile failed any of these tests at least five-times in a row, then I removed all profiles collected after this series of failures. I also removed any profiles collected 100 days prior to when these consecutive failed tests first started. This latter step was taken as a cautionary measure to avoid any inaccurate data resulting from onset of bio-fouling, sensor drift, or sensor malfunction that could not be easily identified by previous tests.

Finally, each float transect was visually inspected to check for issues not flagged by the QC tests. This step is similar to the grey list employed by Argo (Argo Data Management Team, 2022). If a float contained data with inconsistent environmental data, I decided to either remove all the data from the float or only data from a specified period. If some of the float data was retained, I chose a date well before the apparent issue was evident (e.g., a sudden increase in the bio-optical values). In total, data from only 8 floats were removed (Table C1).

Prior to applying these QC tests, I had 883 floats with bio-optical sensors across all data sources. Out of these floats, 791 floats passed QC and were used in this analysis resulting in 86,523 profiles for analysis.

4.2.3 Calculation of phytoplankton carbon

To determine phytoplankton C_{org}, b_{bp} must be partitioned into phytoplankton ($b_{bp,phyto}$) and non-algal particle ($b_{bp,NAP}$) components, such that:

$$b_{bp} = b_{bp,phyto} + b_{bp,NAP}, \quad 10$$

Often, C_{org} is calculated by assuming a constant $b_{bp,NAP}$ (e.g., Behrenfeld et al., 2005; Martinez-Vicente et al., 2013; Graff et al., 2015), however, $b_{bp,NAP}$ can vary with depth, season, and region (Bellacicco et al., 2019). If $b_{bp,NAP}$ variability is not considered, the conversion of b_{bp} to C_{org} can lead to erroneous results (e.g., negative C_{org} concentrations).

To account for the spatiotemporal variability of $b_{bp,NAP}$, I calculated $b_{bp,NAP}$ as a "background" value of b_{bp} for each weekly mean profile. This approach builds off the offset correction from Arteaga et al. (2020). They offset surface C_{org} with reference values between 900 and 2000 m depth to ensure C_{org} asymptotes to 0 mg m^{-3} with depth. I calculated $b_{bp,NAP}$ by utilizing all values of b_{bp} at depth. I first restricted measurements of b_{bp} to the deeper portion of the profile, where Chla concentrations are close to zero and b_{bp} is dominated by NAP. I separated NAP-dominated b_{bp} as all b_{bp} values less than the profile's median b_{bp}, and then applied a 1% quantile regression to the depth profile of separated b_{bp}. Using this trend line, I defined a depth horizon equal to the shallowest depth where the b_{bp} profile intersects with the line. Below this depth horizon, $b_{bp,NAP}$ is set equal to b_{bp}, where b_{bp} is largely NAP-dominated. Above this depth horizon, $b_{bp,NAP}$ is set equal to b_{bp} at the point where the trend line intersects with the profile (extrapolating

the background value towards the surface). The resulting profile of $b_{bp,NAP}$ is then used to estimate $b_{bp,phyto}$ by subtraction. Phytoplankton C_{org} was calculated as the product of an empirically-derived slope coefficient based on direct estimates of C_{org} (Graff et al., 2012, 2015):

$$C_{\mathrm{org}} = 12128 \times b_{\mathrm{bp,phyto}}, \quad 11$$

4.2.4 Calculation of weekly climatology and global stock

Profiles were grouped every 10° latitude for each ocean basin (Atlantic, Indian, and Pacific) between 80°S and 90°N. For all calculations below, measurements were limited to the upper 500 m of the ocean. For each region, the weekly average mixed-layer depth and depth profiles of temperature, salinity, Chla, and b_{bp} were calculated from the available profiles. Weeks with missing data were interpolated with the closest available data. Then, C_{org} was calculated from the weekly averaged b_{bp} profiles (see Section 4.2.3)

The weekly, depth-resolved climatology was concatenated three times, and a nine-point running median followed by a nine-point running mean was applied to the weekly mixed-layer depth and each isoline of C_{org} and Chla. The center 52-week smoothed time series was then separated and used for the analysis. For regions with no available data in the Arctic or with little ocean area, I extrapolated the entire seasonal cycle from the closest available region. This step only constituted ~0.2% of the final global estimates of C_{org} and Chla. The stock of Chla (Tg) and C_{org} (Tg) for 5 m intervals was calculated as the product of the total volume of seawater (m^3) at each depth (Figure C1) and its average, weekly volumetric concentration (mg of Chla or C_{org} m^{-3}). At this point, these steps have resulted in a smoothed weekly climatology of depth-resolved stocks of Chla and C_{org} every 10° latitude for the Indian, Pacific, and Atlantic oceans. The sum of these

weekly stocks was calculated to obtain a weekly and annual mean global stock. For phenological analysis, the weekly mean depth-integrated stock of Chla and C_{org} underwent an additional smoothing using a six-point rolling median followed by a six-point rolling mean.

4.2.5 Conversion factors and uncertainty in global stocks

I quantified the error in both our global C_{org} and Chla estimates from floats. For this, I considered only the uncertainty in the conversion of the bio-optical parameter to biological mass, and assume that errors due to sensor drift, temperature, bio-fouling, and intra-model sensor calibrations are negligible. I report 95% confidence intervals (CI) for all C_{org} and Chla using the standard error multiplied by 1.96.

The factors and their uncertainty for converting b_{bp} to C_{org} was determined from a linear least-squares regression applied to the measurements made by Graff et al. (2015). These measurements are based on direct measurements of phytoplankton carbon biomass, which resulted in a slope and intercept of 12,128 mg m^{-2} + 0.59 mg m^{-3}. While these conversion factors are very close to the approximation made by Behrenfeld et al. (2005), the direct measurements by Graff et al. have not yet been replicated.

The error in the conversion factors is not reported in Graff et al., so to determine this error, the data from their Figure 3 was digitized using WebPlotDigitizer (https://automeris.io/WebPlotDigitizer/). I counted 52 data points and calculated the same slope and y-intercept reported in their study. The slope and its standard error of the regression were calculated as 12,128 ± 1168 mg C_{org} m^{-2}, which is equal to a 95% CI in the slope of 9,839–14,417 mg C_{org} m^{-2}. The uncertainty in Chla was evaluated from the unitless slope factors provided by Roesler et al. (2017) from their Table 2. For non-

Southern Ocean regions, I calculated a median slope factor and standard error of 1.8 ± 0.06 (or a 95% CI of 1.7–1.9). For Southern Ocean regions, I calculated a slope factor and standard error of 4.13 ± 0.55 (or a 95% CI of 3.5–4.7). Through error propagation, the global error in the estimate of Chla was determined from the sum of Southern Ocean (2.3 ± 0.3 Tg) and non-Southern Ocean (6.8 ± 0.4 Tg) Chla stocks. For the final global stock, I determined the annual mean ± 95% CI of global C_{org} and Chla stocks equal to 341 ± 65 Tg and 9.1 ± 0.5 Tg, respectively.

4.2.6 Satellite chlorophyll-a climatology

To compare with float observations of surface Chla and ΣC_{org}, I created weekly climatologies of surface Chla using level-3 data from the MODIS-Aqua satellite. I obtained 8-day surface Chla data with a 9-km spatial resolution for the period of January 1, 2012, to December 31, 2022. This date range approximately covers the period when most of the float data was collected (Figure 13). For each image, I calculated the average Chla concentration for every 10° latitude only if 70% of pixels were available. These weekly averages were used to calculate a mean climatology for each latitudinal band to compare with float observations. Similar to the float climatology, satellite Chla was concatenated three times and smoothed with a three-point rolling median followed by a three-point rolling mean, using the center 52-weeks of data for analysis.

4.2.7 Phenological metrics

A variety of metrics to describe phytoplankton blooms and the seasonal cycle of phytoplankton biomass have been used before (Platt and Sathyendranath, 2008; Behrenfeld, 2010; Boyce et al., 2017). Here, I characterized the annual cycle of phytoplankton with three phenological metrics: 1) the timing of the bloom peak, 2) the

bloom duration, and 3) the bloom amplitude. These metrics were calculated using ΣC_{org} and surface Chla (as a proxy for ΣC_{org}). The timing of the peak bloom is the week when ΣC_{org} or surface Chla is at its maximum. Bloom duration was defined as the number of weeks when ΣC_{org} or surface Chla are above the annual average (*sensu* Boyce et al., 2017). To give a sense of the relative variation in each region's seasonal cycle, the bloom amplitude was defined as the maximum in ΣC_{org} or Chla minus the minimum and divided by the annual mean (*sensu* Cloern and Jassby, 2008). Similar metrics were also calculated for satellite Chla to compare with surface Chla. Pearson correlation coefficients were determined for the log-transformed surface Chla v. ΣC_{org} and surface Chla v. satellite Chla (Figure C**4**). These correlations, bloom amplitude, and bloom duration were calculated only when at least 47 weeks of year had available satellite data. Additional metrics describing the seasonal cycle, such as the timing of the minimum rate of change, are also reported in Appendix C (Figure C5). Latitudinal trends in phenological metrics are described with generalized additive models using LinearGAM function from the pyGAM Python package.

4.3 Results and Discussion

I calculate total standing stocks of ~341 Tg C_{org} and ~9.1 Tg Chla in the global ocean (Figure 14). Area-normalized stocks are equal to ~952 mg C_{org} m^{-2} and 25 mg Chla m^{-2}, respectively. This puts the global average C_{org}:Chla ratio at ~38:1. The majority of the C_{org} and Chla stocks are present in the southern hemisphere (65% and 55%, respectively). I find both C_{org} and Chla stocks closely follow the relative sizes of each basin: the Pacific Ocean holds half of the global stocks, while the Indian and Atlantic Ocean each hold a quarter. The climatological depth of maximum Chla is offset by more than 10 m from the

depth of maximum C_{org} in ~80% of the ocean (by area). Moreover, the subsurface layer (everything below the surface mixed layer) contains about half of the global C_{org} and Chla stocks (45% and 56%, respectively) meaning that large portions of Earth's phytoplankton are not observable from satellite. Below 300 m, extremely small portions of global C_{org} (~0.3%) and Chla (~0.7%) stock are present, which is consistent with expectations (Buitenhuis et al., 2013).

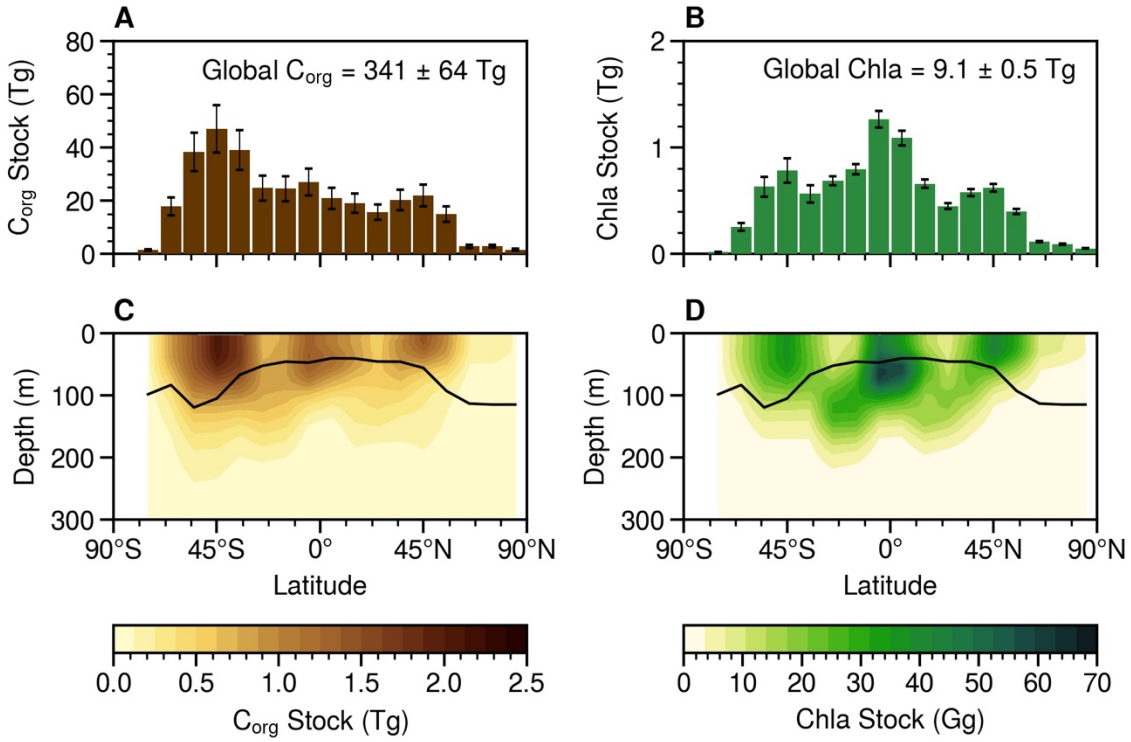

Figure 14. (**A**, **B**) Latitudinal distributions of Chla and C_{org} stock; and (**C**, **D**) vertical distributions of Chla and C_{org} stocks per 5 m depth. The average mixed layer depth, weighted by the area of each ocean basin, is shown as a black line in each **C** and **D**. Note that stocks are integrated from 0 to 500 m, although stocks below 300 m depth are either extremely low or equal to zero.

Differences between the latitudinal distribution in C_{org} and Chla stocks are substantial. Nearly half of Earth's phytoplankton C_{org} stock is present in the Southern Ocean and its subtropical boundaries. I find that around ~42% of C_{org} is located south of 30°S (Figure 14), even though the same region only represents about a third of the

ocean's surface area and holds only a quarter of the global Chla stock. I do not observe any obvious differences in ΣC_{org} between the subtropical gyres and the equatorial upwelling zones, in contrast to ΣChla or surface Chla, which increase near the equator (Figure C2), although this result should be interpreted cautiously due to possible changes in the C_{org}-to-b_{bp} ratio across the equatorial band (Fox et al., 2022). However, I have confidence that phytoplankton south of 30°S make up a major portion of global C_{org} stocks and are likely underestimated there (Fox et al., 2022). Altogether, the biogeography of C_{org} stocks, especially in the Southern Hemisphere, show a qualitatively different pattern compared to that of Chla.

Our estimate of global phytoplankton biomass of 341 Tg is within the lower end of previous estimates, which range from 250 and 2,400 Tg (Falkowski and Raven, 1997; Buitenhuis et al., 2013). I argue that our estimate is more reliable because, unlike previous approaches, it contains depth-resolved, carbon-centric measurements from the entire euphotic layer (and deeper). Previous estimates are based on either satellite-observed ocean color or cell abundance measurements taken in the field. Satellite estimates come from net primary productivity models, which rely on assumptions about the vertical structure of Chla. For example, Antoine et al. (1996) put global C_{org} at 860 Tg, assuming a global C_{org}:Chla ratio of 100 g C_{org} g $Chla^{-1}$, even though their global Chla stock of 8.6 Tg was reasonably close to ours (~9.1 Tg). Falkowski and Raven (1997) estimated global C_{org} somewhere between 250 to 650 Tg (assuming a Chla:C_{org} ratio between 40 and 100 g $Chla^{-1}$ g C_{org}^{-1}). As for abundance-based estimates, they rely on a relatively sparse number of observations and must make assumptions about intracellular carbon concentrations. Abundance-based estimates from Buitenhuis et al.

(2013) put global phytoplankton C_{org} between 500 and 2,400 Tg. A global census for all oceanic life on Earth from Bar-On et al. (2019) provides a best estimate of ~600 Tg of C_{org}. Considering the error in our conversion factors, the 95% confidence interval in our estimate of global phytoplankton C_{org} only ranges from 276 to 407 Tg (see Appendix C). Thus, our more holistic, carbon-based subsurface estimate acts as a constraint that significantly narrows the current range of global phytoplankton estimates and will make it easier to determine any climate-related changes into the future.

These carbon-based, depth-resolved observations also allow us to better characterize the seasonal cycles in phytoplankton C_{org} stock across the global ocean (Figure 15). I find that the annual phytoplankton bloom reaches its peak, on average, 10 weeks after surface Chla has reached its annual maximum across ~75% of the ocean (Figure 15C). Alternatively, in three quarters of the ocean, the time of the peak phytoplankton bloom is offset by more than 4 weeks from the peak in surface Chla. The area where this discrepancy occurs contains ~70% of Earth's phytoplankton carbon stock, and spans equatorial and temperate latitudes. Polar oceans tend to have the best synchrony between surface Chla and ΣC_{org} peaks, however, the difference at latitudes greater than 50° still ranges from 0 to up to 4 weeks.

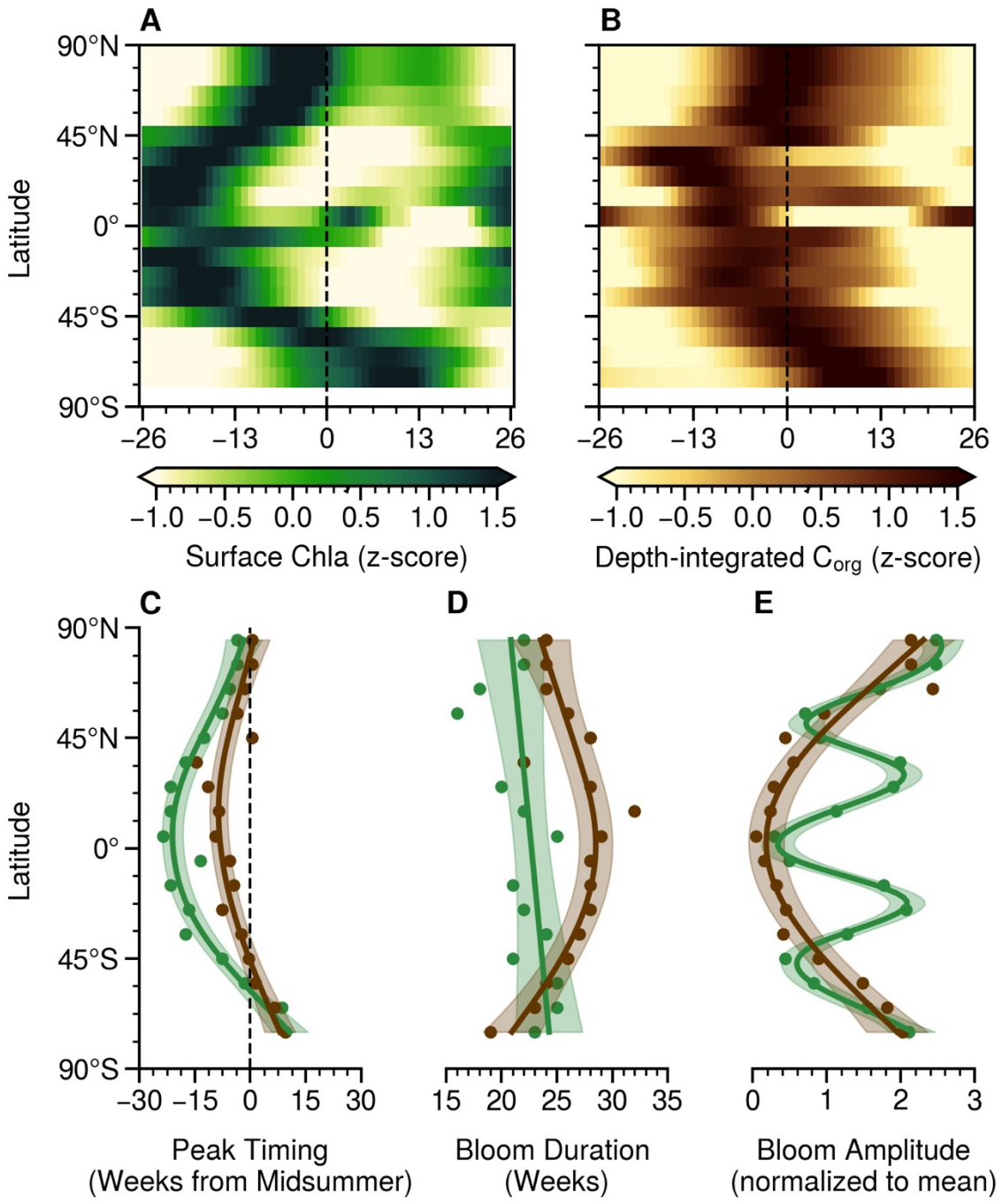

Figure 15. (**A**, **B**) Seasonal cycles in phytoplankton surface Chla (mg m^{-3}) and ΣC_{org} (mg m^{-2}) as z-scores from BGC-Argo floats. (**C**–**E**) Phenological metrics derived from the seasonal ΣC_{org} and surface Chla: (**C**) the timing of the peak ΣC_{org} and surface Chla, defined as the week from the summer solstice (midsummer); (**D**) the bloom duration, defined as the number of weeks above the annual mean; and (**E**) bloom amplitude, defined as the annual range normalized to the mean. The trend lines are best fits estimated from a generalized additive model and the shading represents the 95% confidence interval.

Other aspects of the seasonal cycle in phytoplankton substantially differ from that of surface Chla. The duration of blooms, defined here as the time when ΣC_{org} is above the annual average, tends to follow a parabolic shape that increases towards the equator (Figure 15). If the metric of surface Chla is used in place of ΣC_{org}, the blooms would appear to be 3 weeks shorter, on average, with the difference increasing to ~6 weeks around the tropics (<30°). The seasonal amplitude, measured as the range in ΣC_{org} normalized to the annual average, also follows a parabolic curve but with the amplitude lowest near the equator. The same bloom metric based on surface Chla results in regional maxima around the subtropical oligotrophic gyres and polar oceans not seen in its ΣC_{org} counterpart (Figure 15E). This large variation in surface Chla in the subtropical gyres and polar oceans is not indicative of equally large variation in phytoplankton biomass.

The same latitudinal trends in float-based surface Chla patterns are generally consistent with those from satellite (Figure C3). Furthermore, there is a strong correlation between satellite- and float-based Chla (Figure C4). This indicates that the size of the BGC-Argo array is large enough to describe basin-wide patterns and that the discrepancies between float- and satellite-based estimates of phytoplankton standing stock and phenology are not artifacts of under sampling. The discrepancy between surface Chla and ΣC_{org} exists for other phenological metrics too (Figure C5) and is well exemplified by the fact that the Pearson correlation coefficient between surface Chla and ΣC_{org} is less than 0.5 in 75% of the ocean and less than 0 for ~50% of the ocean (Figure C4). In summary, these carbon-based metrics show that seasonal phytoplankton blooms are longer-lived, less intense, and occur later in the year than implied by surface measurements of Chla.

4.4 Conclusion

Based on our estimate, the biomass of oceanic phytoplankton accounts for only ~0.05% of the biosphere (Bar-On et al., 2018) – a miniscule fraction despite their tremendous role in Earth's ecosystems and carbon cycling. Monitoring of this important group of organisms is necessary given current and projected future increases to ocean temperatures (Cheng et al., 2022), de-oxygenation (Schmidtko et al., 2017; Breitburg et al., 2018), and acidification (Doney et al., 2009). To achieve this, the right measurements of phytoplankton biomass are needed. I have shown that carbon-centric observations from the entire water-column offer a holistic view of phytoplankton biomass that greatly constrains uncertainties in their present stocks. Our estimate is an important benchmark against which to interpret future trends in phytoplankton standing stocks and phenology. I demonstrated how Chla concentrations at the surface are inadequate for describing the dynamics in global phytoplankton biomass. In most of the ocean, surface Chla gives a qualitatively wrong description of the seasonal cycle in phytoplankton biomass for canonical events like the annual bloom. While the depth-limitation of satellites and the variation in C:Chla ratios are well-known, these results demonstrate that surface Chla is more often than not a misleading metric for phytoplankton bloom dynamics. Further studies should focus on re-evaluating our current understanding of phytoplankton dynamics in the context of depth-resolved, carbon-based measurements.

Chapter 5

CONCLUSIONS

This thesis presents results on the quality of measurements from the BGC-Argo program and then applies those measurements to help answer key scientific questions about the ocean's phytoplankton. In Chapter 2, I report a census on the biogeochemical measurement quality of the BGC-Argo program, providing information on the overall, regional, and annual quality of the measurements taken. This chapter provides important context on the biogeochemical measurements used in subsequent chapters (*i.e.*, O_2, Chla fluorescence, and b_{bp}). With a better understanding of the biogeochemical data quality, in Chapter 3, I infer net primary productivity from daily cycles of O_2 and b_{bp} measured by the BGC-Argo fleet. Finally, in another application of the BGC-Argo data, I quantify the stock of phytoplankton C_{org} and Chla on Earth in Chapter 4. I also describe the phenology and biogeography of C_{org} in contrast to Chla at the surface, showing how the two greatly differ despite the common assumption that Chla is a proxy for C_{org} biomass.

5.1 Key Findings and Implications

5.1.1 BGC-Argo array provides high-quality biogeochemical data

Chapter 2 overviews the database of biogeochemical measurements collected by the BGC-Argo program. The program is expanding towards a target of 1,000 floats with

~600 floats deployed so far. As of December 2022, more than 250,000 profiles have been collected by the program. The majority of these profiles contain O_2 measurements, while pH and PAR/E_d are the least abundant. About 110,000 profiles in this database include measurements of Chla fluorescence and b_{bp}. Using the quality flagging system provided by the program, between 80 and 95% of the profiles collected so far contain high-quality BGC data for most BGC parameters, with the exception of pH, which is at ~50%. The yearly portion of high-quality pH profiles has increased from 40 to 60% between 2018 and 2022, putting pH on track to match the data quality of other BGC parameters. This census shows increasing profile numbers and spatial coverage across all marine regions. Currently, some of the highest data density occurs in the seas around Europe (the Baltic, Black, and Mediterranean Seas), the Southern Ocean, and the Arctic Ocean, with the lowest data density in the South Pacific Ocean. However, while data density may be high in some regions, they are not necessarily evenly distributed across the region. I highlight how BGC-Argo is improving and discuss various avenues for how more high-quality profiles could become available. The census presented in this chapter shows that tracking percentages of high-quality data through time is useful for monitoring float sensor technology and the success of the BGC-Argo program.

5.1.2 Novel approach to estimating net primary productivity

With a technique inspired by Johnson and Bif (2021), I show how NPP can be inferred from daily cycles of b_{bp} detected by the BGC-Argo array. In Chapter 3, I estimate NPP equal to ~11.4 Pg C yr^{-1} and ~4.6 Pg C yr^{-1} for the temperate and polar regions of the southern hemisphere. These productivity estimates were comparable when daily cycles of oxygen are used instead (11.7 and 3.5 Pg C yr^{-1}, respectively) and were

within range of satellite-based estimates. The major takeaway from this chapter, which is also exemplified by the work of Gille (2012) and (Johnson and Bif, 2021), is how daily cycles in ocean biogeochemistry can be obtained by the BGC-Argo array – even though the sampling scheme of individual floats is not intended for this purpose. The approach provides information about the subsurface structure of productivity on basin-wide scales, which is otherwise not possible using shipboard- or satellite-based techniques. Daily cycles from the BGC-Argo array could likely be obtained from other variables as well. For example, the variation in nitrate and Chla fluorescence over the course of day has been used to estimate nitrate uptake (Johnson et al., 2006) and non-photochemical quenching (Ryan-Keogh and Thomalla, 2020), respectively. Further studies that focus on expanding this approach to other biogeochemical measurements may offer valuable new insights into ocean biogeochemistry.

5.1.3 A depth-resolved, carbon-centric view of phytoplankton

In Chapter 4, I describe global phytoplankton stocks of C_{org} and Chla using ~90,000 water-column profiles of proxy bio-optical observations. With this dataset, I estimate and constrain global phytoplankton carbon stocks to ~340 Tg. I find that half of Earth's phytoplankton biomass is located below the surface ocean at depths out-of-view from satellites. I show that the seasonal cycle of C_{org} biomass is qualitatively different from Chla at the surface in the vast majority other ocean. This mismatch occurs to such an extent that surface Chla cannot accurately identify the timing of the peak phytoplankton bloom in three-quarters of the ocean. In general, using Chla as a proxy of C_{org} biomass, makes phytoplankton blooms appear too earlier, shorter, and more intense than in reality. These results challenge the decades-long practice of relying solely on satellite

observations of Chla to characterize the dynamics of phytoplankton biomass. In this chapter, I argue, as others have before, that both depth-resolved and carbon-based estimates are needed to properly describe phytoplankton biomass, especially when considering the ongoing and likely future changes to the ocean due to global warming.

5.2 Final Thoughts

To effectively address scientific questions about the ocean, it is essential to gather observations. These observations have largely come from shipboard and laboratory measurements, and for the past 5 decades, from satellite remote sensing. While measurements from water samples are of higher quality, gathering such measurements over decades at basin-wide scales is not feasible. Satellite remote sensing helps alleviate this issue by providing data over large swathes of the ocean at daily to weekly timescales. However, satellite observations have limitations, one of which is that they only measure the surface ocean, meaning that valuable subsurface information is not consistently observed. More recently, underwater robots, such as Argo floats and gliders, have been effective for providing consistent subsurface information about ocean biogeochemistry; however, they cannot provide the same spatiotemporal resolution of the global ocean as satellite imagery. In other words, there are unavoidable gaps in time (usually days to weeks) and horizontal space (1 to 100 km). With that said, there is a complementary nature to the two technologies: floats provide the information *beneath* the ocean's surface, while satellites provide information *across* the ocean's surface. Combining these two pieces of information about the ocean with numerical models – and extensive validation – will be an important next step for Earth observation.

Appendix A

Data Processing Note

Float #5906004 contains a single pH profile labeled as 'delayed mode' but is not accompanied by a profile-level quality flag for pH. This profile was removed from Figure 2.

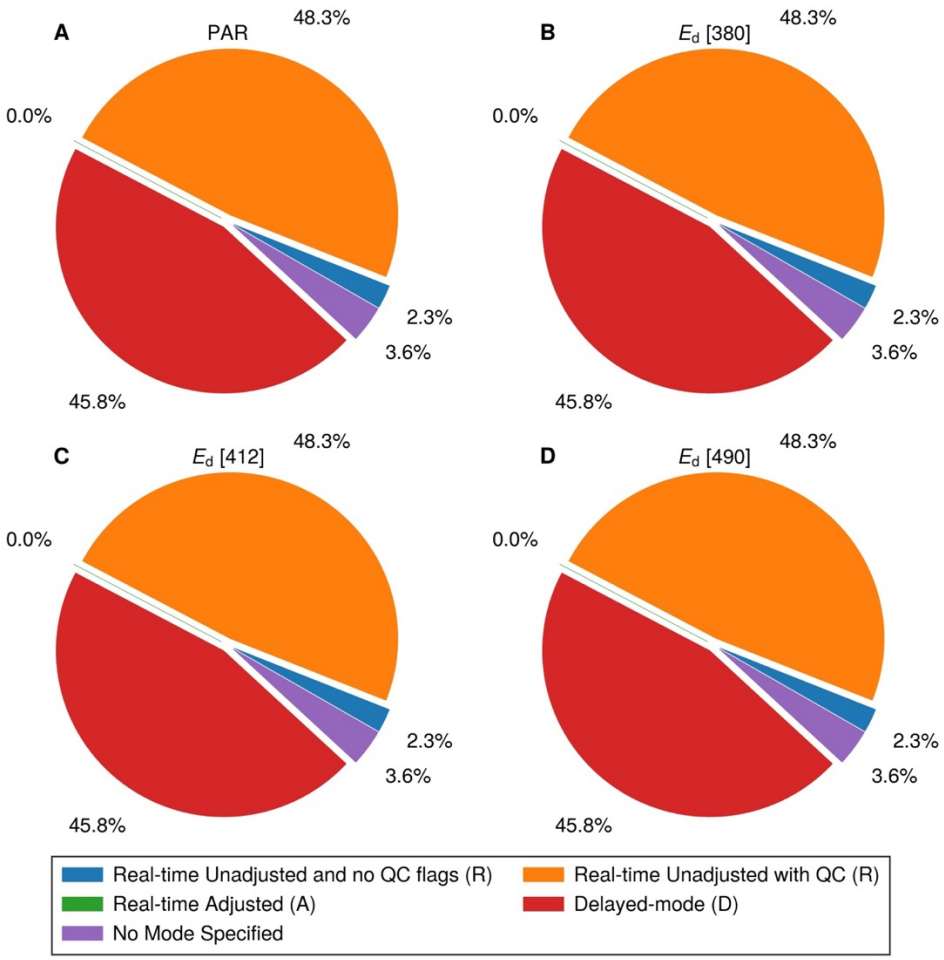

Figure A1. Percentage of profiles based on the type of quality-control procedure applied for the four most common downlight light parameters: (**A**) PAR, and E_d at (**B**) 380 nm, (**C**) 412 nm, and (**D**) 490 nm. Only floats that had all four of these channels are reported here.

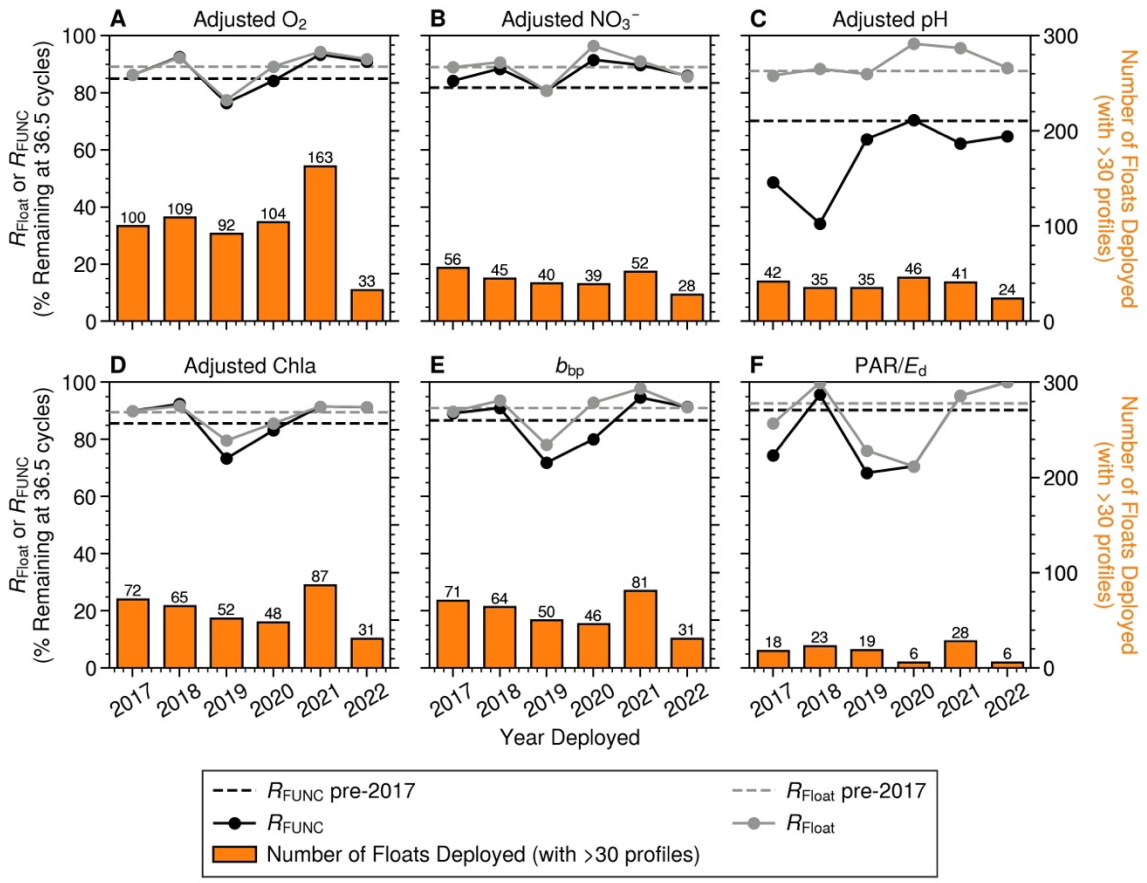

Figure A2. Survival rates of floats (R_{Float}) and functional profiles (R_{FUNC}) by deployment year. Each of the six key BGC variables: (**A**) adjusted O_2, (**B**) adjusted NO_3^-, (**C**) adjusted pH, (**D**) adjusted Chla, (**E**) b_{bp}, and (**F**) PAR/E_d. The solid line represents R_{Float} (grey) and R_{FUNC} (black) by year from 2017 to 2022. The horizontal dashed line in each subplot represents R_{Float} (grey) and R_{FUNC} (black) before 2017. The number of floats with quality-controlled data (and adjusted data when relevant) deployed each year are reported as the bar plot at bottom of each subplot and on the top of each bar. The number of floats deployed before 2017 are 813 for O_2; 144 for NO_3^-; 60 for pH; 249 for Chla; 238 for b_{bp}; and 128 for PAR/E_d. Note that only floats deployed for more than 300 days before January 1, 2023, were used to standardize float lifetimes for the survival rate calculation (see Section 2.2.2.3).

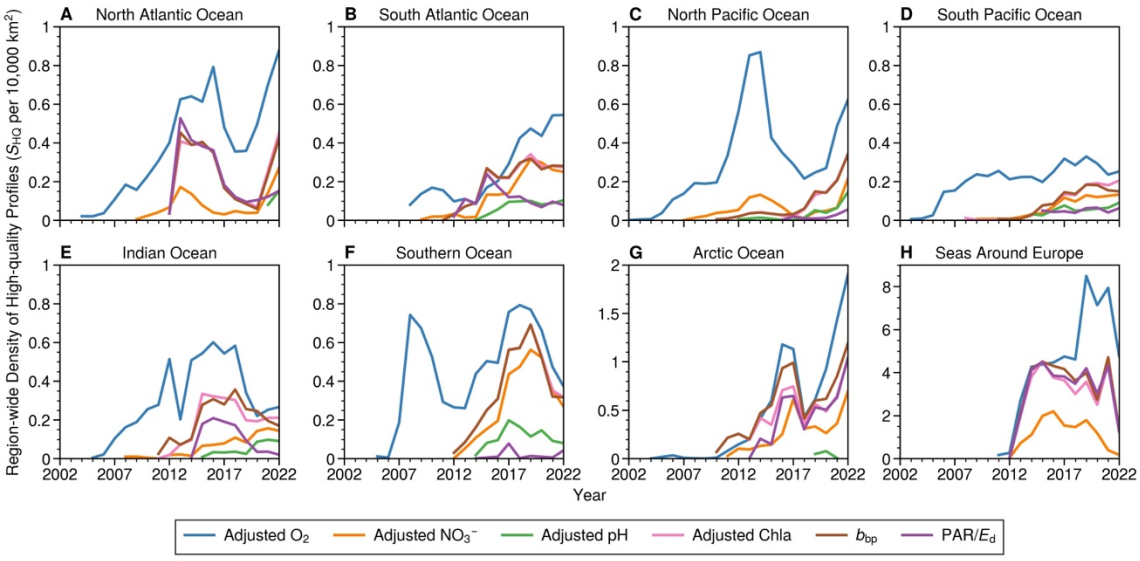

Figure A3. Region-wide density of high-quality profiles taken each year for each BGC parameter in the (**A**) North Atlantic, (**B**) South Atlantic, (**C**) North Pacific, (**D**) South Pacific, (**E**) Indian Ocean, (**F**) Southern Ocean, (**G**) Arctic Ocean, and the (**H**) seas around Europe. For regions in **A**–**G**, areas shallower than 200 m were removed. The average number of high-quality profiles for co-located PAR and E_d profiles was used.

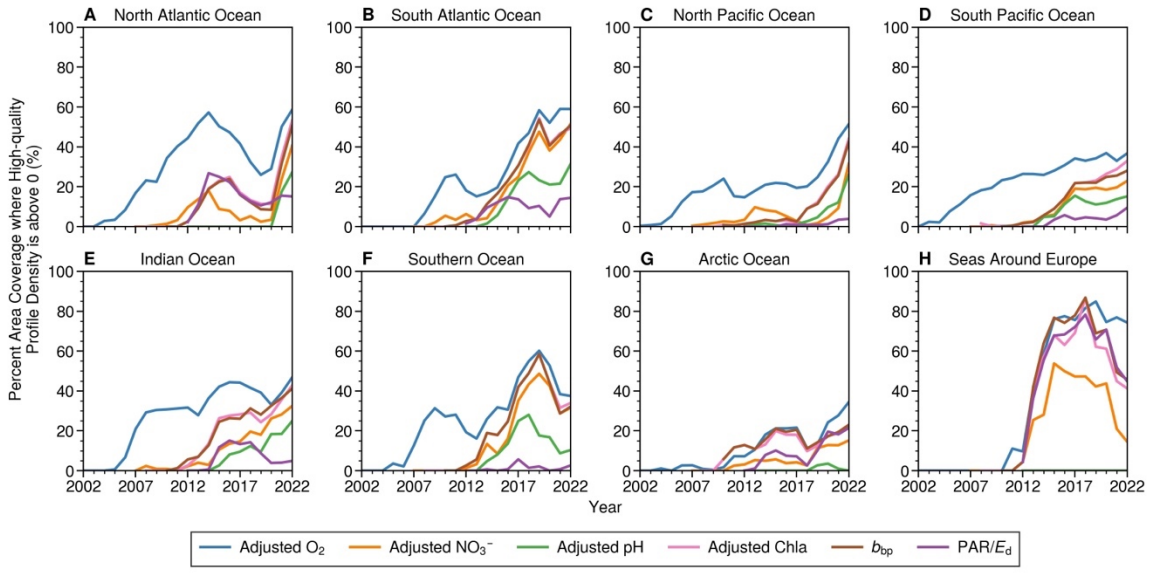

Figure A4. Percent area coverage where high-quality profile density is above 0 for each BGC parameter in the (**A**) North Atlantic, (**B**) South Atlantic, (**C**) North Pacific, (**D**) South Pacific, (**E**) Indian Ocean, (**F**) Southern Ocean, (**G**) Arctic Ocean, and (**H**) seas around Europe. For regions in **A**–**G**, areas shallower than 200 m were removed. The average number of high-quality profiles for co-located PAR and E_d profiles was used.

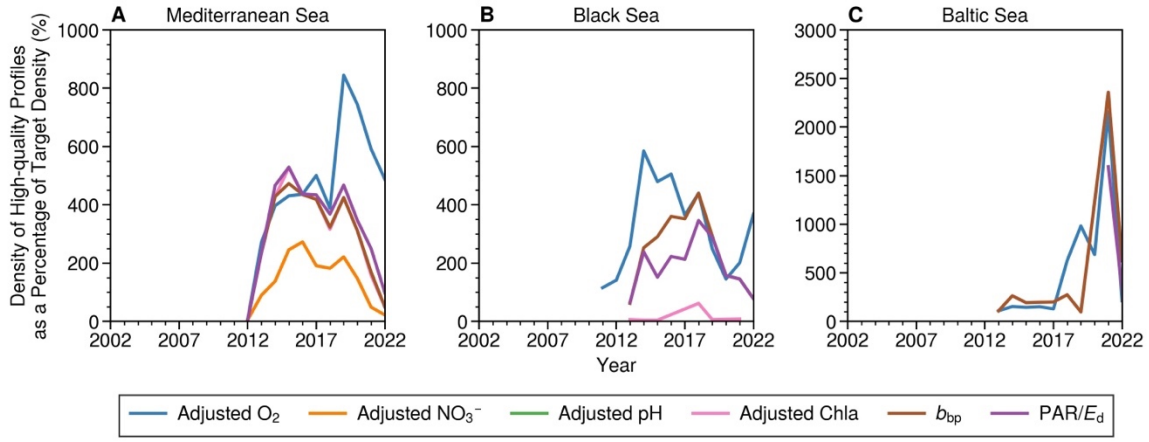

Figure A5. High-quality profile density as a percentage of the targeted high-quality profiles per year with each BGC parameter in the (**A**) Mediterranean Sea, (**B**) Black Sea, and (**C**) Baltic Sea. Other figure details in Figure 7 are same as in this figure.

Table A1. Floats deployed and raw ascending profiles collected up to 2022. Profiles with any mode of processing are reported here. For downwelling light data, only floats simultaneously collecting PAR and E_d at 380, 412, 490 nm are reported.

BGC Property	Floats Deployed	Profiles Collected
O_2	1,754	251,855
NO_3^-	533	60,017
pH	447	39,483
Chla	805	111,703
b_{bp}	791	108,703
PAR, E_d [380], E_d [412], E_d [490]	273	46,028

Table A2. Floats deployed, profiles collected, and the associated quality control up to 2022. Profiles with only real-time adjusted or delayed-mode processing are reported for O_2, NO_3^-, pH, and Chla. A mix of unadjusted and adjusted measurements are reported for b_{bp} and PAR/E_d. Only quality-controlled profiles are reported here.

BGC Property	Floats	QC'd Profiles	Profile Quality Control Scale			Functional Sensors Scale	
			S_{HQ}	S_{LQ}	S_{UNRES}	S_{FUNC}	S_{FAIL}
Adjusted O_2	1,533	228,892	205,625	20,702	2,565	208,849	20,043
Adjusted NO_3^-	485	53,109	46,333	6,458	318	48,126	4,983
Adjusted pH	350	31,413	15,130	16,261	21	18,888	12,524
Adjusted Chla	747	91,277	78,033	12,929	315	85,700	5,577
b_{bp}	717	91,979	79,987	6,693	5,299	81,029	10,950
PAR	261	44,947	41,151	1,145	2,651	41,865	3,082
E_d [380]			41,500	796	2,651	41,871	3,076
E_d [412]			41,496	800	2,651	41,867	3,080
E_d [490]			41,444	852	2,651	41,814	3,133

Table A3. Survival rates of floats (R_{Float}) and functional profiles (R_{FUNC}) for different periods, manufacturers, and models of sensors. The hyphen (-) indicates that too few sensors (less than 10) were available to calculate meaningful survival rates. Note that float numbers do not always add up to the total because some floats were missing metadata about the manufacturer and model but had QC flags. For Chla and suspended particle sensors, all ECO- and MCOMS-type models were grouped together. I only considered downwelling light data from floats that simultaneously measured PAR and E_d at 380, 412, and 490 nm wavelengths.

Parameter, Manufacturer, or Model	Number of Floats Deployed				R_{FUNC} / R_{Float}			
	Before 2017	2017–2019	2020–2022	All	Before 2017	2017–2019	2020–2022	All
Adjusted O_2	817	301	302	1420	85%/89%	85%/86%	90%/92%	86%/89%
Aanderaa	637	268	258	1163	89%/91%	88%/88%	91%/93%	89%/91%
3830/3835	257	0	0	257	91%94%	-	-	91%/94%
4330/4831	379	268	258	905	87%/90%	88%/88%	91%/93%	88%/90%
JAC ARO/D-FT	0	5	12	17	-	-	93%/92%	66%/67%
SBE	176	28	32	236	74%/83%	80%/80%	83%/90%	76%/84%
SBE43	132	0	13	145	71%/82%	-	93%/97%	73%/84%
SBE63	44	28	19	91	82%/87%	80%/80%	77%/85%	81%/84%
Adjusted NO_3^-	144	141	121	406	82%/89%	85%/87%	89%/92%	85%/89%
MBARI ISUS	83	100	78	261	84%/97%	84%/88%	93%/96%	87%/93%
SBE/Satlantic	61	41	43	145	78%/78%	85%/84%	83%/83%	81%/81%
ISUS	3	0	0	3	-	-	-	-
SUNA	18	11	0	29	63%/63%	70%/69%	-	66%/65%
SUNA V2	40	30	43	113	87%/87%	90%/89%	83%/83%	86%/86%
Adjusted pH	60	112	113	285	70%/88%	49%/87%	66%/95%	60%/90%
MBARI DURAFET	50	102	50	202	73%/91%	49%/89%	82%/97%	63%/91%
SBE SEAFET	10	10	63	83	55%/71%	52%/65%	53%/93%	53%/87%
Adjusted Chla	249	189	168	606	86%/89%	86%/88%	89%/90%	87%/89%
SBE/Wetlabs	240	189	168	597	85%/89%	86%/88%	89%/90%	86%/89%
ECO	225	177	145	547	86%/90%	87%/89%	88%/89%	87%/89%
MCOMS	15	12	23	50	72%/72%	72%/72%	92%/92%	81%/81%
b_{bp}	238	185	160	583	87%/91%	85%/88%	90%/95%	87%/91%
SBE/Wetlabs	229	185	160	574	86%/91%	85%/88%	90%/95%	87%/91%
ECO	214	174	137	525	87%/92%	86%/89%	89%/95%	87%/92%
MCOMS	15	11	23	49	72%/72%	69%/69%	92%/92%	81%/81%
Downwelling light (SBE/Satlantic OCR-504)								
380 nm	128	60	40	228	90%/93%	81%/88%	92%/92%	88%/91%
412 nm					90%/93%	81%/88%	92%/92%	88%/91%
490 nm					90%/93%	81%/88%	92%/92%	88%/91%
PAR					90%/93%	81%/88%	92%/92%	88%/91%

Table A4. Accumulated density of high-quality BGC profiles in each marine region. See Figure 6 for the corresponding high-quality profiles. The average number of high-quality profiles for co-located PAR/E_d profiles was used in the density calculation. Each density value is rounded to the second decimal place.

Marine Region	**Accumulated Density of High-Quality Profiles (S_{HQ} per 10,000 km^2)**					
	Adjusted O_2	**Adjusted NO_3^-**	**Adjusted pH**	**Adjusted Chla**	**b_{bp}**	**PAR/E_d**
North Atlantic Ocean	7.41	1.13	0.23	2.75	2.71	2.50
South Atlantic Ocean	3.93	1.87	0.66	2.35	2.35	1.21
North Pacific Ocean	6.40	1.01	0.36	1.08	1.11	0.14
South Pacific Ocean	4.09	0.90	0.51	1.25	1.17	0.41
Indian Ocean	5.59	0.93	0.41	2.27	2.40	0.95
Southern Ocean	8.23	3.13	0.99	3.87	3.82	0.15
Arctic Ocean	9.13	3.34	0.13	6.05	7.37	4.66
Seas around Europe	54.97	12.61	0.00	32.58	35.75	34.65

Appendix B

Comparison with ^{14}C-NPP

It would be valuable to make a robust comparison between float-based-NPP and ^{14}C-NPP, the standard for measuring oceanic NPP; however, the Southern Ocean lacks consistent shipboard measurements to allow for such a comparison. While in the Northern Hemisphere around the Bermuda and Hawaii time series sites such a comparison is prevented by the limited number of acceptable b_{bp} profiles. Despite these setbacks, a simple comparison for the Southern Ocean was made as follows. I compiled 26 profiles of ^{14}C-NPP measurements from the month of March by combing two publicly available databases (Mattei and Scardi, 2021b; Marra, 2022). The relevant incubation methods are described by Mattei and Scardi (2021a) and Marra et al. (2021). I compared these shipboard measurements with float-based estimates between 40 to 70°S for the periods of February to April. Estimates of NPP from ^{14}C were grouped into 10-m wide depth bins from the surface to 100 m depth and the median, minimum, and maximum NPP at each depth were calculated. Measurements made at 0 m were included in the 0–10 m depth bin.

The float-based NPP estimates made in the South Indian Ocean are similar to those made from bottle incubations of ^{14}C (Figure 9; Figure B**2**). The estimates of volumetric $NPP_{b_{bp}}$ and $NPP_{\Delta O_2}$ ranged from 101–158 and 45–84 mmol C m^{-3}, respectively, in the top 30 m, where diel cycles are strongest. These ranges are reasonably close to the median profile of ^{14}C-NPP of 85–133 mmol C m^{-3} and are within range of ^{14}C-NPP at the same depths. For greater depths, float-based NPP is generally outside of the range ^{14}C-

NPP. I suspect that at these depths, productivity is weaker and more susceptible to abiotic influences, potentially explaining the negative $NPP_{\Delta O_2}$ (or GOP) and the subsurface peak in $NPP_{b_{bp}}$ (Figure B**2**).

Additional Sensitivity Analysis Results

The sensitivity of NPP due to ±10 m variation in the z_{eu} yields notably different NPP estimates. Because $NPP_{\Delta O_2}$ tends to have more negative values at greater depths than $NPP_{b_{bp}}$, I find that $\Sigma NPP_{\Delta O_2}$ declines while $\Sigma NPP_{b_{bp}}$ increases when z_{eu} is deepened by 10 m. When z_{eu} is decreased by 10 m, both float-based estimates of NPP decline. The uncertainty in z_{eu} (derived from satellite observation) and the sensitivity of float-based NPP highlights the need for radiometry on BGC-Argo floats, which can be used to provide an accurate measurement of z_{eu}.

Different conversion algorithms tested in the sensitivity analysis yielded a wide range in zonal NPP. For south of 30°S, $NPP_{b_{bp}}$ ranges from 5.3 to 20.4 Pg y^{-1}, and south of 50°S, from 2.2 to 8.2 Pg y^{-1} (Table B1). While some of these algorithms represent the extremes in the b_{bp} -to-POC relationships, the multi-model means (10.5 Pg y^{-1} and 4.5 Pg y^{-1}, respectively) are reasonably close to our reported values. Some of these algorithms do not account for DOC absorption to the filter during POC filtration, which may lead to overestimates of POC and thus $NPP_{b_{bp}}$. Similarly, the choice of the spectral slope is another source of uncertainty that results in appreciably different $NPP_{b_{bp}}$ estimates (Table B1). More research is needed to determine the conversion factors best suited for predicting POC from b_{bp} measured by Bgc-argo floats.

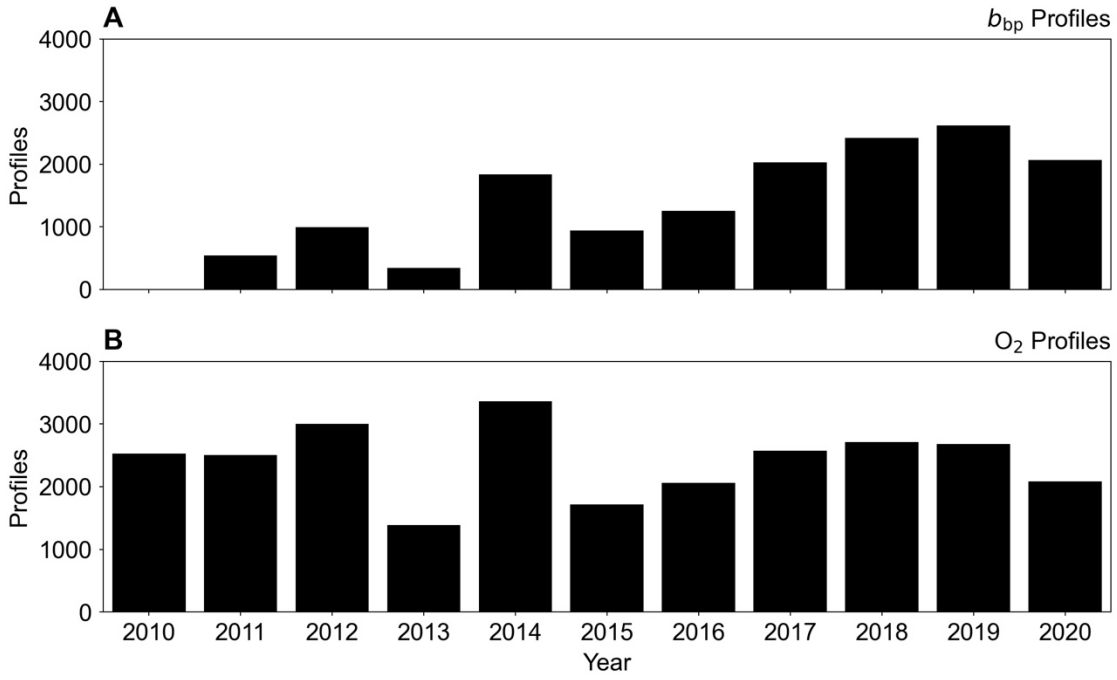

Figure B1. The total number of (**A**) b_{bp} and (**B**) O_2 profiles collected each year from 2010 to 2020 in the region of 30–70°S.

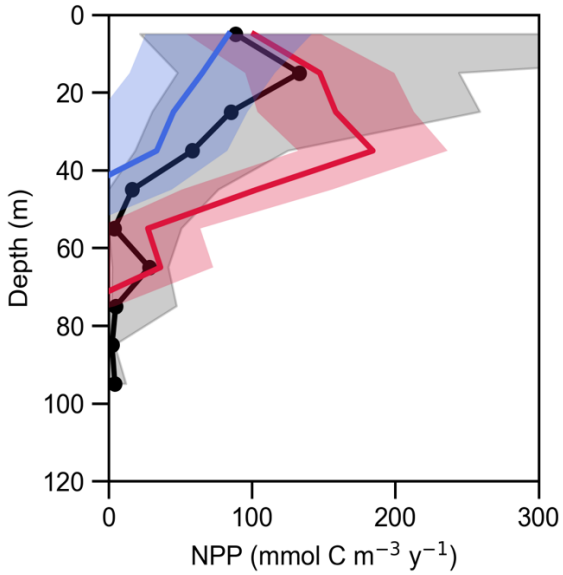

Figure B2. Float-based $NPP_{\Delta O_2}$ (blue line) and $NPP_{b_{bp}}$ (red line) between 40 and 70°S for the period of February to April. In both panels, the median profile of ^{14}C-NPP (black line) taken during the month of March is shown for comparison. The shaded region for float-based NPP represent one standard error while for ^{14}C-NPP it represents the range of observed NPP.

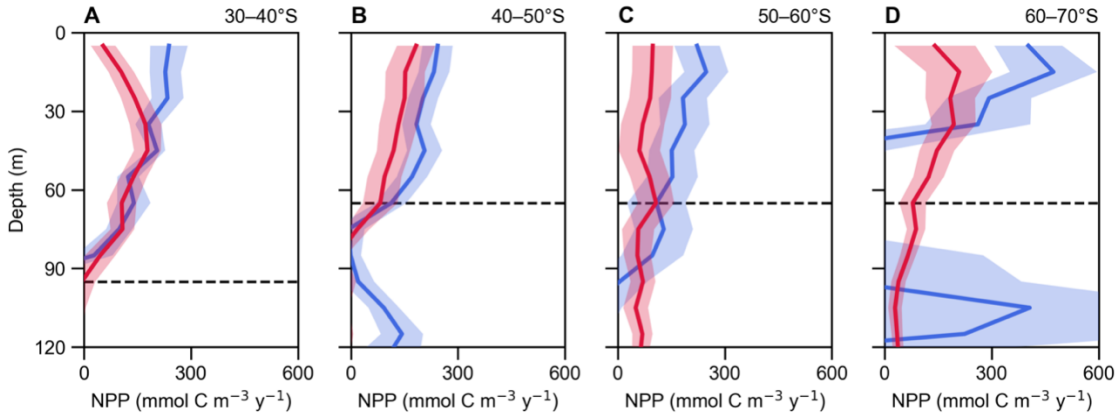

Figure B3. (**A**–**D**) Annual NPP based on co-located O_2 and b_{bp} profiles by latitude. The red lines represent $NPP_{b_{bp}}$ and the blue lines represent $NPP_{\Delta O_2}$. The shaded regions represent one standard error. The 1% euphotic depth is shown as a dashed horizontal line in each panel.

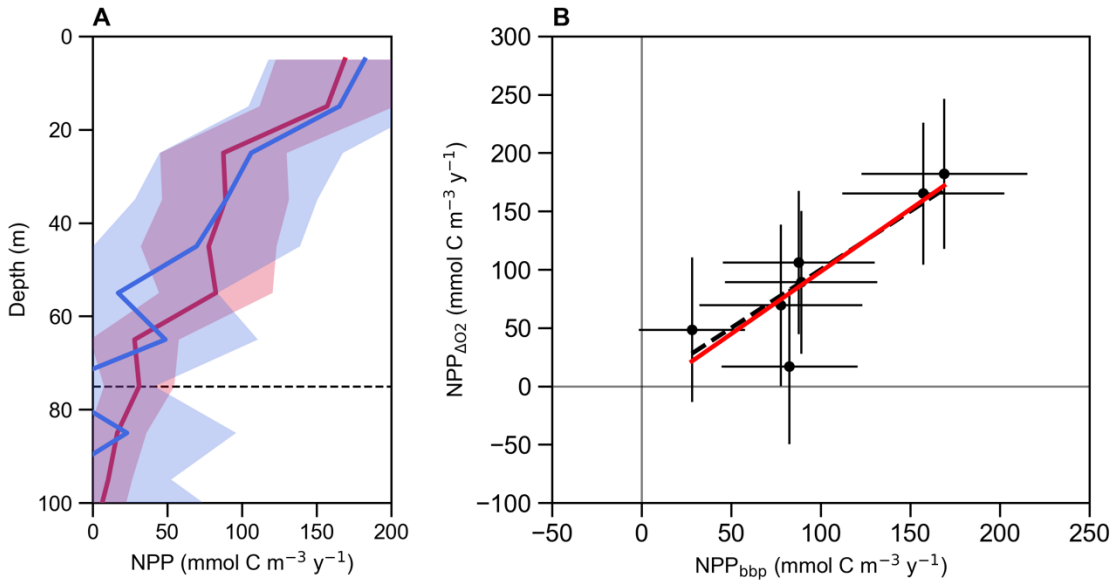

Figure B4. Comparison between co-located $NPP_{b_{bp}}$ and $NPP_{\Delta O_2}$ from 30–70°S. (**A**) All float profiles with both O_2 and b_{bp} measurements were used to estimate $NPP_{b_{bp}}$ and $NPP_{\Delta O_2}$ shown as red and blue lines, respectively. (**B**) A least squares linear regression was applied to all NPP data points above the euphotic depth. The trend line is represented by the equation $NPP_{\Delta O_2} = 1.07 \times NPP_{b_{bp}} - 9$ (p-value = 0.01; $R^2 = 0.78$; n = 7) and is shown in red in panel **B**. The 1:1 line is shown as a black dashed line in (**B**). The standard error of each point is shown by shaded regions in (**A**) and as the horizontal and vertical lines in (**B**).

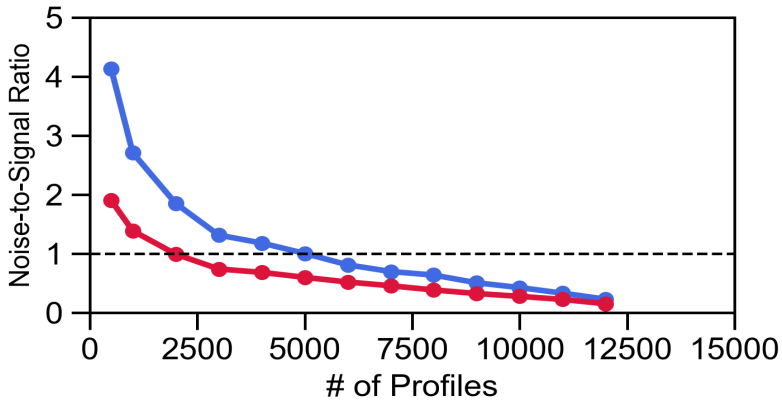

Figure B5. Noise-to-signal ratio from bootstrapping analysis using b_{bp} and O_2 from 30–70°S. The curve describes one standard deviation divided by the mean at each sample size for $NPP_{\Delta O2}$ (blue line) and $NPP_{b_{bp}}$ (red line). The dashed line represents when the standard deviation is equal to the mean.

Table B1. Sensitivity analysis involving different parameters and years. See more details below.

Parameter Changed									Below 30°S		Below 50°S			Statistics		
Measure of Center	Min hours[a]	Threshold X[b]	Outlier X[c]	Conversion Model[d]	Spectral Slope	z_{eu}[e]	Model Fit[f]	Years	$NPP_{\Delta O_2}$ (Pg C y^{-1})[g]	$NPP_{b_{bp}}$ (Pg C y^{-1})[g]	$NPP_{\Delta O_2}$ (Pg C y^{-1})[g]	$NPP_{b_{bp}}$ (Pg C y^{-1})[g]	O_2-Profiles	b_{bp} - Profiles	Slope[h]	R^2
Median	18	3	-	G15	0.78	NC	S	2010-2020	11.9 ± 6.6	11.4 ± 1.1	2.5 ± 6.6	4.6 ± 0.8	27,848	15,736	1.21*	0.73
Median	19	3	-	G15	0.78	NC	S	2010-2020	10.7 ± 6.6	11.2 ± 1.1	2.5 ± 6.6	4.6 ± 0.8	27,737	15,625	0.96*	0.59
Median	20	3	-	G15	0.78	NC	S	2010-2020	10.3 ± 6.6	11.2 ± 1.1	2.1 ± 6.6	4.7 ± 0.8	27,475	15,422	0.99*	0.66
Median	21	3	-	G15	0.78	NC	S	2010-2020	11.7 ± 5.6	11.4 ± 1.1	3.5 ± 5.6	4.6 ± 0.8	26,611	15,052	1.07*	0.76
Median	22	3	-	G15	0.78	NC	S	2010-2020	13.5 ± 5.1	11.9 ± 1.2	4.5 ± 5.0	5.1 ± 0.9	25,632	14,712	1.47*	0.72
Median	23	3	-	G15	0.78	NC	S	2010-2020	14.5 ± 4.2	12.0 ± 1.3	5.8 ± 4.1	4.8 ± 0.9	24,362	14,231	1.29*	0.75
Median	24	3	-	G15	0.78	NC	S	2010-2020	15.3 ± 3.9	9.5 ± 1.5	7.0 ± 3.8	4.7 ± 1.0	20,978	12,638	1.04*	0.85
Median	21	3	-	G15	0.78	+10 m	S	2010-2020	9.9 ± 7.8	12.3 ± 1.2	2.2 ± 7.8	5.2 ± 0.8	26,611	15,052	1.24*	0.79
Median	21	3	-	G15	0.78	-10 m	S	2010-2020	11.1 ± 3.7	10.4 ± 1.0	3.4 ± 3.6	4.0 ± 0.7	26,611	15,052	1.34*	0.79
Median	21	3	-	G15	0.41	NC	S	2010-2020	11.7 ± 5.6	9.8 ± 0.8	3.5 ± 5.6	4.0 ± 0.6	26,611	15,052	1.24*	0.76
Median	21	3	-	S99-RS	0.78	NC	S	2010-2020	11.7 ± 5.6	20.4 ± 3.7	3.5 ± 5.6	8.2 ± 2.4	26,611	15,052	0.59*	0.76
Median	21	3	-	S99-APFZ	0.78	NC	S	2010-2020	11.7 ± 5.6	8.4 ± 0.6	3.5 ± 5.6	3.4 ± 0.4	26,611	15,052	1.47*	0.75
Median	21	3	-	S99	0.78	NC	S	2010-2020	11.7 ± 5.6	14.5 ± 1.8	3.5 ± 5.6	5.9 ± 1.2	26,611	15,052	0.84*	0.76
Median	21	3	-	S99-NU	0.78	NC	S	2010-2020	11.7 ± 5.6	11.0 ± 1.0	3.5 ± 5.6	4.5 ± 0.7	26,611	15,052	1.11*	0.76
Median	21	3	-	C12	N/a	NC	S	2010-2020	11.7 ± 5.6	6.1 ± 0.3	3.5 ± 5.6	2.5 ± 0.2	26,611	15,052	2.01*	0.76
Median	21	3	-	J17	N/a	NC	S	2010-2020	11.7 ± 5.6	5.3 ± 0.2	3.5 ± 5.6	2.2 ± 0.2	26,611	15,052	2.28*	0.76
Median	21	3	-	T17	0.78	NC	S	2010-2020	11.7 ± 5.6	9.2 ± 0.7	3.5 ± 5.6	3.7 ± 0.5	26,611	15,052	1.32*	0.76
Median	21	3	-	R17	0.78	NC	S	2010-2020	11.7 ± 5.6	9.2 ± 0.7	3.5 ± 5.6	3.7 ± 0.5	26,611	15,052	1.31*	0.76
Median	18	3	-	G15	0.78	NC	L	2010-2020	**12.7 ± 9.6**	12.1 ± 1.8	**1.3 ± 9.6**	5.0 ± 1.2	27,848	15,736	0.95*	0.60
Median	19	3	-	G15	0.78	NC	L	2010-2020	**11.2 ± 9.6**	11.8 ± 1.8	**1.3 ± 9.6**	4.8 ± 1.3	27,737	15,625	0.56	0.34
Median	20	3	-	G15	0.78	NC	L	2010-2020	**10.6 ± 9.6**	12.0 ± 1.8	**0.7 ± 9.6**	5.2 ± 1.3	27,475	15,422	0.72*	0.46
Median	21	3	-	G15	0.78	NC	L	2010-2020	11.8 ± 8.4	12.3 ± 1.8	2.2 ± 8.3	5.1 ± 1.2	26,611	15,052	0.87*	0.59
Median	22	3	-	G15	0.78	NC	L	2010-2020	13.9 ± 7.8	12.8 ± 2.0	3.0 ± 7.7	3.0 ± 7.7	25,632	14,712	1.34*	0.58
Median	23	3	-	G15	0.78	NC	L	2010-2020	15.7 ± 6.7	13.1 ± 2.0	4.7 ± 6.6	5.1 ± 1.5	24,362	14,231	1.18*	0.65
Median	24	3	-	G15	0.78	NC	L	2010-2020	17.0 ± 6.1	10.2 ± 2.3	6.5 ± 6.0	4.8 ± 1.6	20,978	12,638	0.76*	0.67
Mean	18	3	3	G15	0.78	NC	S	2010-2020	**9.6 ± 6.9**	13.3 ± 1.5	**0.4 ± 6.8**	5.0 ± 1.1	27,848	15,736	8.00*	0.88
Mean	19	3	3	G15	0.78	NC	S	2010-2020	**8.4 ± 6.9**	13.2 ± 1.5	**0.4 ± 6.8**	5.0 ± 1.1	27,737	15,625	7.62*	0.89
Mean	20	3	3	G15	0.78	NC	S	2010-2020	**7.9 ± 7.1**	13.4 ± 1.5	**0.0 ± 7.1**	5.1 ± 1.1	27,475	15,422	7.88*	0.88
Mean	21	3	3	G15	0.78	NC	S	2010-2020	**9.0 ± 6.3**	14.2 ± 1.6	**0.7 ± 6.2**	5.2 ± 1.2	26,611	15,052	6.65*	0.80
Mean	22	3	3	G15	0.78	NC	S	2010-2020	11.0 ± 4.5	14.0 ± 1.6	2.3 ± 4.4	5.0 ± 1.2	25,632	14,712	**9.23***	**0.85**
Mean	23	3	3	G15	0.78	NC	S	2010-2020	12.0 ± 4.4	13.0 ± 1.7	2.7 ± 4.3	4.3 ± 1.3	24,362	14,231	**8.78***	**0.82**
Mean	24	3	3	G15	0.78	NC	S	2010-2020	14.9 ± 2.8	9.0 ± 1.8	5.7 ± 2.6	4.1 ± 1.3	20,978	12,638	**4.20***	**0.88**
Mean	18	3	5	G15	0.78	NC	S	2010-2020	**8.7 ± 6.6**	12.5 ± 1.8	**-0.3 ± 6.5**	4.4 ± 1.6	27,848	15,736	2.92*	0.80
Mean	19	3	5	G15	0.78	NC	S	2010-2020	**7.6 ± 6.6**	12.6 ± 1.8	**-0.3 ± 6.5**	4.3 ± 1.6	27,737	15,625	2.66*	0.79
Mean	20	3	5	G15	0.78	NC	S	2010-2020	**7.3 ± 6.8**	13.0 ± 1.7	**-0.5 ± 6.8**	4.6 ± 1.5	27,475	15,422	2.59*	0.84
Mean	21	3	5	G15	0.78	NC	S	2010-2020	**8.2 ± 6.0**	13.6 ± 1.9	**0.0 ± 5.9**	4.6 ± 1.6	26,611	15,052	2.37*	0.79
Mean	22	3	5	G15	0.78	NC	S	2010-2020	10.5 ± 4.1	**12.8 ± 1.8**	1.8 ± 4.0	**3.8 ± 1.6**	25,632	14,712	3.11*	0.75
Mean	23	3	5	G15	0.78	NC	S	2010-2020	12.4 ± 4.0	**12.3 ± 2.0**	3.2 ± 3.8	**3.6 ± 1.8**	24,362	14,231	**3.65***	**0.79**
Mean	24	3	5	G15	0.78	NC	S	2010-2020	15.4 ± 2.8	**7.1 ± 1.9**	6.0 ± 2.4	**2.9 ± 1.5**	20,978	12,638	**1.70***	**0.77**
Median	18	5	-	G15	0.78	NC	S	2010-2020	**9.4 ± 6.2**	10.8 ± 1.3	**1.1 ± 6.1**	4.1 ± 0.7	31,938	17,578	1.09*	0.59
Median	19	5	-	G15	0.78	NC	S	2010-2020	**9.6 ± 6.9**	12.5 ± 1.2	**2.1 ± 6.8**	4.7 ± 0.7	31,711	17,404	0.76	0.32
Median	20	5	-	G15	0.78	NC	S	2010-2020	10.2 ± 6.9	12.4 ± 1.2	2.9 ± 6.8	4.6 ± 0.7	31,255	17,012	0.77	0.38
Median	21	5	-	G15	0.78	NC	S	2010-2020	10.3 ± 7.1	13.0 ± 1.3	3.4 ± 7.0	4.9 ± 0.7	29,884	16,319	1.28*	0.78
Median	22	5	-	G15	0.78	NC	S	2010-2020	10.9 ± 7.6	13.4 ± 1.6	2.2 ± 7.5	5.3 ± 1.2	28,100	15,942	1.58*	0.89
Median	23	5	-	G15	0.78	NC	S	2010-2020	11.5 ± 5.1	13.5 ± 1.5	3.4 ± 5.0	5.2 ± 1.1	26,757	15,354	1.49*	0.82
Median	24	5	-	G15	0.78	NC	S	2010-2020	13.0 ± 4.2	9.3 ± 1.9	6.3 ± 4.1	3.8 ± 1.2	22,657	13,468	1.27*	0.87
Median	18	3	-	G15	0.78	NC	S	2010-2021	12.3 ± 6.4	10.1 ± 1.1	2.5 ± 6.3	5.0 ± 0.8	30,008	17,645	0.92	0.38
Median	19	3	-	G15	0.78	NC	S	2010-2021	12.2 ± 6.4	10.3 ± 1.1	2.5 ± 6.3	5.1 ± 0.8	29,985	17,622	0.92	0.36
Median	20	3	-	G15	0.78	NC	S	2010-2021	**10.9 ± 6.9**	9.1 ± 1.1	**1.3 ± 6.8**	3.8 ± 0.9	29,764	17,402	1.25*	0.63
Median	21	3	-	G15	0.78	NC	S	2010-2021	12.5 ± 6.4	9.3 ± 1.1	2.8 ± 6.3	4.0 ± 0.9	29,233	17,297	1.23*	0.68
Median	22	3	-	G15	0.78	NC	S	2010-2021	15.1 ± 2.9	9.1 ± 1.1	4.7 ± 2.8	3.8 ± 0.8	28,407	16,978	1.66*	0.70
Median	23	3	-	G15	0.78	NC	S	2010-2021	14.4 ± 2.9	9.3 ± 1.1	4.6 ± 2.7	3.8 ± 0.7	26,981	16,430	1.39*	0.62

Median	24	3	-	G15	0.78	NC	S	2010-2021	15.4 ± 2.7	10.2 ± 1.3	7.0 ± 2.6	4.4 ± 0.9	23,008	14,633	1.33*	0.67
Median	18	5	-	G15	0.78	NC	S	2010-2021	**9.7 ± 4.7**	10.8 ± 1.1	**1.6 ± 4.6**	4.6 ± 0.7	34,507	19,859	1.46*	0.63
Median	19	5	-	G15	0.78	NC	S	2010-2021	**9.7 ± 4.7**	10.8 ± 1.1	**1.6 ± 4.6**	4.6 ± 0.7	34,459	19,836	1.45*	0.62
Median	20	5	-	G15	0.78	NC	S	2010-2021	**9.3 ± 4.5**	10.2 ± 1.1	**1.3 ± 4.4**	3.7 ± 0.7	34,093	19,476	**1.70***	**0.77**
Median	21	5	-	G15	0.78	NC	S	2010-2021	11.7 ± 4.5	10.7 ± 1.1	3.5 ± 4.4	3.7 ± 0.7	33,146	19,073	1.68*	0.86
Median	22	5	-	G15	0.78	NC	S	2010-2021	12.0 ± 3.5	10.5 ± 1.1	2.6 ± 3.3	3.7 ± 0.6	31,203	18,365	2.06*	0.70
Median	23	5	-	G15	0.78	NC	S	2010-2021	11.6 ± 3.0	9.0 ± 1.3	2.5 ± 2.7	2.8 ± 0.8	29,677	17,747	2.14*	0.85
Median	24	5	-	G15	0.78	NC	S	2010-2021	11.5 ± 2.7	10.7 ± 1.7	5.7 ± 2.5	4.1 ± 0.9	25,020	15,503	1.95*	0.72
Median	23	3	-	G15	0.78	NC	S	2010-2021	14.4 ± 2.9	9.3 ± 1.1	4.6 ± 2.7	3.8 ± 0.7	26,981	16,430	1.21*	0.73
								Mean ± standard deviation[i] (with negative ΣNPP)	11.5 ± 2.3	11.3 ± 2.3	2.8 ± 2.3	4.4 ± 0.9			2.17 ± 2.11	0.71 ± 0.14
								Range (with negative ΣNPP)	7.3–17.0	5.3-20.4	-0.5-7.0	2.2-8.2			0.56–9.23	0.32–0.89
								Mean ± standard deviation[i] (with negative ΣNPP)	12.6 ± 1.9	11.3 ± 2.3	3.8 ± 1.6	4.5 ± 0.9			1.86 ± 1.72	0.70 ± 0.14
								Range (with negative ΣNPP)	9.9-17.0	5.3-20.4	1.8-7.0	2.2-8.2			0.56–8.00	0.32-0.89

The cells shaded in gray shows the parameters used in the main analysis. [a]The number of unique local hours the float had to have observed. [b]The threshold multiplier is multiplied by the expected number of profiles. [c]When using the mean as the center value for each local hour, the outliers are defined as any values around the mean that are the outlier multiplier times the standard deviation. [d]The model used to estimate POC from bbp. G15 = Graff et al. (2015); C12 = (Cetinić et al., 2012); T17 = Thomalla et al. (2017b); S99-RS = Stramski et al. (1999) – Ross Sea Data; S99-APFZ = Stramski et al. (1999) – Antarctic Polar Frontal Zone Sea Data; S08 = Stramski et al. (2008); S08-NU = Stramski et al. (2008) – excluding upwelling data. R17 = Rasse et al. (2017); J17 = Johnson et al. (2017).[e]NC means "no change" to the z_{eu} values estimated. [f]S = sinusoidal model fit; L = linear model fit. See details in Barone et al. (2019). [g]Bolded values highlight totals that include negative ΣNPP from any latitudinal group. These negative estimates mainly occurred either in the 50-60°S or 60-70°S regions and mainly with NPPDO2. [h]The relationship between NPPDO2 and NPPbbp from all measurements from 30-70°S. A star is used to indicate if the regression is significant below the 0.1 significance level. [i]Mean and one standard deviations of mean/medians NPP totals. The means exclude rows 13 to 21 for NPP estimates and rows 11 to 21 for the average of all R^2 values (go to e). Note that a spectral slope of 0.41 comes from Cetinić et al. (2012).

Table B2. Total NPP south of 30°S from co-located b_{bp}-and O_2 profiles. The area is calculated from ETOPO5 using all grid cells deeper than 2,000 m. The climatological mean euphotic depth was obtained from NASA Ocean Color and was rounded to the nearest depth bin's center. Argo data is from 2010 to 2020 (inclusive) and does not include profiles in waters less than 2,000 m deep. Total NPP below 30°S and 50°S is calculated as the sum of all latitudinal bands shown in the table. Errors represents one standard error.

Latitudinal Band	b_{bp} and O_2 Profiles	Area (10^{13} m^2)	z_{eu} (m)	$NPP_{b_{bp}}$ (Pg C y^{-1})	$NPP_{\Delta O_2}$ (Pg C y^{-1})
30–40°S	1,946	2.94	95	3.7 ± 0.5	5.2 ± 0.6
40–50°S	3,613	2.80	65	2.8 ± 0.5	4.2 ± 0.4
50–60°S	3,974	2.37	65	1.4 ± 0.6	3.2 ± 0.7
60–70°S	3,504	1.53	65	1.8 ± 0.6	1.7 ± 3.2
Total (below 30°S)	13,037	9.64	-	9.8 ± 1.1	14.3 ± 3.3
Total (below 50°S)	7,478	3.90	-	3.3 ± 0.8	4.9 ± 3.3

Appendix C

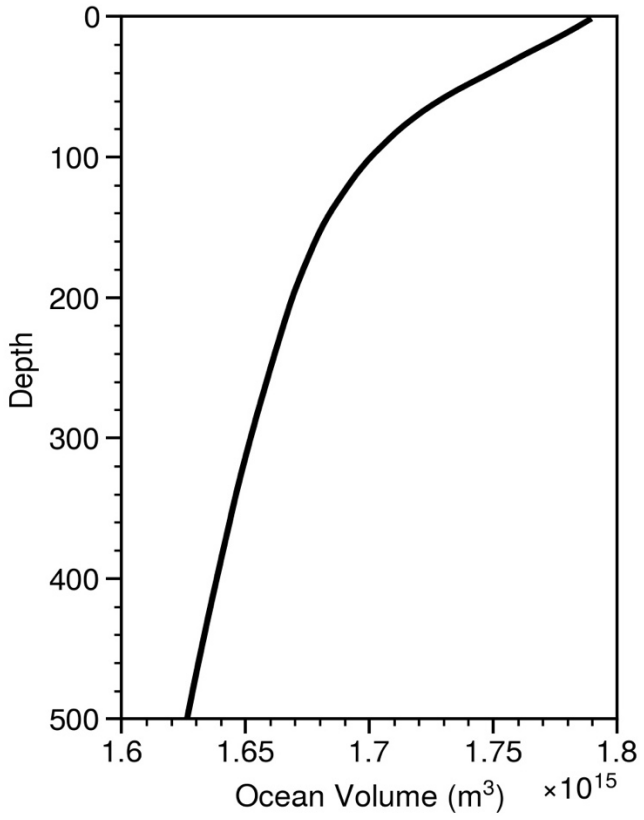

Figure C1. The change in ocean volume with depth was multiplied by the volumetric concentrations of Chla and C_{org} to calculate stocks. This calculation was made for each 10° latitude region and for each basin, although the figure here gives an example of what this profile looks like for the global ocean. Bathymetry was determined from the ETOPO 2022 Global Relief Model (60 arc-second resolution) for ice surface elevation. Area was calculated using the area function from GeoPandas in Python.

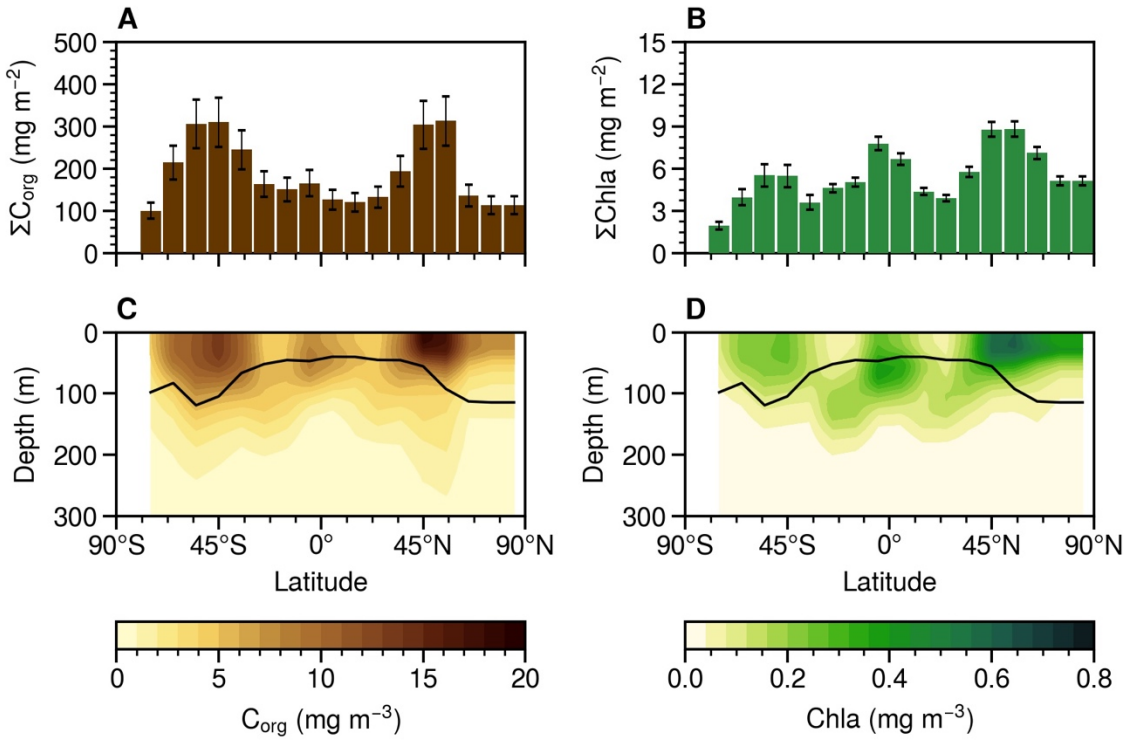

Figure C2. (**A**, **B**) Latitudinal distributions of Chla and C_{org} stock per area; and (**C**, **D**) vertical distributions of the volumetric concentrations of Chla and C_{org}. The average mixed layer depth, weighted by the area of each ocean basin, is shown as a black line in each **C** and **D**.

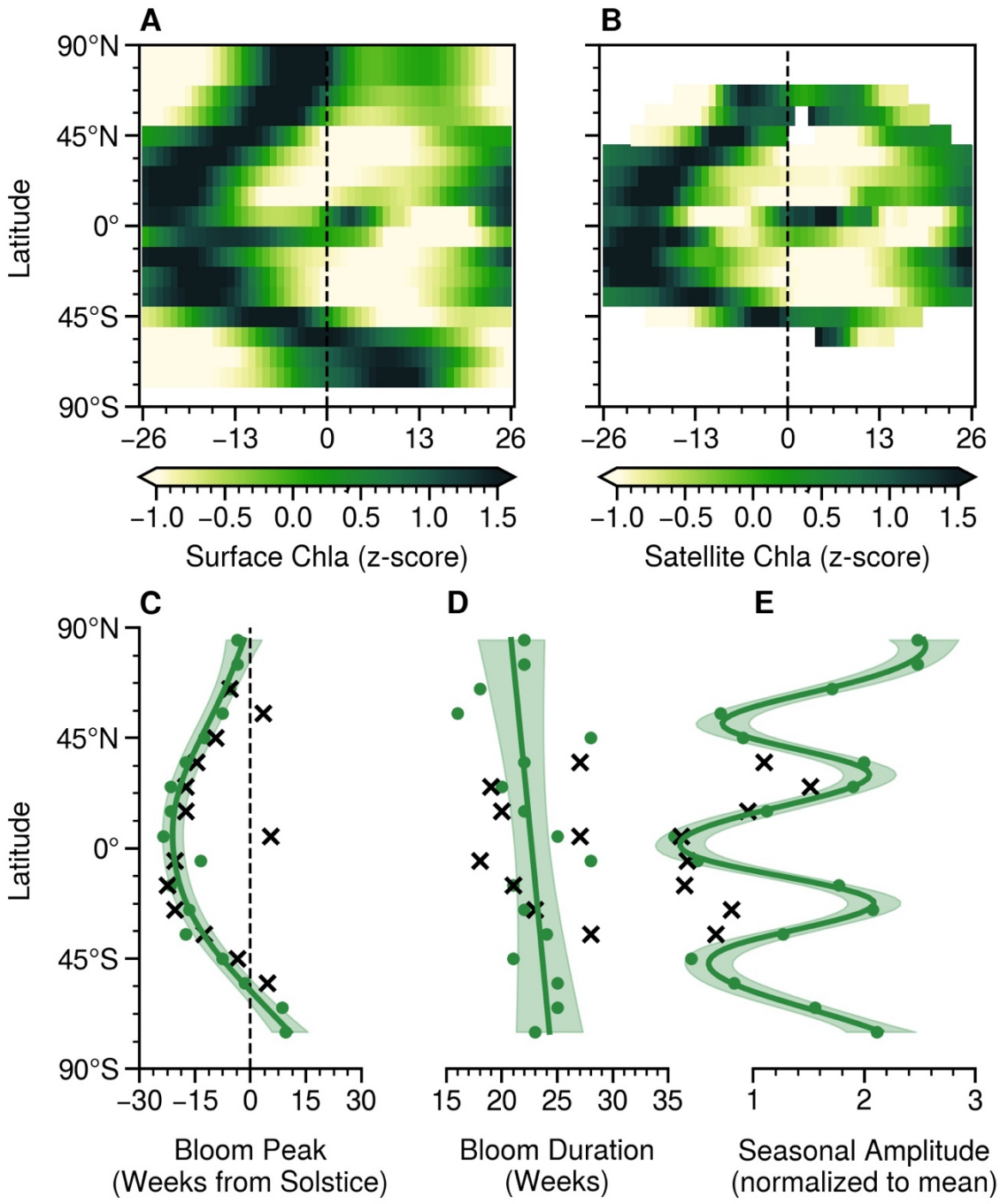

Figure C3. (**A**, **B**) Seasonal cycles in float- and satellite-based surface Chla (as z-scores). (**C**–**E**) Phenological metrics derived from the seasonal surface Chla derived from float (green points) and satellite (black x's) satellite observations: (**C**) the timing of the peak satellite and float surface Chla, defined as the week from the summer solstice; (**D**) the bloom duration, defined as the number of weeks above the annual mean; and (**E**) seasonal range, normalized to the annual mean. Panels **B** and **C** extend to 65°, while panels **D** and **E** only extend to time-series with at least 47 weeks of observations.

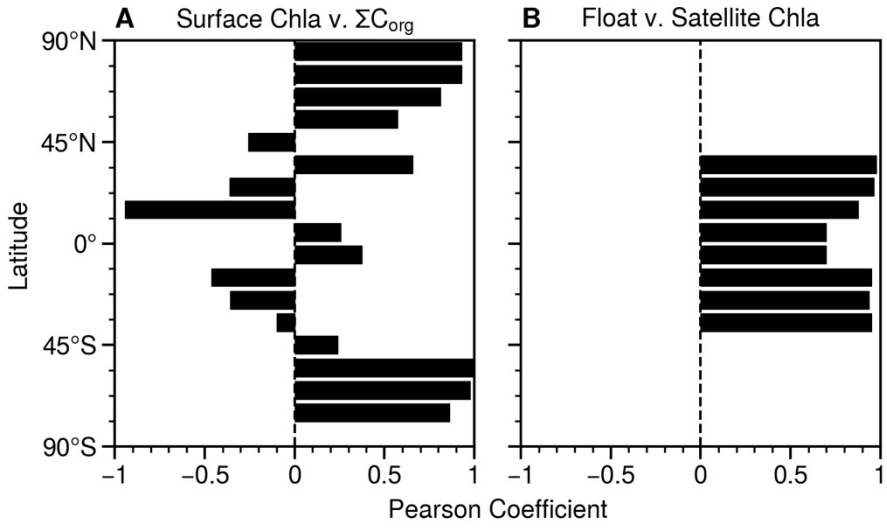

Figure C4. Pearson correlation coefficients calculated from the 52-week cycle of the log-transformed (**A**) surface Chla and ΣC_{org} and (**B**) surface Chla from floats and satellite observations.

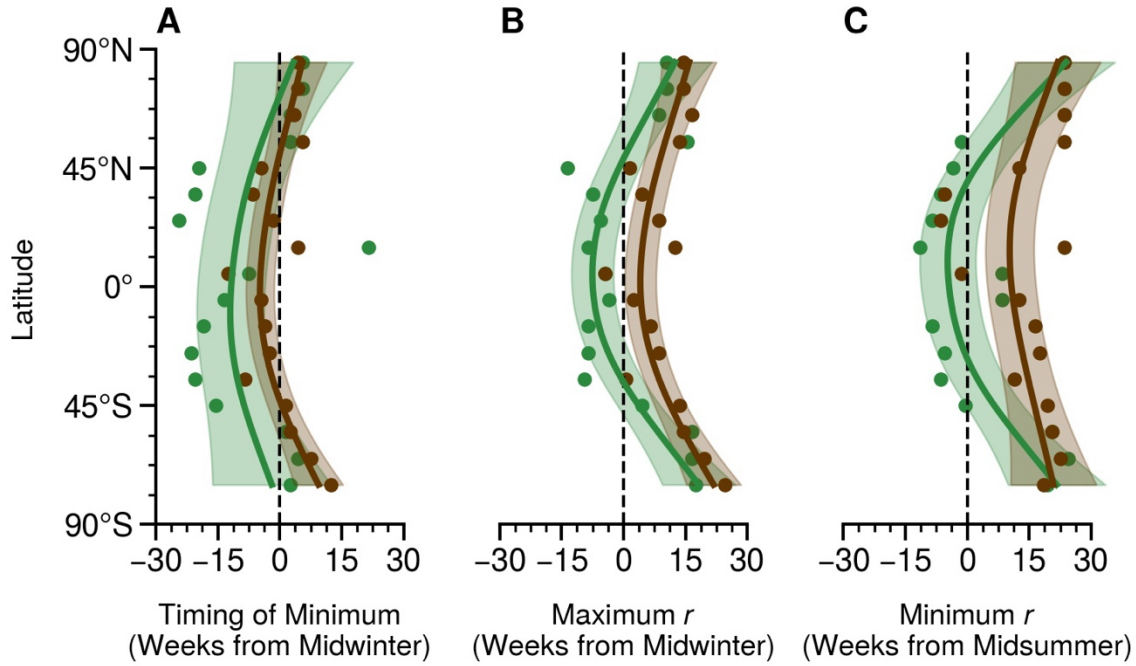

Figure C5. Additional phenological metrics calculated surface Chla (green) and ΣC_{org} (brown) of the timing of the minimum (**A**), the timing of the maximum accumulation rate (**B**), and the timing the minimum rate of change (**C**). The timing of these metrics is relative to the day of year with the least (midwinter) or most (midsummer) daylight hours.

Table C1. Float data discarded following visual inspection. When applicable, I liberally removed profiles well before the issue with the data was apparent.

Float WMO	Profiles Removed	Reason
2902209	All	Salinity is too low given expectation in the open ocean (~17 PSU).
5906207	All	There is an abrupt increase in temperature in the time series that is inconsistent with the first two years of the observations.
2902160	All	There is an abrupt consistent increase in b_{bp} that is still in range of what is realistic. It is not clear if the data before or after is usable, so the entire time series was discarded from this float.
2902158	All	The same issue in 2902160 is present with this float
5904218	Profiles after November 1, 2012	There is a slow increase in the b_{bp} possibly due to sensor drift or bio-fouling (most profiles from this float went ~400 m depth).
6901473	Profiles after September 1, 2014	There is a slow increase and decrease in the b_{bp} and Chla, respectively. This is possibly due to sensor or bio-fouling.
6901650	Profiles after June 1, 2015	There is a sudden, unrealistic drop in b_{bp}.
6901687	Profiles after July 1, 2017	There appears to be an increase in b_{bp} that is rapid, however, b_{bp} returns close to its initial values. This happens twice. Profiles were removed well before this first increase was observed.

Bibliography

Alvarez-Fernandez, S., and Riegman, R. (2014). Chlorophyll in North Sea coastal and offshore waters does not reflect long term trends of phytoplankton biomass. *J Sea Res* 91, 35–44. doi: 10.1016/j.seares.2014.04.005.

Antoine, D., André, J., and Morel, A. (1996). Oceanic primary production: 2. Estimation at global scale from satellite (Coastal Zone Color Scanner) chlorophyll. *Global Biogeochem Cycles* 10, 57–69. doi: 10.1029/95GB02832.

Argo (2000). Argo float data and metadata from Global Data Assembly Centre (Argo GDAC). *SEANOE*. Available at: doi: 10.17882/42182 [Accessed March 15, 2023].

Argo (2021). Argo float data and metadata from Global Data Assembly Centre (Argo GDAC)—Snapshot of Argo GDAC of December 10, 2021. *SEANOE*.

Argo (2023). Argo float data and metadata from Global Data Assembly Centre (Argo GDAC). *SEANOE*.

Argo Data Management Team (2022). Argo User's Manual. Available at: doi: 10.13155/29825 [Accessed January 31, 2023].

Arrigo, K. R., van Dijken, G. L., and Bushinsky, S. (2008). Primary production in the Southern Ocean, 1997–2006. *J Geophys Res Oceans* 113. doi: 10.1029/2007JC004551.

Arteaga, L. A., Boss, E., Behrenfeld, M. J., Westberry, T. K., and Sarmiento, J. L. (2020). Seasonal modulation of phytoplankton biomass in the Southern Ocean. *Nat Commun* 11, 5364. doi: 10.1038/s41467-020-19157-2.

Arteaga, L., Haëntjens, N., Boss, E., Johnson, K. S., and Sarmiento, J. L. (2018). Assessment of Export Efficiency Equations in the Southern Ocean Applied to Satellite-Based Net Primary Production. *J Geophys Res Oceans* 123, 2945–2964. doi: 10.1002/2018JC013787.

Babin, S. M., Carton, J. A., Dickey, T. D., and Wiggert, J. D. (2004). Satellite evidence of hurricane-induced phytoplankton blooms in an oceanic desert. *J Geophys Res Oceans* 109. doi: 10.1029/2003JC001938.

Banse, K. (1977). Determining the carbon-to-chlorophyll ratio of natural phytoplankton. *Mar Biol* 41, 199–212. doi: 10.1007/BF00394907.

Barbieux, M., Uitz, J., Mignot, A., Roesler, C., Claustre, H., Gentili, B., et al. (2022). Biological production in two contrasted regions of the Mediterranean Sea during the oligotrophic period: an estimate based on the diel cycle of optical properties measured by BioGeoChemical-Argo profiling floats. *Biogeosciences* 19, 1165–1194. doi: 10.5194/bg-19-1165-2022.

Bar-On, Y. M., and Milo, R. (2019). The Biomass Composition of the Oceans: A Blueprint of Our Blue Planet. *Cell* 179, 1451–1454. doi: 10.1016/j.cell.2019.11.018.

Bar-On, Y. M., Phillips, R., and Milo, R. (2018). The biomass distribution on Earth. *Proceedings of the National Academy of Sciences* 115, 6506–6511. doi: 10.1073/pnas.1711842115.

Barone, B., Nicholson, D., Ferrón, S., Firing, E., and Karl, D. (2019). The estimation of gross oxygen production and community respiration from autonomous time-series measurements in the oligotrophic ocean. *Limnol Oceanogr Methods* 17, 650–664. doi: 10.1002/lom3.10340.

Begouen Demeaux, C., and Boss, E. (2022). Validation of Remote-Sensing Algorithms for Diffuse Attenuation of Downward Irradiance Using BGC-Argo Floats. *Remote Sens (Basel)* 14, 4500. doi: 10.3390/rs14184500.

Behrenfeld, M. J. (2010). Abandoning Sverdrup's Critical Depth Hypothesis on phytoplankton blooms. *Ecology* 91, 977–989. doi: 10.1890/09-1207.1.

Behrenfeld, M. J., and Boss, E. S. (2018). Student's tutorial on bloom hypotheses in the context of phytoplankton annual cycles. *Glob Chang Biol* 24, 55–77. doi: 10.1111/gcb.13858.

Behrenfeld, M. J., Boss, E., Siegel, D. A., and Shea, D. M. (2005). Carbon-based ocean productivity and phytoplankton physiology from space. *Global Biogeochem Cycles* 19. doi: 10.1029/2004GB002299.

Behrenfeld, M. J., and Falkowski, P. G. (1997). Photosynthetic rates derived from satellite-based chlorophyll concentration. *Limnol Oceanogr* 42, 1–20. doi: 10.4319/lo.1997.42.1.0001.

Behrenfeld, M. J., Moore, R. H., Hostetler, C. A., Graff, J., Gaube, P., Russell, L. M., et al. (2019). The North Atlantic Aerosol and Marine Ecosystem Study (NAAMES): Science Motive and Mission Overview. *Front Mar Sci* 6. doi: 10.3389/fmars.2019.00122.

Behrenfeld, M. J., O'Malley, R. T., Boss, E. S., Westberry, T. K., Graff, J. R., Halsey, K. H., et al. (2016). Revaluating ocean warming impacts on global phytoplankton. *Nat Clim Chang* 6, 323–330. doi: 10.1038/nclimate2838.

Behrenfeld, M. J., O'Malley, R. T., Siegel, D. A., McClain, C. R., Sarmiento, J. L., Feldman, G. C., et al. (2006). Climate-driven trends in contemporary ocean productivity. *Nature* 444, 752–755. doi: 10.1038/nature05317.

Bellacicco, M., Cornec, M., Organelli, E., Brewin, R. J. W., Neukermans, G., Volpe, G., et al. (2019). Global Variability of Optical Backscattering by Non-algal particles From a Biogeochemical-Argo Data Set. *Geophys Res Lett* 46, 9767–9776. doi: 10.1029/2019GL084078.

Bittig, H., Fiedler, B., Scholz, R., Krahmann, G., and Körtzinger, A. (2014). Time response of oxygen optodes on profiling platforms and its dependence on flow speed and temperature. *Limnol Oceanogr Methods* 12, 617–636. doi: 10.4319/lom.2014.12.617.

Bittig, H., and Körtzinger, A. (2015). Tackling Oxygen Optode Drift: Near-Surface and In-Air Oxygen Optode Measurements on a Float Provide an Accurate in Situ Reference. *J Atmos Ocean Technol* 32, 1536–1543. doi: 10.1175/JTECH-D-14-00162.1.

Bittig, H., Maurer, T., Plant, J., Schmechtig, C., Wong, A., Claustre, H., et al. (2019). A BGC-Argo Guide: Planning, Deployment, Data Handling and Usage. *Front Mar Sci* 6, 502. doi: 10.3389/fmars.2019.00502.

Bittig, H., Wong, A., Plant, J., and the Coriolis Argo data management team (2022). BGC-Argo synthetic profile file processing and format on Coriolis GDAC, v1.3. Available at: http://dx.doi.org/10.13155/55637 [Accessed January 31, 2023].

Boss, E., and Behrenfeld, M. (2010). In situ evaluation of the initiation of the North Atlantic phytoplankton bloom. *Geophys Res Lett* 37, n/a-n/a. doi: 10.1029/2010GL044174.

Boss, E., and Haëntjens, N. (2016). Primer regarding measurements of chlorophyll fluorescence and the backscattering coefficient with WETLabs FLBB on profiling floats. Princeton.

Boss, E., Picheral, M., Leeuw, T., Chase, A., Karsenti, E., Gorsky, G., et al. (2013). The characteristics of particulate absorption, scattering and attenuation coefficients in the surface ocean; Contribution of the Tara Oceans expedition. *Methods in Oceanography* 7, 52–62. doi: 10.1016/j.mio.2013.11.002.

Boss, E., Swift, D., Taylor, L., Brickley, P., Zaneveld, R., Riser, S., et al. (2008). Observations of pigment and particle distributions in the western North Atlantic from an autonomous float and ocean color satellite. *Limnol Oceanogr* 53, 2112–2122. doi: 10.4319/lo.2008.53.5_part_2.2112.

Boyce, D. G., Petrie, B., Frank, K. T., Worm, B., and Leggett, W. C. (2017). Environmental structuring of marine plankton phenology. *Nat Ecol Evol* 1, 1484–1494. doi: 10.1038/s41559-017-0287-3.

Breitburg, D., Levin, L. A., Oschlies, A., Grégoire, M., Chavez, F. P., Conley, D. J., et al. (2018). Declining oxygen in the global ocean and coastal waters. *Science (1979)* 359. doi: 10.1126/science.aam7240.

Briggs, N., Perry, M. J., Cetinić, I., Lee, C., D'Asaro, E., Gray, A., et al. (2011). High-resolution observations of aggregate flux during a sub-polar North Atlantic spring bloom. *Deep Sea Research Part I: Oceanographic Research Papers* 58, 1031–1039. doi: 10.1016/j.dsr.2011.07.007.

Buitenhuis, E. T., Vogt, M., Moriarty, R., Bednaršek, N., Doney, S. C., Leblanc, K., et al. (2013). MAREDAT: towards a world atlas of MARine Ecosystem DATa. *Earth Syst Sci Data* 5, 227–239. doi: 10.5194/essd-5-227-2013.

Cetinić, I., Perry, M. J., Briggs, N. T., Kallin, E., D'Asaro, E. A., and Lee, C. M. (2012). Particulate organic carbon and inherent optical properties during 2008 North Atlantic Bloom Experiment. *J Geophys Res Oceans* 117, n/a-n/a. doi: 10.1029/2011JC007771.

Chai, F., Johnson, K. S., Claustre, H., Xing, X., Wang, Y., Boss, E., et al. (2020). Monitoring ocean biogeochemistry with autonomous platforms. *Nat Rev Earth Environ* 1, 315–326. doi: 10.1038/s43017-020-0053-y.

Chai, F., Wang, Y., Xing, X., Yan, Y., Xue, H., Wells, M., et al. (2021). A limited effect of sub-tropical typhoons on phytoplankton dynamics. *Biogeosciences* 18, 849–859. doi: 10.5194/bg-18-849-2021.

Cheng, L., von Schuckmann, K., Abraham, J. P., Trenberth, K. E., Mann, M. E., Zanna, L., et al. (2022). Past and future ocean warming. *Nat Rev Earth Environ* 3, 776–794. doi: 10.1038/s43017-022-00345-1.

Chiswell, S. M., Gutiérrez-Rodríguez, A., Gall, M., Safi, K., Strzepek, R., Décima, M. R., et al. (2022). Seasonal cycles of phytoplankton and net primary production from Biogeochemical Argo float data in the south-west Pacific Ocean. *Deep Sea Research Part I: Oceanographic Research Papers* 187, 103834. doi: 10.1016/j.dsr.2022.103834.

Claustre, H., Johnson, K. S., and Takeshita, Y. (2020). Observing the Global Ocean with Biogeochemical-Argo. *Ann Rev Mar Sci* 12, 23–48. doi: 10.1146/annurev-marine-010419-010956.

Cloern, J. E., Grenz, C., and Vidergar-Lucas, L. (1995). An empirical model of the phytoplankton chlorophyll : carbon ratio-the conversion factor between productivity and growth rate. *Limnol Oceanogr* 40, 1313–1321. doi: 10.4319/lo.1995.40.7.1313.

Cloern, J. E., and Jassby, A. D. (2008). Complex seasonal patterns of primary producers at the land-sea interface. *Ecol Lett* 11, 1294–1303. doi: 10.1111/j.1461-0248.2008.01244.x.

Cornec, M., Claustre, H., Mignot, A., Guidi, L., Lacour, L., Poteau, A., et al. (2021). Deep Chlorophyll Maxima in the Global Ocean: Occurrences, Drivers and Characteristics. *Global Biogeochem Cycles* 35. doi: 10.1029/2020GB006759.

Cossarini, G., Feudale, L., Teruzzi, A., Bolzon, G., Coidessa, G., Solidoro, C., et al. (2021). High-Resolution Reanalysis of the Mediterranean Sea Biogeochemistry (1999–2019). *Front Mar Sci* 8. doi: 10.3389/fmars.2021.741486.

Cullen, J. J. (1982). The Deep Chlorophyll Maximum: Comparing Vertical Profiles of Chlorophyll a. *Canadian Journal of Fisheries and Aquatic Sciences* 39, 791–803. doi: 10.1139/f82-108.

Cullen, J. J. (2015). Subsurface Chlorophyll Maximum Layers: Enduring Enigma or Mystery Solved? *Ann Rev Mar Sci* 7, 207–239. doi: 10.1146/annurev-marine-010213-135111.

Dall'Olmo, G., Bhaskar TVS, U., Bittig, H., Boss, E., Brewster, J., Claustre, H., et al. (2023). Real-time quality control of optical backscattering data from Biogeochemical-Argo floats. *Open Research Europe* 2, 118. doi: 10.12688/openreseurope.15047.2.

de Boyer Montégut, C., Madec, G., Fischer, A., Lazar, A., and Ludicone, D. (2004). Mixed layer depth over the global ocean: An examination of profile data and a profile-based climatology. *J Geophys Res* 109, C12003. doi: 10.1029/2004JC002378.

Doney, S. C., Fabry, V. J., Feely, R. A., and Kleypas, J. A. (2009). Ocean Acidification: The Other CO_2 Problem. *Ann Rev Mar Sci* 1, 169–192. doi: 10.1146/annurev.marine.010908.163834.

Dong, S., Sprintall, J., Gille, S. T., and Talley, L. (2008). Southern Ocean mixed-layer depth from Argo float profiles. *J Geophys Res* 113, C06013. doi: 10.1029/2006JC004051.

Eppley, R. W., Carlucci, A. F., Holm-Hansen, O., Kiefer, D., McCarthy, J. J., Venrick, E., et al. (1971). PHYTOPLANKTON GROWTH AND COMPOSITION IN SHIPBOARD CULTURES SUPPLIED WITH NITRATE, AMMONIUM, OR UREA AS THE NITROGEN SOURCE1. *Limnol Oceanogr* 16, 741–751. doi: 10.4319/lo.1971.16.5.0741.

Eppley, R. W., Stewart, E., Abbott, M. R., and Heyman, U. (1985). Estimating ocean primary production from satellite chlorophyll. Introduction to regional differences and statistics for the Southern California Bight. *J Plankton Res* 7, 57–70. doi: 10.1093/plankt/7.1.57.

Falkowski, P. G. (1994). The role of phytoplankton photosynthesis in global biogeochemical cycles. *Photosynth Res* 39, 235–258. doi: 10.1007/BF00014586.

Falkowski, P., and Raven, J. (1997). "Aquatic Photosynthesis in Biogeochemical Cycles," in *Aquatic Photosynthesis: (Second Edition)* (Princeton University Press), 389.

Falkowski, P., Scholes, R. J., Boyle, E., Canadell, J., Canfield, D., Elser, J., et al. (2000). The Global Carbon Cycle: A Test of Our Knowledge of Earth as a System. *Science (1979)* 290, 291–296. doi: 10.1126/science.290.5490.291.

Fennel, K., and Boss, E. (2003). Subsurface maxima of phytoplankton and chlorophyll: Steady-state solutions from a simple model. *Limnol Oceanogr* 48, 1521–1534. doi: 10.4319/lo.2003.48.4.1521.

Field, C. B., Behrenfeld, M. J., Randerson, J. T., and Falkowski, P. (1998). Primary production of the biosphere: Integrating terrestrial and oceanic components. *Science (1979)* 281, 237–240. doi: 10.1126/science.281.5374.237.

Flanders Marine Institute (2021). Global Oceans and Seas, version 1. Available at: https://doi.org/10.14284/542 [Accessed January 31, 2023].

Fox, J., Kramer, S. J., Graff, J. R., Behrenfeld, M. J., Boss, E., Tilstone, G., et al. (2022). An absorption-based approach to improved estimates of phytoplankton biomass and net primary production. *Limnol Oceanogr Lett* 7, 419–426. doi: 10.1002/lol2.10275.

Garcia, H. E., and Gordon, L. I. (1992). Oxygen solubility in seawater: Better fitting equations. *Limnol Oceanogr* 37, 1307–1312. doi: 10.4319/lo.1992.37.6.1307.

Geider, R. J. (1987). Light and Temperature Dependence of the Carbon to Chlorophyll a Ratio in Microalgae and Cyanobacteria: Implications for Physiology and Growth of Phytoplankton. *New Phytologist* 106, 1–34.

Geider, R. J., MacIntyre, H. L., and Kana, T. (1997). Dynamic model of phytoplankton growth and acclimation: responses of the balanced growth rate and the chlorophyll a: carbon ratio to light, nutrient-limitation and temperature. *Dynamic model of phytoplankton growth and acclimation: responses of the balanced growth rate and the chlorophyll a: carbon ratio to light, nutrient-limitation and temperature* 148, 187–200.

Gille, S. T. (2012). Diurnal variability of upper ocean temperatures from microwave satellite measurements and Argo profiles. *J Geophys Res Oceans* 117, n/a-n/a. doi: 10.1029/2012JC007883.

Gordon, C., Fennel, K., Richards, C., Shay, L., and Brewster, J. (2020). Can ocean community production and respiration be determined by measuring high-frequency oxygen profiles from autonomous floats? *Biogeosciences* 17, 4119–4134. doi: 10.5194/bg-17-4119-2020.

Gordon, H. R., Clark, D. K., Brown, J. W., Brown, O. B., Evans, R. H., and Broenkow, W. W. (1983). Phytoplankton pigment concentrations in the Middle Atlantic Bight: comparison of ship determinations and CZCS estimates. *Appl Opt* 22, 20. doi: 10.1364/AO.22.000020.

Gordon, H. R., and McCluney, W. R. (1975). Estimation of the Depth of Sunlight Penetration in the Sea for Remote Sensing. *Appl Opt* 14, 413. doi: 10.1364/AO.14.000413.

Graff, J. R., Milligan, A. J., and Behrenfeld, M. J. (2012). The measurement of phytoplankton biomass using flow-cytometric sorting and elemental analysis of carbon. *Limnol Oceanogr Methods* 10, 910–920. doi: 10.4319/lom.2012.10.910.

Graff, J. R., Westberry, T. K., Milligan, A. J., Brown, M. B., Dall'Olmo, G., Dongen-Vogels, V. van, et al. (2015). Analytical phytoplankton carbon measurements spanning diverse ecosystems. *Deep Sea Research Part I: Oceanographic Research Papers* 102, 16–25. doi: 10.1016/j.dsr.2015.04.006.

Hamilton, P., and Leidos (2017). Ocean currents, temperatures, and others measured by drifters and profiling floats for the Lagrangian Approach to Study the Gulf of Mexico Deep Circulation project 2011-07 to 2015-06 (NCEI Accession 0159562).

He, Q., McGillicuddy, D. J., Xing, X., Cai, S., Zhan, W., He, Y., et al. (2023). Subsurface phytoplankton responses to ocean eddies can run counter to satellite-based inference from surface properties in subtropical gyres. *Prog Oceanogr* 218, 103118. doi: 10.1016/j.pocean.2023.103118.

Henson, S. A., Cael, B. B., Allen, S. R., and Dutkiewicz, S. (2021). Future phytoplankton diversity in a changing climate. *Nat Commun* 12, 5372. doi: 10.1038/s41467-021-25699-w.

Henson, S. A., Cole, H. S., Hopkins, J., Martin, A. P., and Yool, A. (2018). Detection of climate change-driven trends in phytoplankton phenology. *Glob Chang Biol* 24, e101–e111. doi: 10.1111/gcb.13886.

Ho, T.-Y., Quigg, A., Finkel, Z. V., Milligan, A. J., Wyman, K., Falkowski, P. G., et al. (2003). The elemental composition of some marine phytoplankton. *J Phycol* 39, 1145–1159. doi: 10.1111/j.0022-3646.2003.03-090.x.

Holm-Hansen, O., Lorenzen, C. J., Holmes, R. W., and Strickland, J. D. H. (1965). Fluorometric Determination of Chlorophyll. *ICES Journal of Marine Science* 30, 3–15. doi: 10.1093/icesjms/30.1.3.

Holte, J., Talley, L. D., Gilson, J., and Roemmich, D. (2017). An Argo mixed layer climatology and database. *Geophys Res Lett* 44, 5618–5626. doi: 10.1002/2017GL073426.

Jackson, T., Sathyendranath, S., and Platt, T. (2017). An Exact Solution For Modeling Photoacclimation of the Carbon-to-Chlorophyll Ratio in Phytoplankton. *Front Mar Sci* 4. doi: 10.3389/fmars.2017.00283.

Johnson, K., and Bif, M. (2021). Constraint on net primary productivity of the global ocean by Argo oxygen measurements. *Nat Geosci* 14, 769–774. doi: 10.1038/s41561-021-00807-z.

Johnson, K., Maurer, T., Plant, J., Bittig, H., Schallenberg, C., and Schmechtig, C. (2021). BGC-Argo quality control manual for nitrate concentration. Available at: http://dx.doi.org/10.13155/84370 [Accessed January 31, 2023].

Johnson, K., Plant, J., and Maurer, T. (2018). Processing BGC-Argo pH data at the DAC level. Available at: https://doi.org/10.13155/57195 [Accessed January 31, 2023].

Johnson, K., Plant, J., Riser, S., and Gilbert, D. (2015). Air Oxygen Calibration of Oxygen Optodes on a Profiling Float Array. *J Atmos Ocean Technol* 32, 2160–2172. doi: 10.1175/JTECH-D-15-0101.1.

Johnson, K. S., Coletti, L. J., and Chavez, F. P. (2006). Diel nitrate cycles observed with in situ sensors predict monthly and annual new production. *Deep Sea Research Part I: Oceanographic Research Papers* 53, 561–573. doi: 10.1016/j.dsr.2005.12.004.

Johnson, K. S., Plant, J. N., Coletti, L. J., Jannasch, H. W., Sakamoto, C. M., Riser, S. C., et al. (2017). Biogeochemical sensor performance in the SOCCOM profiling float array. *J Geophys Res Oceans* 122, 6416–6436. doi: 10.1002/2017JC012838.

Jutard, Q., Organelli, E., Briggs, N., Xing, X., Schmechtig, C., Boss, E., et al. (2021). Correction of Biogeochemical-Argo Radiometry for Sensor Temperature-Dependence and Drift: Protocols for a Delayed-Mode Quality Control. *Sensors* 21, 6217. doi: 10.3390/s21186217.

Kheireddine, M., and Antoine, D. (2014). Diel variability of the beam attenuation and backscattering coefficients in the northwestern Mediterranean Sea (BOUSSOLE site). *J Geophys Res Oceans* 119, 5465–5482. doi: 10.1002/2014JC010007.

Lavigne, H., D'Ortenzio, F., Ribera D'Alcalà, M., Claustre, H., Sauzède, R., and Gacic, M. (2015). On the vertical distribution of the chlorophyll a concentration in the Mediterranean Sea: a basin-scale and seasonal approach. *Biogeosciences* 12, 5021–5039. doi: 10.5194/bg-12-5021-2015.

Laws, E. A. (1991). Photosynthetic quotients, new production and net community production in the open ocean. *Deep Sea Research Part A. Oceanographic Research Papers* 38, 143–167. doi: 10.1016/0198-0149(91)90059-O.

Lee, Z., Weidemann, A., Kindle, J., Arnone, R., Carder, K. L., and Davis, C. (2007). Euphotic zone depth: Its derivation and implication to ocean-color remote sensing. *J Geophys Res* 112, C03009. doi: 10.1029/2006JC003802.

Lindeman, R. (1942). The trophic-dynamic aspect of ecology. *Ecology* 23, 399–417.

Marra, J. (2002). "Approaches to the Measurement of Plankton Production," in *Phytoplankton productivity: Carbon assimilation in marine and freshwater ecosystems*, eds. P. Williams, D. Thomas, and C. Reynolds (Wiley), 78–108. doi: 10.1002/9780470995204.ch4.

Marra, J. (2022). An ocean productivity database using consistent, globally-acquired data from in situ primary productivity based on 14C assimilation, and including ancillary data, 1985-2008. *Biological and Chemical Oceanography Data Management Office (BCO-DMO)* Verson 1.

Marra, J. F., Barber, R. T., Barber, E., Bidigare, R. R., Chamberlin, W. S., Goericke, R., et al. (2021). A database of ocean primary productivity from the <scp> ^{14} C </scp> method. *Limnol Oceanogr Lett* 6, 107–111. doi: 10.1002/lol2.10175.

Martinez, E., Antoine, D., D'Ortenzio, F., and Gentili, B. (2009). Climate-Driven Basin-Scale Decadal Oscillations of Oceanic Phytoplankton. *Science (1979)* 326, 1253–1256. doi: 10.1126/science.1177012.

Martinez-Vicente, V., Dall'Olmo, G., Tarran, G., Boss, E., and Sathyendranath, S. (2013). Optical backscattering is correlated with phytoplankton carbon across the Atlantic Ocean. *Geophys Res Lett* 40, 1154–1158. doi: 10.1002/grl.50252.

Masuda, Y., Yamanaka, Y., Smith, S. L., Hirata, T., Nakano, H., Oka, A., et al. (2021). Photoacclimation by phytoplankton determines the distribution of global subsurface chlorophyll maxima in the ocean. *Commun Earth Environ* 2, 128. doi: 10.1038/s43247-021-00201-y.

Mattei, F., and Scardi, M. (2021a). Collection and analysis of a global marine phytoplankton primary-production dataset. *Earth Syst Sci Data* 13, 4967–4985. doi: 10.5194/essd-13-4967-2021.

Mattei, F., and Scardi, M. (2021b). Global marine phytoplankton production dataset. *PANGAEA*.

Maurer, T., Plant, J., and Johnson, K. (2021). Delayed-Mode Quality Control of Oxygen, Nitrate, and pH Data on SOCCOM Biogeochemical Profiling Floats. *Front Mar Sci* 8. doi: 10.3389/fmars.2021.683207.

McClain, C. R. (2009). A Decade of Satellite Ocean Color Observations. *Ann Rev Mar Sci* 1, 19–42. doi: 10.1146/annurev.marine.010908.163650.

Moore, J. K., and Abbott, M. R. (2000). Phytoplankton chlorophyll distributions and primary production in the Southern Ocean. *J Geophys Res Oceans* 105, 28709–28722. doi: 10.1029/1999JC000043.

Moran, M. A., Ferrer-González, F. X., Fu, H., Nowinski, B., Olofsson, M., Powers, M. A., et al. (2022). The Ocean’s labile <scp>DOC</scp> supply chain. *Limnol Oceanogr* 67, 1007–1021. doi: 10.1002/lno.12053.

Morel, A. (1988). Optical modeling of the upper ocean in relation to its biogenous matter content (case I waters). *J Geophys Res* 93, 10749–10768. doi: 10.1029/JC093iC09p10749.

NASA Goddard Space Flight Center, Ocean Ecology Laboratory, and Ocean Biology Processing Group (2022). Moderate-resolution imaging spectroradiometer (MODIS) aqua euphotic depth data; 2018 reprocessing.

NOAA (1988). Data announcement 88-MGG-02, digital relief of the surface of the earth. *NOAA, National Geophysical Data Center, [accessed 2021 August 21]. Available from https://www.ngdc.noaa.gov/mgg/global/etopo5.HTML*.

O'Brien, T., and Boss, E. (2022). Correction of Radiometry Data for Temperature Effect on Dark Current, with Application to Radiometers on Profiling Floats. *Sensors* 22, 6771. doi: 10.3390/s22186771.

Organelli, E., Barbieux, M., Claustre, H., Schmechtig, C., Poteau, A., Bricaud, A., et al. (2017). Two databases derived from BGC-Argo float measurements for marine biogeochemical and bio-optical applications. *Earth Syst Sci Data* 9, 861–880. doi: 10.5194/essd-9-861-2017.

Organelli, E., Claustre, H., Bricaud, A., Schmechtig, C., Poteau, A., Xing, X., et al. (2016). A Novel Near-Real-Time Quality-Control Procedure for Radiometric Profiles Measured by Bio-Argo Floats: Protocols and Performances. *J Atmos Ocean Technol* 33, 937–951. doi: 10.1175/JTECH-D-15-0193.1.

Parekh, P., Dutkiewicz, S., Follows, M. J., and Ito, T. (2006). Atmospheric carbon dioxide in a less dusty world. *Geophys Res Lett* 33, L03610. doi: 10.1029/2005GL025098.

Platt, T., Fuentes-Yaco, C., and Frank, K. T. (2003). Spring algal bloom and larval fish survival. *Nature* 423, 398–399. doi: 10.1038/423398b.

Platt, T., and Sathyendranath, S. (2008). Ecological indicators for the pelagic zone of the ocean from remote sensing. *Remote Sens Environ* 112, 3426–3436. doi: 10.1016/j.rse.2007.10.016.

Poteau, A., Organelli, E., Boss, E., and Xing, X. (2019). Quality control for BGC-Argo radiometry.

Poulin, C., Antoine, D., and Huot, Y. (2018). Diurnal variations of the optical properties of phytoplankton in a laboratory experiment and their implication for using inherent optical properties to measure biomass. *Opt Express* 26, 711. doi: 10.1364/OE.26.000711.

Racault, M.-F., Le Quéré, C., Buitenhuis, E., Sathyendranath, S., and Platt, T. (2012). Phytoplankton phenology in the global ocean. *Ecol Indic* 14, 152–163. doi: 10.1016/j.ecolind.2011.07.010.

Randelhoff, A., Lacour, L., Marec, C., Leymarie, E., Lagunas, J., Xing, X., et al. (2020). Arctic mid-winter phytoplankton growth revealed by autonomous profilers. *Sci Adv* 6. doi: 10.1126/sciadv.abc2678.

Rasse, R., Dall'Olmo, G., Graff, J., Westberry, T. K., van Dongen-Vogels, V., and Behrenfeld, M. J. (2017). Evaluating Optical Proxies of Particulate Organic Carbon across the Surface Atlantic Ocean. *Front Mar Sci* 4. doi: 10.3389/fmars.2017.00367.

Riebesell, U., Körtzinger, A., and Oschlies, A. (2009). Sensitivities of marine carbon fluxes to ocean change. *Proceedings of the National Academy of Sciences* 106, 20602–20609. doi: 10.1073/pnas.0813291106.

Riley, G. A., Stommel, H., and Bumpus, D. F. (1949). Quantitative ecology of the phytoplankton of the Western North Atlantic. *Bulletin of the Bingham Oceanographic Collection* 12, 1–169.

Riser, S. C., Swift, D., and Drucker, R. (2018). Profiling Floats in SOCCOM: Technical Capabilities for Studying the Southern Ocean. *J Geophys Res Oceans* 123, 4055–4073. doi: 10.1002/2017JC013419.

Roemmich, D., Alford, M. H., Claustre, H., Johnson, K., King, B., Moum, J., et al. (2019). On the Future of Argo: A Global, Full-Depth, Multi-Disciplinary Array. *Front Mar Sci* 6. doi: 10.3389/fmars.2019.00439.

Roesler, C., Uitz, J., Claustre, H., Boss, E., Xing, X., Organelli, E., et al. (2017). Recommendations for obtaining unbiased chlorophyll estimates from in situ chlorophyll fluorometers: A global analysis of WET Labs ECO sensors. *Limnol Oceanogr Methods* 15, 572–585. doi: 10.1002/lom3.10185.

Ryan-Keogh, T. J., and Thomalla, S. J. (2020). Deriving a Proxy for Iron Limitation From Chlorophyll Fluorescence on Buoyancy Gliders. *Front Mar Sci* 7. doi: 10.3389/fmars.2020.00275.

Ryan-Keogh, T. J., Thomalla, S. J., Monteiro, P. M. S., and Tagliabue, A. (2023). Multidecadal trend of increasing iron stress in Southern Ocean phytoplankton. *Science (1979)* 379, 834–840. doi: 10.1126/science.abl5237.

Sarmiento, J. L., Johnson, K. S., Arteaga, L. A., Bushinsky, S. M., Cullen, H. M., Gray, A. R., et al. (2023). The Southern Ocean carbon and climate observations and modeling (SOCCOM) project: A review. *Prog Oceanogr* 219, 103130. doi: 10.1016/j.pocean.2023.103130.

Sathyendranath, S., Stuart, V., Nair, A., Oka, K., Nakane, T., Bouman, H., et al. (2009). Carbon-to-chlorophyll ratio and growth rate of phytoplankton in the sea. *Mar Ecol Prog Ser* 383, 73–84. doi: 10.3354/meps07998.

Sauzède, R., Claustre, H., Uitz, J., Jamet, C., Dall'Olmo, G., D'Ortenzio, F., et al. (2016). A neural network-based method for merging ocean color and Argo data to extend surface bio-optical properties to depth: Retrieval of the particulate backscattering coefficient. *J Geophys Res Oceans* 121, 2552–2571. doi: 10.1002/2015JC011408.

Schallenberg, C., Strzepek, R. F., Bestley, S., Wojtasiewicz, B., and Trull, T. W. (2022). Iron Limitation Drives the Globally Extreme Fluorescence/Chlorophyll Ratios of the Southern Ocean. *Geophys Res Lett* 49, e2021GL097616. doi: 10.1029/2021GL097616.

Schmechtig, C., Boss, E., Briggs, N., Claustre, H., Dall'Olmo, G., and Poteau, A. (2019). BGC Argo quality control manual for particles backscattering. Available at: https://doi.org/10.13155/60262 [Accessed January 31, 2023].

Schmechtig, C., Claustre, H., Poteau, A., and D'Ortenzio, F. (2018). BGC-Argo quality control manual for the Chlorophyll-A concentration. Available at: http://doi.org/10.13155/35385 [Accessed January 31, 2023].

Schmechtig, C., Thierry, V., and the Bio Argo Team (2015). Argo Quality Control Manual For Biogeochemical Data. Available at: http://dx.doi.org/10.13155/40879 [Accessed January 31, 2023].

Schmidtko, S., Stramma, L., and Visbeck, M. (2017). Decline in global oceanic oxygen content during the past five decades. *Nature* 542, 335–339. doi: 10.1038/nature21399.

Shay, L., Fennel, K., Jaimes, B., Brewster, J., Gordon, C., Rastin, S., et al. (2018). Conductivity, temperature, and depth (CTD) data collected from R/V F.G. Walton Smith cruise WS17121 in the northeastern Gulf of Mexico from 2017-05-02 to 2017-05-07.

Siegel, D. A., Dickey, T. D., Washburn, L., Hamilton, M. K., and Mitchell, B. G. (1989). Optical determination of particulate abundance and production variations in the oligotrophic ocean. *Deep Sea Research Part A. Oceanographic Research Papers* 36, 211–222. doi: 10.1016/0198-0149(89)90134-9.

Siegel, D. A., Doney, S. C., and Yoder, J. A. (2002). The North Atlantic Spring Phytoplankton Bloom and Sverdrup's Critical Depth Hypothesis. *Science (1979)* 296, 730–733. doi: 10.1126/science.1069174.

Silsbe, G. M., Behrenfeld, M. J., Halsey, K. H., Milligan, A. J., and Westberry, T. K. (2016). The CAFE model: A net production model for global ocean phytoplankton. *Global Biogeochem Cycles* 30, 1756–1777. doi: 10.1002/2016GB005521.

Steele, J. H. (1964). A Study of Production in the Gulf of Mexico. *J Mar Res* 22, 211–222.

Steemann Nielsen, E. (1951). Measurement of the Production of Organic Matter in the Sea by means of Carbon-14. *Nature* 167, 684–685. doi: 10.1038/167684b0.

Stoer, A. C., and Fennel, K. (2023). Estimating ocean net primary productivity from daily cycles of carbon biomass measured by profiling floats. *Limnol Oceanogr Lett* 8, 368–375. doi: 10.1002/lol2.10295.

Stoer, A. C., Takeshita, Y., Maurer, T. L., Begouen Demeaux, C., Bittig, H. C., Boss, E., et al. (2023). A Census of Quality-Controlled Biogeochemical-Argo Float Measurements. *Front Mar Sci* 10.

Stramski, D., Reynolds, R. A., Babin, M., Kaczmarek, S., Lewis, M. R., Röttgers, R., et al. (2008). Relationships between the surface concentration of particulate organic carbon and optical properties in the eastern South Pacific and eastern Atlantic Oceans. *Biogeosciences* 5, 171–201. doi: 10.5194/bg-5-171-2008.

Stramski, D., Reynolds, R. A., Kahru, M., and Mitchell, B. G. (1999). Estimation of Particulate Organic Carbon in the Ocean from Satellite Remote Sensing. *Science (1979)* 285, 239–242. doi: 10.1126/science.285.5425.239.

Takeshita, Y., Martz, T. R., Johnson, K., Plant, J., Gilbert, D., Riser, S., et al. (2013). A climatology-based quality control procedure for profiling float oxygen data. *J Geophys Res Oceans* 118, 5640–5650. doi: 10.1002/jgrc.20399.

Thierry, V., Bittig, H., and the Argo-BGC team (2021). Argo Quality Control Manual for Dissolved Oxygen Concentration, v2.1. Available at: http://dx.doi.org/10.13155/46542 [Accessed January 31, 2023].

Thomalla, S. J., Nicholson, S.-A., Ryan-Keogh, T. J., and Smith, M. E. (2023). Widespread changes in Southern Ocean phytoplankton blooms linked to climate drivers. *Nat Clim Chang* 13, 975–984. doi: 10.1038/s41558-023-01768-4.

Thomalla, S. J., Ogunkoya, A. G., Vichi, M., and Swart, S. (2017a). Using Optical Sensors on Gliders to Estimate Phytoplankton Carbon Concentrations and Chlorophyll-to-Carbon Ratios in the Southern Ocean. *Front Mar Sci* 4. doi: 10.3389/fmars.2017.00034.

Thomalla, S. J., Ogunkoya, A. G., Vichi, M., and Swart, S. (2017b). Using Optical Sensors on Gliders to Estimate Phytoplankton Carbon Concentrations and Chlorophyll-to-Carbon Ratios in the Southern Ocean. *Front Mar Sci* 4. doi: 10.3389/fmars.2017.00034.

Vives, C. R., Schallenberg, C., Strutton, P. G., and Boyd, P. W. (2023). Biogeochemical-Argo floats show that chlorophyll increases before carbon in the high-latitude Southern Ocean spring bloom. *Limnol Oceanogr Lett*. doi: 10.1002/lol2.10322.

Westberry, T., Behrenfeld, M. J., Siegel, D. A., and Boss, E. (2008). Carbon-based primary productivity modeling with vertically resolved photoacclimation. *Global Biogeochem Cycles* 22, n/a-n/a. doi: 10.1029/2007GB003078.

Westberry, T. K., Schultz, P., Behrenfeld, M. J., Dunne, J. P., Hiscock, M. R., Maritorena, S., et al. (2016). Annual cycles of phytoplankton biomass in the subarctic Atlantic and Pacific Ocean. *Global Biogeochem Cycles* 30, 175–190. doi: 10.1002/2015GB005276.

Xing, X., Boss, E., Chen, S., and Chai, F. (2021). Seasonal and Daily-Scale Photoacclimation Modulating the Phytoplankton Chlorophyll-Carbon Coupling Relationship in the Mid-Latitude Northwest Pacific. *J Geophys Res Oceans* 126. doi: 10.1029/2021JC017717.

Xing, X., Briggs, N., Boss, E., and Claustre, H. (2018). Improved correction for non-photochemical quenching of in situ chlorophyll fluorescence based on a synchronous irradiance profile. *Opt Express* 26, 24734–24751. doi: 10.1364/OE.26.024734.

Xing, X., Claustre, H., Blain, S., D'Ortenzio, F., Antoine, D., Ras, J., et al. (2012). Quenching correction for in vivo chlorophyll fluorescence acquired by autonomous platforms: A case study with instrumented elephant seals in the Kerguelen region (Southern Ocean). *Limnol Oceanogr Methods* 10, 483–495. doi: 10.4319/lom.2012.10.483.

Xing, X., Morel, A., Claustre, H., Antoine, D., D'Ortenzio, F., Poteau, A., et al. (2011). Combined processing and mutual interpretation of radiometry and fluorimetry from autonomous profiling Bio-Argo floats: Chlorophyll a retrieval. *J Geophys Res* 116, C06020. doi: 10.1029/2010JC006899.

Yoder, J. A., and Kennelly, M. A. (2003). Seasonal and ENSO variability in global ocean phytoplankton chlorophyll derived from 4 years of SeaWiFS measurements. *Global Biogeochem Cycles* 17, n/a-n/a. doi: 10.1029/2002GB001942.

Yoder, J. A., McClain, C. R., Feldman, G. C., and Esaias, W. E. (1993). Annual cycles of phytoplankton chlorophyll concentrations in the global ocean: A satellite view. *Global Biogeochem Cycles* 7, 181–193. doi: 10.1029/93GB02358.